DISSERTATION

FUNDAMENTAL RESEARCH INTO GOLD NANOCLUSTER PROPERTIES

Submitted by

Phillip S. Window

Department of Chemistry

In partial fulfillment of the requirements

For the Degree of Doctor of Philosophy

Colorado State University

Fort Collins, Colorado

Summer 2021

Doctoral committee:

Advisor: Christopher J. Ackerson

James R. Neilson
Alan J. Kennan
Olve Peersen

ABSTRACT

FUNDAMENTAL RESEARCH INTO GOLD NANOCLUSTER PROPERTIES

Gold materials are popular for research into many applications with their interesting properties, such as magnetism, bio-inactivity, and other size-dependent properties. As the size of the gold material decreases from a bulk material to the the nanoscale, new properties are introduced moving through different size regimes. As the particle size reaches the 2-3 nm range and move into the quantum-confined particle range, the most interesting particle changes occur and gold nanomaterials have extremely interesting research potential. These materials exist between the bulk and molecular systems and have similar properties to both; however, they are different enough from both of these to have their own unique application possibilities.

Some properties of gold nanoclusters can be attributed more to the core or more to the ligand layer of the nanocluster. Certain properties, like electronics and magnetism, are due to the superatomic electron count and electronic structure from the core and depend on the number of gold atoms in the nanocluster. Extensive research has been done on investigating and altering these properties in small nanoclusters, however, larger nanoclusters have hardly been studied as they can be more difficult to work with. Within this work is investigated the magnetism and thus electronic structure of $Au_{102}(SPh)_{44}$ and $Au_{133}(tBBT)_{52}$ in different oxidation states. Paramagnetism up to two unpaired electrons is observed with both these nanoclusters through solution phase magnetic studies. Through this, electronic structure information has been obtained to elucidate the behavior of unique superatomic 1G and 1H orbitals.

Looking at the outside of a nanocluster structure, interactions of nanoclusters with other nanoclusters, molecules, surfaces, and solvents are all due to the ligand layer of the nanocluster. Investigations of the ligand layer have been performed extensively through many techniques. However, further studies are always helpful since controlling the ligand layer is essential for functionalization for potential applications. Within this work is investigated the interactions of $Au_{25}(SR)_{18}$ with other Au_{25} nanoclusters in both solution and solid phase, as well as ligand exchange reactions of $Au_{133}(tBBT)_{52}$. Studies on $Au_{25}(SR)_{18}$ within solution include investigations of a supramolecular assembly, or supercluster, formed solely of the nanocluster itself with control over its growth and size. Studies on $Au_{25}(SR)_{18}$ within the solid-phase include controlled crystallization techniques that result in different solid-phase structures with previously unseen properties. Ligand exchange studies have also been expanded from small nanocluster materials only in previously published studies to the large nanocluster, $Au_{133}(tBBT)_{52}$.

Within this dissertation, some of the first empirical studies into the oxidation state-dependent properties of large gold nanoclusters, $Au_{102}(SPh)_{44}$ and $Au_{133}(tBBT)_{52}$, were performed. This betters the field's understanding of how many unpaired electron spins these large gold nanocluster can sustain at room temperature and further elucidates the behavior of superatomic electronic structure and behavior based on electron count. Furthermore, this dissertation presents the first investigations into the formation of supramolecular assemblies of gold nanocluster as recyclable materials, and more interactions of gold nanoclusters based on ligand layer interactions through polymorphism studies and ligand exchange studies. These investigations all help understand how to control the ligand layer for future applications of gold nanoclusters and nanoparticles, from molecular to bulk materials.

TABLE OF CONTENTS

Chapter 1. Introduction to Gold Nanoclusters

Nano-gold materials are historically and recently interesting material to research for a variety of applications and other fundamental research. The long history of non-bulk gold materials starts with Michael Faraday with his synthesis and discovery of nano-scale gold and its different properties from bulk gold.[1–3] These nano-sized materials are easily produced with gold salts and a variety of reducing or protecting agents. Gold nanoparticles in the micron to five nanometer size have been industrially produced since then with numerous mundane to fascinating applications.[4–7] However, as synthetic control increased, even smaller gold nano-materials could be produced with their own differences in properties which made them desirable for modern research. The controlled synthesis and modern-day research of these ultra-small materials was jump-started into the popular scientific eye when Mathias Brust working with David Schiffrin created a synthesis that produced ultra-small, near-monodisperse, thiol-protected, gold nanoparticles which presented significantly different properties than the larger nanoparticles.[8,9] These ultra-small gold nanoclusters, as they are called, differ significantly from larger nanoparticles and offer greater research opportunities for their unique properties.

As the size of the nanoparticles decreases and the diameter of the particle nears the wavelength of an electron, quantum confinement begins to take place which significantly changes the way the particles behave. The fully metallic core of the nanoclusters allow electrons to freely move across the diameter. This creates a spherical potential well of freely moving electrons which in turn interact to create a completely new class of electronic orbitals that come from high rotational momentum.[10,11] These new orbitals seen in cluster materials have been investigated thoroughly in the gas phase and in other metal materials where it was seen that nanoclusters that were many times the size of a single atom could nevertheless behave just like a single atom based on their electronic structure.[12–15] These were coined superatoms. A useful model for approximating the electronic structure of these superatoms was created named the superatom/jellium model.[12,15,16] Superatomic orbitals are created from the interaction of the electrons in the core of a nanocluster and this model predicts the progression of those orbitals. These superatomic orbitals progress quickly from orbitals analogous to molecular orbitals like 1s and 1p orbitals to high angular quantum number orbitals such as 1g and 1h unseen in most other molecular systems.

Similar to octet closings, there is a noticeable stability that comes from the closing of superatomic orbitals with certain numbers of electrons. With gold nanoclusters protected by thiols, the number of electrons donated to the superatomic orbitals can be easily calculated with a simple equation seen in Equation 1.[11]

Equation 1.1 $$n^* = MV_a - N - z$$

With numbers of electrons that provide superatomic orbital shell closings, high stability is observed. These numbers of electrons correspond to specific numbers of gold atoms and ligands which are called “magic-sized clusters”. Unlike nanoparticles which are described by a range of sizes based on the monodispersity, nanoclusters are described by the exact number of gold atoms and ligands. The exact nanocluster being worked with can be known to atomic precision because of the stability that comes from electronic shell closings.

Since nanoclusters can be atomically precise and purified to near-perfect monodispersity, they can also be crystallized. Early work on nanoclusters was done with low accuracy mass spectrometry and other accompanying techniques, where most numbers of gold atoms and ligands were approximations and the structures were based on assumptions. The first nanocluster was then crystallized in 2007 by applying bio-macromolecule techniques to inorganic materials. [17] With the ability to compare crystallographically determined structures to the properties of a nanocluster, there is significant insight into the structure-function relationship which is missing from larger gold nanoparticles.

Figure 1.1 shows the structure building from the core to the ligand layer of the $Au_{102}(SR)_{44}$ gold nanocluster, according to the framework described by Pradeep.[18] The core

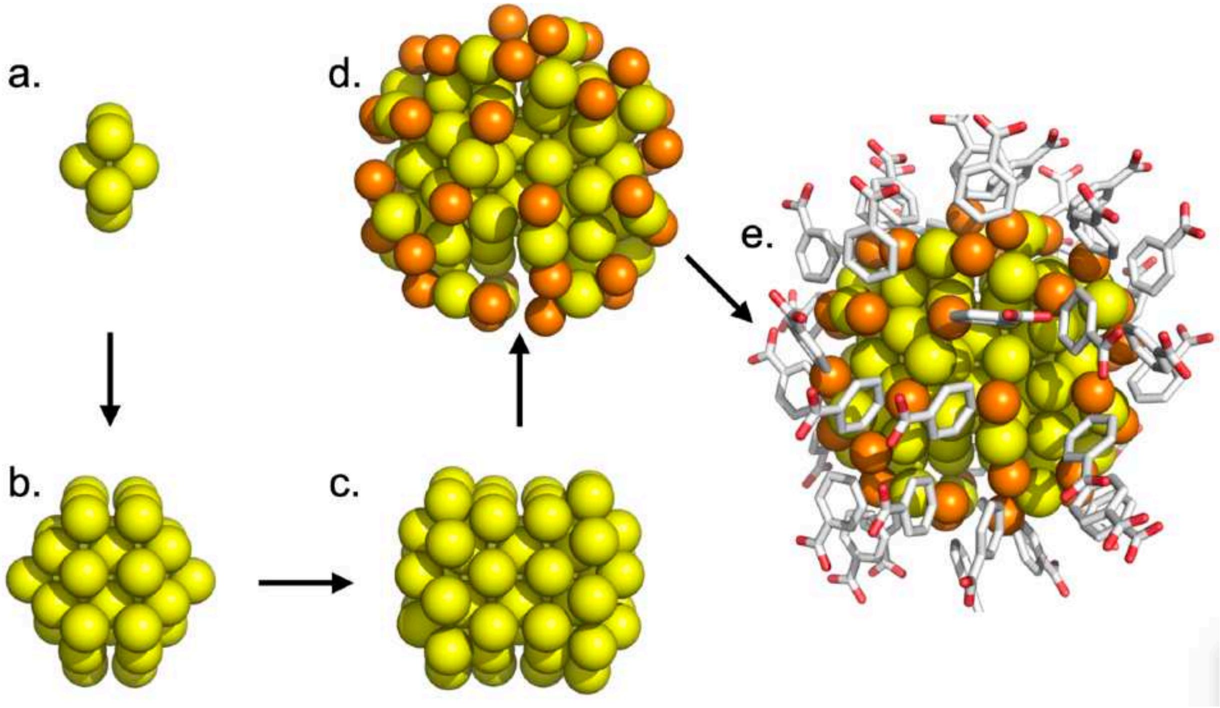

Figure 1.1. Images showing the structure of the $Au_{102}(pMBA)_{44}$ gold nanocluster as it build from the core Au^0 atoms in a-c, then the staple units of $S\text{-}Au^I\text{-}S$ added in d, then the rest of the ligands in e. Au represented in yellow, S represented in orange, C represented in light gray, O represented in red.

begins with geometric shells made of Au^0 atoms. These shells build geometrically and significant stability occurs from those shells. This is akin to the stability that occurs in some atomic nuclei from certain numbers of protons or neutrons.[10] Beyond these core Au^0 atoms are arranged the staple units of the nanocluster, that consist of S ligands and Au^I atoms. These can vary based on the different magic-sized cluster from single staples with S-Au-S, to longer staples with S-Au-S-Au-S. Different properties can come from either the core of the nanocluster or from the exterior golds and ligand layer.

Gold nanoclusters have been studied heavily for the past few decades for their unique properties. These studies have been varied from purely theoretical studies to experimental only studies and everything in between. Significant work has been put into understanding the properties that come from the core of the nanocluster like magnetism and optics, and the properties that come from the ligand layer and interaction with other materials.

Lots of research has been done on a variety of nanoclusters to examine the magnetism, optics and electronic behavior.[19–26] Changing the nuclearity, ligand, shape of nanoclusters, and oxidation state all can have an affect on these behaviors. Different nanocluster nuclearities result in different properties because of their different electron counts, frontier superatomic orbitals, and surface coverings. The ligands affect the stability, electronics, and interactions with other molecules, discussed below. The shape of the nanocluster changes the symmetry, stability, and ligand coverage and through this the properties of the nanocluster.[27–29] And the oxidation state, or electron count of the superatom can affect all these. Most interestingly to the first two chapters of this dissertation are the results of magnetic studies from this lab and others in the field showing the oxidation state-dependent magnetism of gold nanoclusters and their possible applications[30–35] and how the ligands on a nanocluster can affect it's intramolecular interactions.

While significant work has been done to understand the properties of smaller nanoclusters like $Au_{25}(SR)_{18}$ and $Au_{38}(SR)_{20}$, less research has been completed on larger nanoclusters. These smaller nanoclusters, including those that aren't easily described by the superatom/jellium model, have much more simple electronic structures and are generally easier to purify and crystallize than larger nanoclusters. Larger nanocluster could be better systems for certain applications for the ability to support higher magnetic spin counts and different electronics. They also may work better as model systems to understand how gold nanoparticles function as they are closer to these larger, non-quantum confined materials.

As gold nanoclusters increase in size the superatomic orbital progression goes from what might be called "normal" chemistry into completely new and different systems. With a quick increase in orbital angular momentum, nanoclusters can be researched that have frontier orbitals such as 1g and 1h. These electronic structures are far beyond what is usually worked with and their behavior cannot easily be predicted or explained once empirical data is collected. Any new data that is collected with these unique systems helps to better understand how they might be used for better applications or to understand other non-"normal" systems.

Along with more research on larger nanoclusters electronics and the origins of their unique properties, examinations of the way all nanoclusters interact with other materials or other nanoclusters is still important for any application that may be proposed. The ligand layer of the nanocluster controls how they interact with the world around them in solution or solid phase. Ligand exchange and interactions between clusters need to be further investigated for functionalization on surfaces and stability within solution as is discussed in the latter chapters of this dissertation.

Research has been performed from the Ackerson research group and plenty of others on ligand exchange and ligand interactions of small nanoclusters and a few larger nanoclusters. This research has varied from X-Ray crystallography based examinations to solution phase studies with NMR and mass spectrometry. It has been observed that ligand exchange occurs certain ways with small nanoclusters and with small numbers of ligands exchanged, however, do these trends happen the same way with larger nanoclusters or do ligand interactions stay the same with different ligands and in different solvents? These are questions that need to be investigated for any expansion of applications of gold nanoclusters.

In this dissertation, numerous studies have been performed to add to this gap in knowledge that remains in the gold nanocluster field. Starting with core based properties of gold nanoclusters, the magnetic properties of $Au_{102}(SR)_{44}$ and $Au_{133}(SR)_{52.}$ were investigated to further understand the electronic structure of these two larger gold nanoclusters. Evan's Method nuclear magnetic resonance spectroscopy (NMR) was used, a solution phase magnetic investigation technique, to study the magnetic susceptibility of these nanoclusters. This technique relies on the interaction of a sample of interest in solution with an internal standard to view the magnetic behavior. These studies were performed in order to better understand the gold nanocluster's electronic structure and behavior as their oxidation state was altered. Observing the differences between these and previously investigated nanoclusters can give insight into superatomic orbitals in general and how these materials change as they get closer to gold nanoparticles in character.

Since the studies of $Au_{133}(SR)_{52}$ involve purification through crystallization, ligand exchange studies could be performed on the nanocluster to examine ligand interactions of the material compared to previously reported studies with smaller materials. Using X-ray crystallography, ligand structure is examined before and after ligands are changed on the surface of the nanocluster. The larger $Au_{133}(SR)_{52}$ gold nanocluster should be able to support larger ratios of exchanged ligands while still being able to crystallize compared to the well studied $Au_{25}(SR)_{18}$. Studies on the larger gold nanocluster with ligand exchanges can also give further insight to ligand exchange mechanisms on differently packed surfaces than smaller nanoclusters.

Further studies included are on the "captain of the great nanocluster ship", $Au_{25}(SR)_{18}$.[36] The controlled crystallization and the intercluster interactions of these nanoclusters in certain solvents is studied within this work. Careful control over the conditions in which the nanoclusters are crystallized results in different morphological changes both in the macro- and microscopic structures. The procedures and results from these different $Au_{25}(SR)_{18}$ crystals is discussed in detail. Looking at intercluster interactions through dynamic light scattering (DLS) to determine how they aggregate and behave with temperature, solvent, and concentration changes is also studied. Previous work has shown permanent fusion or covalent attachment between nanoclusters when aggregation is induced. However, reversible aggregation of supramolecular assemblies is seen herein where the size of the nanoclusters as well as the growth models that produce those assemblies can be examined.

Chapter 1 References

(1) Faraday, M. The Bakerian Lecture. —Experimental Relations of Gold (and Other Metals) to Light. *Phil. Trans. R. Soc.* **1857**, *147*, 145–181.

(2) Dass, A. Faradaurate Nanomolecules: A Superstable Plasmonic 76.3 KDa Cluster. *J. Am. Chem. Soc.* **2011**, *133* (48), 19259–19261.

(3) Sakthivel, N. A.; Theivendran, S.; Ganeshraj, V.; Oliver, A. G.; Dass, A. Crystal Structure of Faradaurate-279: Au 279(SPh- TBu) 84Plasmonic Nanocrystal Molecules. *J. Am. Chem. Soc.* **2017**, *139* (43), 15450–15459.

(4) Daniel, M.-C.; Astruc, D. Gold Nanoparticles: Assembly, Supramolecular Chemistry, Quantum-Size-Related Properties, and Applications toward Biology, Catalysis, and Nanotechnology. *Chem. Rev.* **2004**, *104* (1), 293–346.

(5) Ertem, E.; Diez-Castellnou, M.; Ong, Q. K.; Stellacci, F. Novel Sensing Strategies Based on Monolayer Protected Gold Nanoparticles for the Detection of Metal Ions and Small Molecules. *Chem. Rec. (New York, N.Y.)* **2017**, *53*, 1756.

(6) Giljohann, D. A.; Seferos, D. S.; Daniel, W. L.; Massich, M. D.; Patel, P. C.; Mirkin, C. A. Gold Nanoparticles for Biology and Medicine. *Angew. Chem.* **2010**, *49* (19), 3280–3294.

(7) Nealon, G. L.; Donnio, B.; Greget, R.; Kappler, J.-P.; Terazzi, E.; Gallani, J.-L. Magnetism in Gold Nanoparticles. *Nanoscale* **2012**, *4* (17), 5244–5258.

(8) Brust, M.; Fink, J.; Bethell, D.; Schiffrin, D. J.; Kiely, C. Synthesis and Reactions of Functionalised Gold Nanoparticles. *J. Chem. So., Chem. Comm.* **1995**, No. 16, 1655–1656.

(9) Brust, M.; Walker, M.; Bethell, D.; Schiffrin, D. J.; Whyman, R. Synthesis of Thiol-Derivatised Gold Nanoparticles in a Two-Phase Liquid–Liquid System. *J. Chem. So., Chem. Comm.* **1994**, *0* (7), 801–802.

(10) Bergmann, T.; Göhlich, H.; Physical, T. L. T. J. of; 1991. Shell Structure of Clusters. *ACS Publications*.

(11) Walter, M.; Akola, J.; Lopez-Acevedo, O.; Jadzinsky, P. D.; Calero, G.; Ackerson, C. J.; Whetten, R. L.; Grönbeck, H.; Häkkinen, H. A Unified View of Ligand-Protected Gold Clusters as Superatom Complexes. *Proc. Natl. Acad. Sci.* **2008**, *105* (27), 9157–9162.

(12) Jena, P. Beyond the Periodic Table of Elements: The Role of Superatoms. *J. Phys. Chem. Lett* **2013**, *4* (9), 1432–1442.

(13) Castleman Jr, A. W. From Elements to Clusters: The Periodic Table Revisited. *J. Phys. Chem. Lett* **2011**, *2* (9), 1062–1069.

(14) Castleman Jr, A. W.; Khanna, S. N. Clusters, Superatoms, and Building Blocks of New Materials. *J. Phys. Chem. C* **2009**, *113* (7), 2664–2675.

(15) Reber, A. C.; Khanna, S. N.; Castleman, A. W. Superatom Compounds, Clusters, and Assemblies: Ultra Alkali Motifs and Architectures. *J. Am. Chem. Soc.* **2007**, *129* (33), 10189–10194.

(16) Liu, F.; Mostoller, M.; Kaplan, T.; Khanna, S. N.; Jena, P. Evidence for a New Class of Solids. First-Principles Study of K(Al13). *Chemical Physics Letters* **1996**, *248* (3–4), 213–217.

(17) Jadzinsky, P. D.; Calero, G.; Ackerson, C. J.; Bushnell, D. A.; Kornberg, R. D. Structure of a Thiol Monolayer-Protected Gold Nanoparticle at 1.1 A Resolution. *Science* **2007**, *318* (5849), 430–433.

(18) Natarajan, G.; Mathew, A.; Negishi, Y.; Whetten, R. L.; Pradeep, T. A Unified Framework for Understanding the Structure and Modifications of Atomically Precise Monolayer Protected Gold Clusters. *J. Phys. Chem. C* **2015**, *119* (49), 27768–27785.

(19) Dass, A.; Theivendran, S.; Nimmala, P. R.; Kumara, C.; Jupally, V. R.; Fortunelli, A.; Sementa, L.; Barcaro, G.; Zuo, X.; Noll, B. C. $Au_{133}(SPh\text{-}TBu)_{52}$ Nanomolecules: X-Ray Crystallography, Optical, Electrochemical, and Theoretical Analysis. *J. Am. Chem. Soc.* **2015**, *137* (14), 4610–4613.

(20) Jones, T. C.; Sumner, L.; Ramakrishna, G.; Hatshan, M. bin; Abuhagr, A.; Chakraborty, S.; Dass, A. Bulky T-Butyl Thiolated Gold Nanomolecular Series: Synthesis, Characterization, Optical Properties, and Electrocatalysis. *J. Phys. Chem. C* **2018**,.

(21) Koivisto, J.; Malola, S.; Kumara, C.; Dass, A.; Häkkinen, H.; Pettersson, M. Experimental and Theoretical Determination of the Optical Gap of the Au144(SC2H4Ph)60 Cluster and the $(Au/Ag)_{144}(SC_2H_4Ph)_{60}$ Nanoalloys. *J. Phys. Chem. Lett* **2012**, *3* (20), 3076–3080.

(22) Nimmala, P. R.; Yoon, B.; Whetten, R. L.; Landman, U.; Dass, A. Au(67)(SR)(35) Nanomolecules: Characteristic Size-Specific Optical, Electrochemical, Structural Properties and First-Principles Theoretical Analysis. *J. Phys. Chem. A* **2013**, *117* (2), 504–517.

(23) Rambukwella, M.; Sementa, L.; Barcaro, G.; Fortunelli, A.; Dass, A. Organosoluble Au 102(SPh) 44Nanomolecules: Synthesis, Isolation, Compositional Assignment, Core Conversion, Optical Spectroscopy, Electrochemistry, and Theoretical Analysis. *J. Phys. Chem. C.* **2015**, *119* (44), 25077–25084.

(24) Zhu, M.; Aikens, C. M.; Hollander, F. J.; Schatz, G. C.; Jin, R. Correlating the Crystal Structure of A Thiol-Protected Au 25Cluster and Optical Properties. *J. Am. Chem. Soc.* **2008**, *130* (18), 5883–5885.

(25) Yi, C.; Tofanelli, M. A.; Ackerson, C. J.; Knappenberger, K. L. Optical Properties and Electronic Energy Relaxation of Metallic Au144(SR)60 Nanoclusters. *J. Am. Chem. Soc.* **2013**, *135* (48), 18222–18228.

(26) AbdulHalim, L. G.; Hooshmand, Z.; Parida, M. R.; Aly, S. M.; Le, D.; Zhang, X.; Rahman, T. S.; Pelton, M.; Losovyj, Y.; Dowben, P. A.; Bakr, O. M.; Mohammed, O. F.; Katsiev, K. PH-Induced Surface Modification of Atomically Precise Silver Nanoclusters: An Approach for Tunable Optical and Electronic Properties. *Inorg. Chem.* **2016**, *55* (21), 11522–11528.

(27) Day, P. N.; Pachter, R.; Nguyen, K. A.; Bigioni, T. P. Linear and Nonlinear Optical Response in Silver Nanoclusters: Insight from a Computational Investigation. *J. Phys. Chem. A* **2016**, *120* (4), 507–518.

(28) Van Steerteghem, N.; Van Cleuvenbergen, S.; Deckers, S.; Kumara, C.; Dass, A.; Häkkinen, H.; Clays, K.; Verbiest, T.; Knoppe, S. Symmetry Breaking in Ligand-Protected Gold Clusters Probed by Nonlinear Optics. *Nanoscale* **2016**, *8* (24), 12123–12127.

(29) Qian, H.; Zhu, M.; Gayathri, C.; Gil, R. R.; Jin, R. Chirality in Gold Nanoclusters Probed by NMR Spectroscopy. *ACS Nano* **2011**, *5* (11), 8935–8942.

(30) Zhu, M.; Aikens, C. M.; Hendrich, M. P.; Gupta, G.; Qian, H.; Schatz, G. C.; Jin, R. Reverisible Switching of Magnetism in Thiolate-Protected Au_{25} Superatoms. *J. Am. Chem. Soc.* **2009**, *131* (7), 2490–2492.
(31) Herbert, P. J.; Window, P.; Ackerson, C. J.; Knappenberger, K. L. Low Temperature Magnetism in Nanoscale Gold Revealed Through Variable-Temperature Magnetic Circular Dichroism Spectroscopy. *J. Phys. Chem. Lett* **2018**, *10* (2), 189–193.
(32) Tofanelli, M. A.; Salorinne, K.; Ni, T. W.; Malola, S.; Newell, B.; Phillips, B.; Häkkinen, H.; Ackerson, C. J. Jahn–Teller Effects in $Au_{25}(SR)_{18}$. *Chem. Sci.* **2016**, *7* (3), 1882–1890.
(33) Zeng, C.; Weitz, A.; Withers, G.; Higaki, T.; Zhao, S.; Chen, Y.; Gil, R. R.; Hendrich, M.; Jin, R. Controlling Magnetism of $Au_{133}(TBBT)_{52}$ Nanoclusters at Single Electron Level and Implication for Nonmetal to Metal Transition. *Chem. Sci.* **2019**, *10* (42), 9684–9691.
(34) Collins, C. B.; Tofanelli, M. A.; Noblitt, S. D.; Ackerson, C. J. Electrophoretic Mechanism of $Au_{25}(SR)_{18}$ Heating in Radiofrequency Fields. *J. Phys. Chem. Lett* **2018**, *9* (7), 1516–1521.
(35) McCoy, R. S.; Choi, S.; Collins, G.; Ackerson, B. J.; Ackerson, C. J. Superatom Paramagnetism Enables Gold Nanocluster Heating in Applied Radiofrequency Fields. *ACS nano* **2013**, *7* (3), 2610–2616.
(36) Kang, X.; Chong, H.; Zhu, M. Au25(SR)18: The Captain of the Great Nanocluster Ship. *Nanoscale* **2018**, *10* (23), 10758–10834.

Chapter 2. Superatom Paramagnetism of $Au_{102}(SPh)_{44}^{(-1/0/+1/+2)}$ Oxidation States*

2.1 Synopsis

Gold nanoclusters show distinctive magnetic properties and electronic structure from many molecular systems. Nanoclusters of sufficiently small size restructure geometrically to stabilize electronically (e.g. a Jahn-Teller effect) whereas geometric distortion may not be possible in larger nanoclusters. In this work, the charge state dependent magnetism of the $Au_{102}(SPh)_{44}^{-1/0/+1/+2}$ nanocluster is investigated through Evans Method NMR measurements. The +2 charge state is shown as paramagnetic. This suggests that the nanocluster does not distort geometrically to pair electrons. Because the nanocluster lies within the transition range of molecule-like to bulk-like properties, this suggests that the geometric stabilization that becomes important in larger 'magic number clusters' may be resistant to electronically driven distortions observed in smaller nanoclusters.

2.2 Introduction

Magnetism in nanoclusters and particles of gold is historically an area of conflicting results.[1,2] Production of gold nanoclusters with tighter control of oxidation state and better monodispersity has helped resolve many early problems and conflicts. There is still, however, the unclear role of structural distortion in certain gold clusters that might change how magnetizable a cluster could be.

---

* *The work presented herein is published in Inorganic Chemistry with Phillip S. Window and Christopher J. Ackerson as coauthors. Phillip S. Window's contributions include experimental design, data analysis, and synthetic development and characterization of gold nanoclusters and assemblies. Window, P. S.; Ackerson, C. J. Inorg Chem* ***2020****, 59 (6), 3509–3512.*

When considering particles of gold in progressively smaller sizes, the melting temperature of the particle decreases, such that 2.5 nm diameter particles are calculated as quasi-molten at room temperatures.[3,4] This decrease in melting point (e.g., rigidity) is concurrent with the disappearance of magnetic properties of bulk gold (diamagnetism) and emergence of the possibility of para- ferro- and anti-ferromagnetic properties.[5,6]

On the smaller side of atomically precise gold clusters, the magnetic properties of $Au_{25}(SR)_{18}$ are especially well studied. $Au_{25}(SR)_{18}$ exhibits molecular like electronic charge state transitions and has Jahn-Teller like distortions in the electronic and geometrics structure of the superatom.[7] In Maran's work, paramagnetism, superparamagnetism, and ferromagnetism were all observed with solid state samples of $Au_{25}(SR)_{18}^0$ in EPR experiments through different magnetic ordering.[8] However, the $Au_{25}(SR)_{18}$ cluster does not support greater than S=1/2, as seen in Tofanelli's work. This is because $Au_{25}(SR)_{18}$ is sufficiently structurally fluid to accommodate Jahn-Teller distortion, which resolves electronic degeneracy with structural distortions.

An open question that builds upon the interplay of structure and magnetism in gold clusters is if larger clusters resist electronic degeneracy driven distortions (e.g., are not subject to Jahn-Teller effects) while at the same time retaining other molecular-like electronic and magnetic properties. To address this question, we measured the magnetic properties of $Au_{102}(SPh)_{44}$ in a set of 4 different oxidation states.

2.3 Results and Discussion

In this work, the charge state dependent paramagnetism of $Au_{102}(SPh)_{44}$ is investigated. Paramagnetism has already been observed in $Au_{102}(SR)_{44}$ through charge state changes[6] and low temperature modifications[9;] however, these observations have not shown how magnetizable the clusters could be and how many unpaired electrons could be sustained. Applying techniques developed for examining magnetism of large biomolecules by Piguet through Evan's Method NMR experiments[10] the diamagnetic correction could be measured directly instead of calculated and the paramagnetism can be measured in different charge states.[11] (See Equation 1) Bulk electrolysis was used with the nanocluster to study the -1, 0, +1, and +2 charge. The 0 charge state of the nanocluster is predicted to have a superatomic electron configuration of $1S^2$ | $1P^6$ | $1D^{10}$ | $2S^2$ $1F^{14}$ | $2P^6$ $1G^{18}$ based on the idealized superatom/jellium model theory for spherical particles. This corresponds to 58 superatomic electrons. The positive charge states of the $Au_{102}(SPh)_{44}$ nanocluster would then have unpaired electrons in the 1G orbital and the negative charge state would have unpaired electrons added to the 2D superatomic orbital. DFT studies

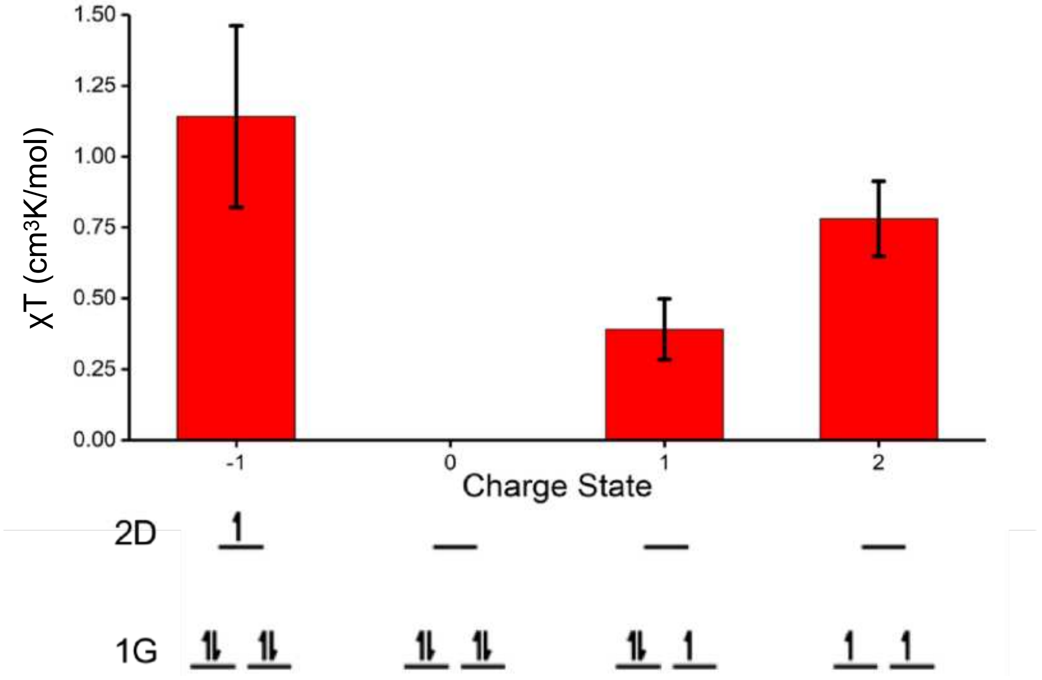

Figure 2.1 Graph showing χT values at different charge states with electron configurations of charge states shown directly below charge state axis. (1G orbital simplified to top two states for clarity)

have show these frontier orbitals are a manifold of 1H, 2D, 3S orbitals.[12] However, a 2D frontier orbital is used herein for simplification.

The $Au_{102}(SPh)_{44}$ nanocluster exhibited paramagnetism in the -1, +1, and +2 charge states, as seen in Figure 2.1. This shows the different behavior that this large cluster has from the $Au_{25}(SR)_{18}$ nanocluster in that when the second electron was removed from the superatomic orbitals, the orbital does not restructure to pair the electrons as was seen with $Au_{25}(SR)_{18}$. This suggests that the core of the $Au_{102}(SPh)_{44}$ nanocluster is more structurally rigid than previously thought. This implies that the geometric stabilization of the larger clusters could be more prevalent than the electronic stabilization seen in smaller clusters. It was also observed that the "0" charge state well of the nanocluster was not in the assumed position in a Square Wave Voltammogram (SWV). This was found through the magnitude of the diamagnetic response of the different charge states examined.

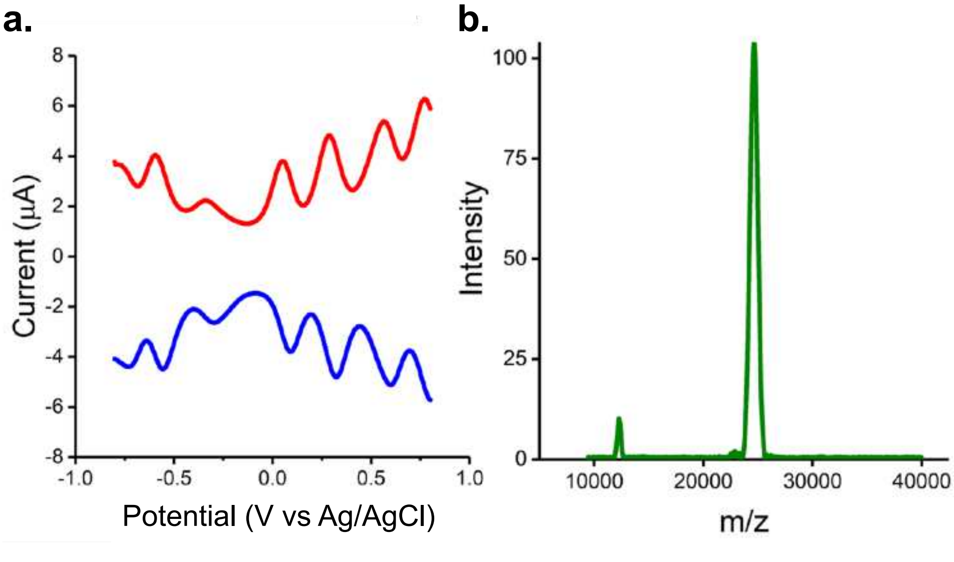

Figure 2.2 a. Square wave voltammogram of $Au_{102}(SPh)_{44}$ with red and blue traces showing positive and negative potential sweeps, respectively. b. MALDI-MS spectrum of $Au_{102}(SPh)_{44}$ showing purity with parent peak centered at 25000 m/z and doubly charged sample peak at 12500 m/z. (* represents fragment)

$Au_{102}(SPh)_{44}$ was synthesized using a modified protocol from Rambukwella.[13] Full details, purification and characterization are given in the supplemental information (SI.) Figure 2.2 shows mass spectrometry and electrochemical analysis of the purified nanocluster, which matches previously published results. Any changes in observed electrochemical data from other $Au_{102}(SR)_{44}$ results are attributed to the different ligand shell. There were no observable changes in these data above after oxidation state modifications and purity was assured regularly throughout experimentation. UV-Vis spectrometry was performed on the cluster (Figure S2) and no significant change was seen after oxidation state modifications. Bulk electrolysis was used to set the oxidation state (and therefore the electron count) of the superatom to produce $Au_{102}(SPh)_{44}^{-1/0/+1/+2}$ samples which is regularly used for charge state modifications on superatom nanoclusters such as $Au_{25}(SR)_{18}$. Since these electrochemical redox processes are reversible, they are assumed to not be ligand redox events. The magnetic response of each $Au_{102}(SPh)_{44}$ oxidation state was determined through Evan's Method. Explanation and full details are given in the appendix I.

In Equation 2.1, developed by Piguet, $\delta\nu$ is the difference between the tetramethylsilane (TMS) peaks in the Evan's Method NMR experiments from the capillary TMS and the TMS with the sample. *M* is the molar mass of the sample and *m* is the mass of sample used in the experiment. This accounts for the diamagnetic correction in the equation without a theoretical calculation since both charge states use the same salt concentration and solvent.

Equation 2.1

$$X_M^p = \frac{1}{\nu_0 S_f}\left[\frac{\delta v^p M^p}{m^p} - \frac{\delta v^{dia} M^{dia}}{m^{dia}}\right]$$

This equation calculated the paramagnetic molar susceptibility of a sample based on subtracting the molar pseudocontact shift of the diamagnetic analogue of the nanocluster (the “0” charge state) from the molar pseudocontact shift of the +1, +2, or -1 charge state nanoclusters to obtain the molar paramagnetic response of the pseudocontact shift peak. The difference between these TMS shifts are then divided by ν_0, the operating frequency of the NMR (400MHz), and S_f, the shape factor of the magnet (4π/3). This equation was developed for solving the diamagnetic correction for large paramagnetic molecules such as proteins where the diamagnetic contribution is as large or larger than the paramagnetic contribution from the molecule.

Table 2.1. List of magnetic study data comparing χT's of different charge states of $Au_{102}(SPh)_{44}$.

Charge State	Avg. Molar Shift (Hz*cm^3/mol)	χT (cm^{3}K/mol)	Std. Dev.
-1	-5.36E+06	1.14	0.321
0	-1.17E+07	0	0
1	-9.55E+06	0.390	0.107
2	-7.37E+06	0.781	0.132

Table 2.1 shows the calculated molar shifts of the TMS peaks and the subsequent χT’s of each charge state. Here we see that the +1 and +2 charge state have χT’s of 0.390 cm^{3}K/mol ± 0.107 and 0.781 cm^{3}K/mol ± 0.132. This data shows immediately the difference between the smaller $Au_{25}(SR)_{18}$ nanocluster and $Au_{102}(SPh)_{44}$. $Au_{25}(SR)_{18}$ undergoes a Jahn-Teller-like distortion when losing two electrons to become diamagnetic. Whereas, the $Au_{102}(SPh)_{44}$ sample increases its χT from 0.390 cm^{3}K/mol to 0.781 cm^{3}K/mol when losing another electron to more than double its paramagnetic response. This demonstrates that electron pairing energy does not dominate in the higher rotational energy orbitals of the HOMO. Table 2.1 and Figure 2.1 also show the χT of the -1 charge state to be 1.14 cm^{3}K/mol ± 0.321. This is a significantly higher

value than would expected for a s=0.5 sample. The larger χT could be due to several factors including intercluster interactions like ferromagnetic coupling. Since a possible location of these electrons is in the 2D superatomic orbital, the behavior makes sense as the unpaired electron is free to interact more easily in the higher quantum number orbital with adjacent orbitals.

Previous work in the field of cluster magnetism found that $Au_{25}(SR)_{18}$ materials had g factors greater than 2 with Marcus Tofanelli's work in SQuID magnetometry and Flavio Maran's work in EPR. Tofanelli's work found a g factor of 2.18 for $Au_{25}(SR)_{18}$ clusters. Using Tofanelli's value as an approximation, a χT can be roughly predicted through Curie's Law. A χT of 0.4455 cm^3K/mol is found for an s = 1/2 cluster similar to $Au_{25}(SR)_{18}$ and a χT of 1.1881 cm^3K/mol is predicted for an s=1 cluster. The significantly smaller experimental χT of the "+2" or s = 1 cluster could be due to partial electron pairing and spin-orbit coupling. Since the superatomic orbitals are an extremely complex system, the approximation of the χT's through Curie's Law should be calculated through the total angular momentum in each charge state. However, with such complexity, the calculations needed for this are improbable to model and computationally expensive, such as work done with F orbital models. EPR spectroscopy was also performed on the cluster (data not shown) and no signal was observed at 140K. Based on this signal, we concluded that the paramagnetism measured with Evan's Method came from the nanocluster and not any contaminant. Lower EPR measurement temperatures are required to observe the superatom paramagnetism observed by Evan's method in this paper.[8]

2.4 Conclusion

The Evan's Method magnetic data collected for $Au_{102}(SPh)_{44}$ allows for the first empirical analysis of the electronic structure and electron pairing of this large nanocluster. By observing this increase in the paramagnetism of the cluster from one to two electrons removed, there is not significant pairing of the electrons or Jahn-Teller-like distortions to the electronic structure as seen with the $Au_{25}(SR)_{18}$ nanocluster. Jahn-Teller effects are improbable to observe through structural data due to the lack of crystallization of the cluster so far. It also appears that the charge state assignments are different than one might expect when viewing a HOMO-LUMO gap from electrochemical data. Figure S1 in the SI show these charge state assignments and explain the assignments. This could have a serious impact when viewing electrochemical data on larger clusters that are less molecular than smaller clusters.

Further work needs to be done beyond these magnetic measurements on the different charge states to get a full picture of the electronic structure and its impact on the stability of the cluster. Variable-Temperature Evan's Method NMR experiments could confirm and give more information on the electronic structure and environment of the unpaired electrons in the superatomic orbitals. Differential scanning calorimetry can be used on this cluster in different charge states as well to see how the thermal stability of this cluster changes as the HOMO-LUMO occupancy changes. However, as found with $Au_{144}(SR)_{60}$, larger clusters can have unpredictable stability from charge state differences.[14] Future investigation into other spherical nanoclusters between $Au_{25}(SR)_{18}$ and $Au_{102}(SR)_{44}$ could be helpful to see the cluster-size dependent trend of electronic versus geometric stabilization, such as the nearly spherical $Au_{67}(SR)_{35}$.

Chapter 2 References

(1) Singh, R. Unexpected Magnetism in Nanomaterials. *J. Magn. Magn. Mater.* **2013**, *346*, 58–73.

(2) Nealon, G. L.; Donnio, B.; Greget, R.; Kappler, J.-P.; Terazzi, E.; Gallani, J.-L. Magnetism in Gold Nanoparticles. *Nanoscale* **2012**, *4* (17), 5244–5258.

(3) Buffat, Ph.; Borel, J.-P. Size Effect on the Melting Temperature of Gold Particles. *Phys. Rev. A* **1975**, *13* (6), 2287–2298.

(4) Marks, L. D. Experimental Studies of Small Particle Structures. *Rep. Prog. Phys.* **1994**, *57*, 603–649.

(5) Zhu, M.; Aikens, C. M.; Hendrich, M. P.; Gupta, G.; Qian, H.; Schatz, G. C.; Jin, R. Reverisible Switching of Magnetism in Thiolate-Protected Au_{25} Superatoms. *J. Am. Chem. Soc.* **2009**, *131* (7), 2490–2492.

(6) McCoy, R. S.; Choi, S.; Collins, G.; Ackerson, B. J.; Ackerson, C. J. Superatom Paramagnetism Enables Gold Nanocluster Heating in Applied Radiofrequency Fields. *ACS Nano* **2013**, *7* (3), 2610–2616.

(7) Tofanelli, M. A.; Salorinne, K.; Ni, T. W.; Malola, S.; Newell, B.; Phillips, B.; Häkkinen, H.; Ackerson, C. J. Jahn–Teller Effects in $Au_{25}(SR)_{18}$. *Chem. Sci.* **2016**, *7* (3), 1882–1890.

(8) Agrachev, M.; Antonello, S.; Dainese, T.; Ruzzi, M.; Zoleo, A.; Apr, E.; Govind, N.; Fortunelli, A.; Sementa, L.; Maran, F. Magnetic Ordering in Gold Nanoclusters. *ACS Omega* **2017**, *2* (6), 2607–2617.

(9) Herbert, P. J.; Window, P.; Ackerson, C. J.; Knappenberger, K. L. Low Temperature Magnetism in Nanoscale Gold Revealed Through Variable-Temperature Magnetic Circular Dichroism Spectroscopy. *J. Phys. Chem. Lett.* **2018**, *10* (2), 189–193.

(10) Evans, D. F. The Determination of the Paramagnetic Susceptibility of Substances in Solution by Nuclear Magnetic Resonance. *J. Chem. Soc.* **1959,** *400*, 2003-2005

(11) Piguet, C. Paramagnetic Susceptibility by NMR: The “Solvent Correction” Removed for Large Paramagnetic Molecules. *J. Chem. Educ.* **1997**, *74* (7), 815.

(12) Walter, M.; Akola, J.; Lopez-Acevedo, O.; Jadzinsky, P. D.; Calero, G.; Ackerson, C. J.; Whetten, R. L.; Grönbeck, H.; Häkkinen, H. A Unified View of Ligand-Protected Gold Clusters as Superatom Complexes. *PNAS* **2008**, *105* (27), 9157–9162.

(13) Rambukwella, M.; Sementa, L.; Barcaro, G.; Fortunelli, A.; Dass, A. Organosoluble $Au_{102}(SPh)_{44}$ Nanomolecules: Synthesis, Isolation, Compositional Assignment, Core Conversion, Optical Spectroscopy, Electrochemistry, and Theoretical Analysis. *J. Phys. Chem. C.* **2015**, *119* (44), 25077–25084.

(14) Tofanelli, M. A.; Ackerson, C. J. Superatom Electron Configuration Predicts Thermal Stability of $Au_{25}(SR)_{18}$ Nanoclusters. *J. Am. Chem. Soc.* **2012**, *134* (41), 16937–16940.

Chapter 3. Preliminary Investigations into Oxidation State Dependent Magnetism of $Au_{133}(tBBT)_{52}$†

3.1 Synopsis

Gold nanocluster properties follow a strong size-dependent trend, molecular behavior on the small side and bulk on the large side. Investigating these size-dependent trends is the best way to understand how to select certain size nanoclusters for certain future applications. Herein, the very large, but still molecular, $Au_{133}(tBBT)_{52}$ nanocluster's magnetism is studies and compared to smaller nanoclusters. Evan's Method ^1H NMR is performed on the nanocluster after oxidation state changes showing paramagnetism in the 0/+1/+2 oxidation states and diamagnetism in the -1 oxidation state, contrary to previously published data. Through these studies, the behavior of the unprecedented 1H superatomic orbital can be elucidated from the magnetic susceptibilities.

3.2 Introduction

Gold nanoclusters are interesting materials for research into fairly unknown systems such as superatomic orbitals. Ligated nanoclusters are stable materials to perform research with and allow for facile investigations into the behavior of the rare superatomic materials. Since their behavior and properties are those between molecular and bulk materials, depending on the size, those properties are a balance of geometric and electronic factors, nuclearity and oxidation state, core properties and ligand properties. One of those interesting properties is magnetism, which in nanomaterial gold is a phenomenon that only comes when the particles become sufficiently small to behave like superatoms or at sufficiently low temperature.[1–7] Magnetism is also a property that

---

† *The work presented herein includes contributions from Phillip S. Window that include experimental design, data analysis, synthesis, and characterization.*

can be investigated in order to more fully understand the unique electronic structure of gold nanoclusters.[8–10]

Previously within this dissertation the magnetism of $Au_{102}(SR)_{44}$ was investigated and the electronic structure was elucidated of this nanocluster.[11] $Au_{102}(SR)_{44}$ magnetism arises from superatom electrons within the 1G and 1H superatomic orbital. The nanocluster was shown to support up to 2 unpaired electrons within the 1G orbital after oxidation. The ability to empirically examine electronic structure within these unique orbitals makes these nanoclusters very interesting for further research. The $Au_{102}(SR)_{44}$ system, however, is from an ultra-stable closed orbital system and still presents molecular behavior. $Au_{102}(SR)_{44}$ is also considered the largest gold nanocluster to still have an observable optical gap. As the size of the nanoclusters increases this molecular behavior decreases further and with the $Au_{133}(SR)_{52}$ nanocluster the electronic stability comes from a half filled rather than a closed shell system.

$Au_{133}(SR)_{52}$ has been researched recently for its oxidation state-dependent magnetism through an EPR study in two different oxidation states.[12] This study found that in the “0” oxidation state, the nanocluster has a s = 1/2 spin with the electron having 1H orbital character. When oxidized through exposure to H_2O_2, the nanocluster becomes diamagnetic which can be reversed through later chemical reduction. This study provided a basis for research into the magnetic properties of the nanocluster. However, the use of chemical reduction and oxidation does not allow for fine control of the oxidation state of the nanocluster nor the further study of more accessible oxidation states.

An important question to answer in this field is what influences nanocluster property changes as the size of the nanoclusters and their atom count changes. There have been many attempts to classify the cutoff of where a molecular nanocluster size ends and a bulk material starts. However, when looking at all the properties and

Within this study, the solution magnetic susceptibility of $Au_{133}(SR)_{52}$ is studied in different oxidation states with Evan's Method 1H NMR and electrochemical electrolysis oxidation state changes.[13] The results of this study show interesting changes to the magnetism of the nanocluster as electrons are added and removed to the half-filled superatomic orbital. There are noticeable differences to the behavior of the superatomic electrons in this system from the previously studied $Au_{102}(SR)_{44}$ nanocluster. Electrochemical analysis is also discussed with small changes to the voltammogram as the oxidation state of the nanocluster is changed through bulk electrolysis.

3.3 Methods

In this work, the charge state dependent paramagnetism of $Au_{133}(tBBT)_{52}$ is investigated through Evan's Method NMR magnetic measurements after electrochemical changes to the oxidation state of the nanocluster. The $Au_{133}(tBBT)_{52}$ samples were synthesized using a modified literature preparation and purified through crystallization.[14] Full synthetic details are in the appendix for this chapter. In short, $Au_{144}(PET)_{60}$ was first synthesized using a one-phase Brust-Schiffrin synthesis.[15] The published time scale for the reaction was extended for better yield of $Au_{144}(PET)_{60}$ over $Au_{25}(PET)_{18}$. The crude was then purified through size exclusion chromatography (SEC). The $Au_{144}(PET)_{60}$ crude sample was then converted into $Au_{133}(tBBT)_{52}$ through ligand exchange thermo-etching or LEIST (ligand exchange induced size transformation). The $Au_{133}(tBBT)_{52}$ nanocluster was then crystallized from this crude sample through a dichloromethane/acetonitrile layering. Moving forward with only crystallized sample was the best way to ensure the best purity of the sample possible since MALDI-TOF MS with large clusters has a very large envelope around the molar mass of the material that only indicates the rough size of the material.

To measure the magnetic susceptibility of the $Au_{133}(tBBT)_{52}$ in different oxidation states, electrochemical bulk electrolysis was used first on the sample to examine the voltammogram then electrolyze the sample to the desired oxidation state well. Figure 3.1 shows the square wave voltammogram (SWV) with the oxidation state assignments based on the HOMO-LUMO gap as the largest potential gap being the electron count of the superatom that should be most stable.

After cleaning the sample of the electrochemical salts through different anti-solvent washes, Evan's Method NMR was used to find the magnetic susceptibility of the material through its interactions with the tetramethylsilane (TMS) standard added to the solution. As

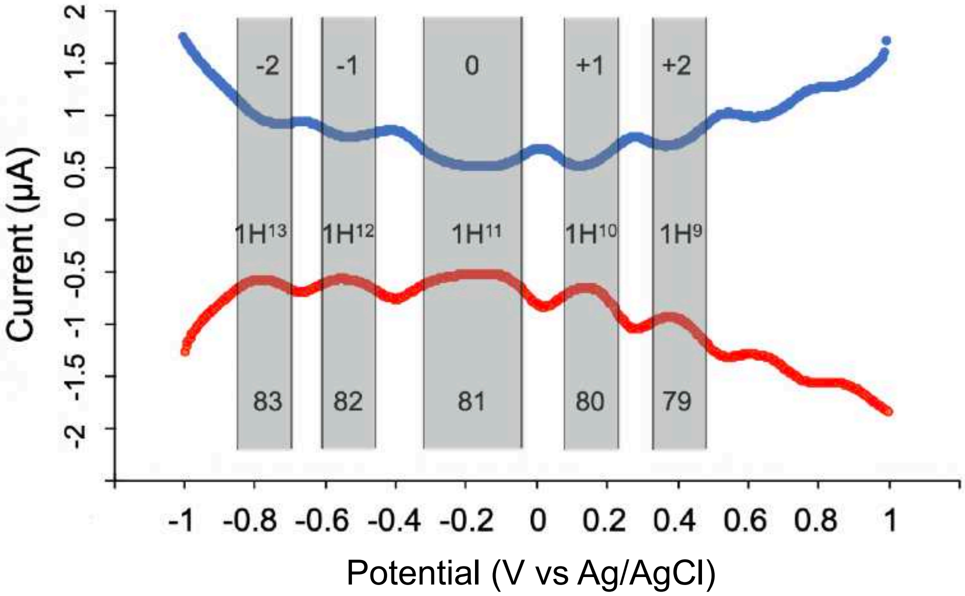

Figure 3.1. Square wave voltammogram of $Au_{133}(tBBT)_{52}$ with overlay of different oxidation state wells with: top text showing oxidation state of the nanocluster, middle text showing the frontier orbital electron count, and bottom text showing the total superatomic electron count of the nanocluster.

previously described in Chapter 2, Equation 2.1 was used to directly calculate the paramagnetic susceptibility of the different oxidation states subtracting out the diamagnetic moment of the nanocluster.[16]

3.4 Results and Discussion

Table 3.1 shows the average molar shift of the TMS peak found in the 1H NMR for each oxidation state. The oxidation state with the most negative TMS peak was determined to be the diamagnetic state of the nanocluster.

Table 3.1. List of magnetic study data comparing χT's of different charge states of $Au_{133}(tBBT)_{52}$.

Charge State	Avg. Molar Shift (Hz*cm^3/mol)x10^6	χT (cm^{3}K/mol)
-1	-9.52	N/A
0	-7.12	0.430
1	-5.1	0.792
2	-1.25	1.48

Figure 3.2 shows a graph comparing the susceptibility of the $Au_{133}(tBBT)_{52}$ nanocluster in its different oxidation states. The -1 oxidation state with the most negative TMS influence has no calculable magnetic susceptibility here with a molar TMS shift of -9.51*10^6 Hz*cm/mol. Assuming that the most stable oxidation state of the material is with a half filled H orbital in its 0 oxidation state, this is said to be within the HOMO LUMO gap as seen in Figure 3.1. In this 0 oxidation state, the molar TMS shift is less negative than that found in the -1 oxidation state. We can consider this a paramagnetic material here then. The 0 oxidation state has a χT susceptibility of 0.430 cm^{3}K/mol. This corresponds to an s = 1/2 system with a χT slightly lower than a free electron system with a g=2 at 0.447 cm^3/mol. As one electron is removed from the nanocluster system with the oxidation state assumed to be 0 and the nanocluster moves into the +1 oxidation

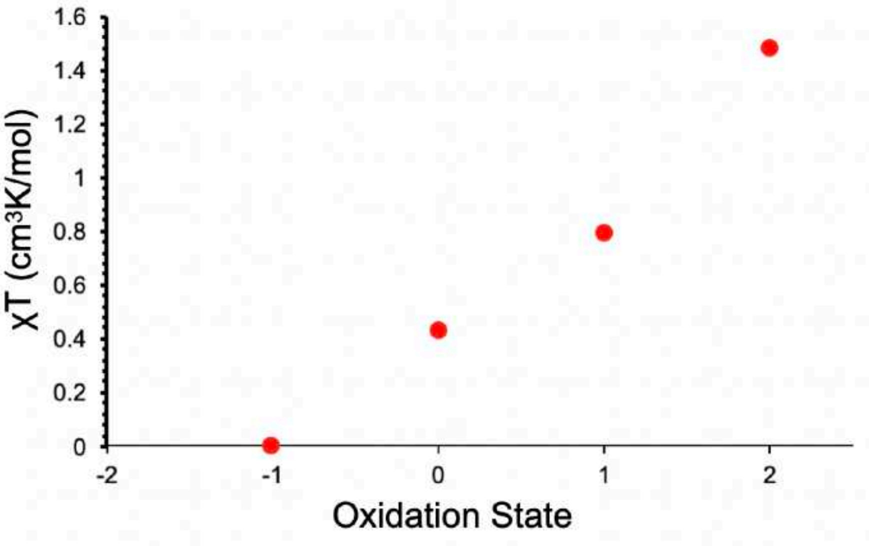

Figure 3.2. Graph showing the magnetic susceptibility in χT of $Au_{133}(tBBT)_{52}$ in different oxidation states. T = 300K (error bars are not available for this data due to the lack of adequate trials)

state, the χT susceptibility increases to 0.792 cm^3K/mol. This corresponds to around two unpaired electrons which differs significantly to previously published results by Zeng et al.[12] As another electron is removed from this system and it moves into the +2 oxidation state., the χT increases to 1.48 cm^3K/mol which is slightly lower susceptibility than a g = 2 free electron system with 3 unpaired electrons.

In Figure 3.1, one can see the numbers of electrons within the H orbital for each given oxidation state well. In the 0 oxidation state, with a half-filled H orbital there are 11 total electrons based on the superatom theory and so there must be one unpaired electron. The susceptibility shows this clearly with a χT of 0.447 cm^3K/mol. Both the +1 and +2 oxidation states correspond to one electron increases to this susceptibility. However, when comparing this to previously published results from Zeng, we see large differences. As previously discussed, they saw diamagnetism in the +1 oxidation state instead of paramagnetic susceptibility. This could be due to the sample being run at 2-25 K versus room temperature measurements. Similar to spin-crossover complexes, a transition from high to low spin could occur as the material is cooled. At those temperatures, the $Au_{133}(tBBT)_{52}$ sample run by Zeng was in a frozen glass solution of toluene and dichloromethane. These differences could possibly be explained with further studies into temperature dependent magnetism through variable temperature NMR, electron paramagnetic resonance, or SQuID magnetometry investigations. Interestingly, instead of being a two unpaired electron system when in the -1 oxidation state, we see pairing of the H orbital electrons and a diamagnetic sample. With 12 total electrons, this is possible to have

Comparison to $Au_{102}(SPh)_{44}$. Comparing the magnetic susceptibility in χT of $Au_{133}(tBBT)_{52}$ to that of $Au_{102}(SPh)_{44}$, similar trends are seen in the observed. As electrons are removed from the system, the remaining electrons remain unpaired in the +1 oxidation state for $Au_{133}(tBBT)_{52}$ compared to the +2 oxidation state for $Au_{102}(SPh)_{44}$ instead of shifting the core structurally to pair the remaining electons. We attributed this to high geometric rigidity for $Au_{102}(SPh)_{44}$ and it is reasonable that the same factors are at play with the even larger $Au_{133}(tBBT)_{52}$. Since core rigidity increases with particle size, $Au_{133}(tBBT)_{52}$ would be even more rigid and could support even more unpaired electrons out to the +3 oxidation state.[17,18] Data has not yet been gathered of this oxidation state since bulk electrolysis to this larger potential well has proved difficult so far.

When comparing the -1 oxidation state of the $Au_{133}(tBBT)_{52}$ and $Au_{102}(SPh)_{44}$ nanoclusters, we see differences in their behavior. As an electron is added to the $Au_{102}(SPh)_{44}$ system, the χT increases significantly. We attributed this to the electron being added to the 2D or 1H frontier orbital. In that case, these orbitals can interact more with surrounding nanoclusters, increasing the susceptibility through ferromagnetic coupling interactions. Another possibility is that as one electron is added to the higher orbital it prompts other electrons to be promoted and unpaired within that orbital as well. However, neither of these claims have yet been substantiated. As an electron is added to the 1H orbital of $Au_{133}(tBBT)_{52}$, it is added to a half-filled orbital and therefore no increase in χT is observed and instead the material is diamagnetic. Further studies with the -2 oxidation state should be performed but these must be performed strictly air-free for the chance of atmospheric oxidation is too great to easily handle. This is very difficult to perform as the electrochemical salts need to be removed before Evan's method 1H NMR experiments. These salts are removed best with selective solubility and centrifugation. Acetonitrile is the easiest to use for this but this solvent easily picks up oxygen and centrifugation is a technique that does not lead itself to air-free chemistry easily as the machines are large and the pellets fragile.

3.5 Conclusion

Presented within this chapter are the preliminary results of magnetic susceptibility measurements on $Au_{133}(tBBT)_{52}$ in four different oxidation states. The nanocluster was synthesized, purified, crystallized, electrolyzed, and measured for its magnetic properties. The Evan's Method 1H NMR experiments represent the first empirical study into the magnetism of a half-filled "magic sized" cluster. The magnetic measurements give us important information for how electrons pair within a 1H orbital system. The -1 oxidation state with 12 total electrons in the 1H orbital seems to be a diamagnetic system with all paired electrons whereas the 0, +1, and +2 oxidation states demonstrate paramagnetism increasing with each additional electron removed. This shows a significant difference from previously published material where the +1 oxidation state was seen as diamagnetic by EPR spectroscopy.[12]

Further research needs to go into this system in more oxidation states as well as more trials in each existing oxidation state tested. Currently, two trials have been completed in the 0 and +1 oxidation states and only one trial in the -1 and +2 oxidation states. This is not nearly enough for an accurate analysis without significant error. Investigating the -2 and the +3 oxidation states should also be done. The -2 oxidation state with 13 total electrons within the superatomic 1H orbital could have one ore more unpaired electrons. The +3 oxidation state with 8 total electrons within the superatomic 1H orbital could be diamagnetic or paramagnetic and this would give a strong data set for understanding when the system pairs all electrons like in the -1 oxidation state versus the +1 oxidation state with 2 unpaired electrons.

Once a solid data set is collected on these oxidation states, collaborative work is planned with primarily computational nanocluster chemists. Modeling the 1H orbital system would be a great stride towards understanding this unique system that is not seen within any other materials. Once this system is understood more, possible targeted applications can be thought of for large nanoclusters that are on the cusp of bulk materials.

Chapter 3 References

(1) Nealon, G. L.; Donnio, B.; Greget, R.; Kappler, J.-P.; Terazzi, E.; Gallani, J.-L. Magnetism in Gold Nanoparticles. *Nanoscale* **2012**, *4* (17), 5244–5258.

(2) Singh, R. Unexpected Magnetism in Nanomaterials. *J. Mag. Mag. Mat.* **2013**, *346*, 58–73.

(3) Trudel, S. Unexpected Magnetism in Gold Nanostructures: Making Gold Even More Attractive. *Gold Bull.* **2011**, *44* (1), 3–13.

(4) Tuboltsev, V.; Savin, A.; Pirojenko, A.; Räisänen, J. Magnetism in Nanocrystalline Gold. *ACS Nano* **2013**, *7* (8), 6691–6699.

(5) Herbert, P. J.; Window, P.; Ackerson, C. J.; Knappenberger, K. L. Low Temperature Magnetism in Nanoscale Gold Revealed Through Variable-Temperature Magnetic Circular Dichroism Spectroscopy. *J. Phys. Chem. Lett* **2018**, *10* (2), 189–193.

(6) Krishna, K. S.; Tarakeshwar, P.; Mujica, V.; Kumar, C. S. S. R. Chemically Induced Magnetism in Atomically Precise Gold Clusters. *Small* **2014**, *10* (5), 907–911.

(7) Zhu, M.; Aikens, C. M.; Hendrich, M. P.; Gupta, G.; Qian, H.; Schatz, G. C.; Jin, R. Reversible Switching of Magnetism in Thiolate-Protected Au_{25} Superatoms. *J. Am. Chem. Soc.* **2009**, *131* (7), 2490–2492.

(8) Tofanelli, M. A.; Ackerson, C. J. Superatom Electron Configuration Predicts Thermal Stability of Au25(SR)18 Nanoclusters. *J. Am. Chem. Soc.* **2012**, *134* (41), 16937–16940.

(9) Tofanelli, M. A.; Salorinne, K.; Ni, T. W.; Malola, S.; Newell, B.; Phillips, B.; Häkkinen, H.; Ackerson, C. J. Jahn–Teller Effects in Au 25(SR) 18. *Chem. Sci.* **2016**, *7* (3), 1882–1890.

(10) Tofanelli, M. A.; Ni, T. W.; Phillips, B. D.; Ackerson, C. J. Crystal Structure of the PdAu24(SR)18(0) Superatom. *Inorg. Chem.* **2016**, *55* (3), 999–1001.

(11) Window, P. S.; Ackerson, C. J. Superatom Paramagnetism in Au102(SR)44^1–/0/1+/2+ Oxidation States. *Inorg. Chem.* **2020**, *59* (6), 3509–3512.

(12) Zeng, C.; Weitz, A.; Withers, G.; Higaki, T.; Zhao, S.; Chen, Y.; Gil, R. R.; Hendrich, M.; Jin, R. Controlling Magnetism of $Au_{133}(TBBT)_{52}$ Nanoclusters at Single Electron Level and Implication for Nonmetal to Metal Transition. *Chem. Sci.* **2019**, *10* (42), 9684–9691.

(13) Evans, D. F. The Determination of the Paramagnetic Susceptibility of Substances in Solution by Nuclear Magnetic Resonance. *J. Chem. Soc.* **1959**.

(14) Nimmala, P. R.; Theivendran, S.; Barcaro, G.; Sementa, L.; Kumara, C.; Jupally, V. R.; Apra, E.; Stener, M.; Fortunelli, A.; Dass, A. Transformation of Au144(SCH2CH2Ph)60 to Au133(SPh-TBu)52 Nanomolecules: Theoretical and Experimental Study. *J. Phys. Chem. Lett* **2015**, *6* (11), 2134–2139.

(15) Brust, M.; Fink, J.; Bethell, D.; Schiffrin, D. J.; Kiely, C. Synthesis and Reactions of Functionalised Gold Nanoparticles. *J. Chem. Soc.* **1995**, No. 16, 1655–1656.

(16) Piguet, C. Paramagnetic Susceptibility by NMR: The “Solvent Correction” Removed for Large Paramagnetic Molecules. *J. Chem. Ed.* **1997**, *74* (7), 815.

(17) Buffat, Ph.; Borel, J.-P. Size Effect on the Melting Temperature of Gold Particles. *Phys. Rev. A* **1975**, *13* (6), 2287–2298.

(18) Font, F.; Myers, T. G. Spherically Symmetric Nanoparticle Melting with a Variable Phase Change Temperature. *J. Nano. Res.* **2013**, *15* (12).

Chapter 4. Analysis of Supercluster Formation from $Au_{25}(SC_6H_{13})_{18}$ ‡

4.1 Synopsis

Supramolecular assemblies are of great interest for advanced materials formed both from molecular materials and nanomaterials. Nanoclusters, being a gateway between molecular and bulk materials, present an interesting alternative to study assembly growth and properties. Herein, we present the first analysis of supercluster formation from $Au_{25}(S(CH_2)_5CH_3)_{18}{}^0$ in a two-phase system through dynamic light scattering and electron microscopy studies. Control over the kinetic and thermodynamic growth models of superclusters is displayed through temperature and time scale control in sizes ~25 - 600 nm.

4.2 Introduction

Assemblies of nanoparticles and nanoclusters have attracted research interest for unexpected and interesting properties[1,2,3,] which depend heavily on the building blocks used. As assemblies are created, the properties of these building blocks can change significantly and lead to new materials beyond the traditional nanomaterials.

Supramolecular assembly growth can be provoked through several different methods including crystallization, ligand-reactions like protein or polymer linking[4], solvation[5], electro-assembly[6], and other methods[7]. These methods can result in quasi-stable assemblies or covalently linked assemblies that are stable against perturbation. Previously, Sorensen showed that assemblies could be made with nanoparticles or colloids to create so-called clusters-of-

---

‡ *The work presented herein is soon to be submitted work to the Journal of Chemical Physics and has contributions from Phillip S. Window that include experimental design, data analysis, synthesis, and characterization. Electron Microscopy seen in the main body text was performed by Kanda Borgognoni.*

clusters or superclusters[8]. In this study similar assemblies are formed but from different monomer units in solution, $Au_{25}(SR)_{18}$ nanoclusters.

The ligand-ligand and ligand-nanoparticle interactions that govern supramolecular assemblies can usually be described by Lennard-Jones type interactions; however, with smaller nanoclusters, surface curvature increases relative to ligand length, modeling of these interactions becomes difficult.[9,10] The most effective interpretations of these seems to be based on Van-der-Waals interactions and solvent mediated interactions,[11] but superatoms and gold-gold interactions change these significantly as the size of the particle continues to decrease. In the more traditional sense, supercluster growth can be described by supracrystal growth through classic nucleation theory[12] and through two-phase thermodynamic growth models.

When very short time scales are used, a kinetic growth system dominates supracrystal growth. In this case, the deeper the temperature quench that is used on the sample, the smaller the superclusters that are formed in solution. Nucleation sites develop in solution when the temperature changes enough to form a two phase system. More nucleation sites develop the deeper the temperature quench since the solubility of the monomer unit is lower. A critical nucleus size must be reached in supracrystals before a second growth phase can occur. Since a very short time scale is used, a growth phase has not yet started in earnest at these nucleation sites and they remain small superclusters for a time. The shallower the quench, the fewer nucleation sites develop and so take a shorter time to reach their critical nucleus size before growth, therefore larger superclusters are seen.

When a longer time scale is used, a thermodynamic growth system dominates supracrystal growth. After the critical nucleation size is reached, a two phase system exists in solution in which homogenous growth continues based on the solubility of the monomer unit; the nanocluster. Supercluster size is related to the temperature at which the solution is held. The lower the temperature used, the larger the supercluster observed in the solution since lower temperatures result in reduced solubility.

Using different time scales, temperature, solvents, and concentrations result in different results for the superclusters grown in solution from the $Au_{25}(SR)_{18}$ nanoclusters. Supercluster assemblies from nanocluster building blocks have been investigated within through temperature, solvent, concentration, and oxidation-state control. Herein, we study the synthesis of supercluster assemblies of the well-studied $Au_{25}(SR)_{18}$ cluster into controlled superclusters. The 1-hexanethiol ligand (HSC_6H_{13}) was used to create a relatively unstable ligand shell and this was placed in anti-solvent-rich solvent systems. Through dynamic light scattering (DLS) analysis after controlled temperature changes, both kinetic and thermodynamic regimes could be accessed with superclusters ranging from ~ 30 nm to 600 nm in solvodynamic radius.

4.3 Methods

Synthesis of $Au_{25}(S(CH_2)_5CH_3)_{18}^0$. A one-phase Brust-Schiffrin synthesis was used to synthesize $Au_{25}(S(CH_2)_5CH_3)_{18}^{-1}$.[13] In a usual synthesis chloroauric acid (HAuCl4·3H2O) was dissolved in tetrahydrofuran (THF) solvent with excess tetra(N-octyl) ammonium bromide (TOABr). To this, hexanethiol was added to form a colorless solution. This was then reduced with sodium borohydride, $NaBH_4$, and stirred for >48 hours to form $Au_{25}(S(CH_2)_5CH_3)_{18}^{-1}$.These clusters were then purified through size exclusion chromatography. For supercluster sample testing, the -1 charge state of $Au_{25}(S(CH_2)_5CH_3)_{18}$ was reduced by running through a silica gel column in dichloromethane (DCM) to obtain the 0 charge-state oxidized form of

$Au_{25}(S(CH_2)_5CH_3)_{18}^0$. The purity of the nanocluster was checked through matrix assisted laser desorption ionization time of flight mass spectrometry (MALDI-MS) as seen in Figure 4.1 with a m/z peak around 7 kDa.

All sample solutions for supercluster formation were solvent mixtures of ACS-grade Toluene and Ethanol that were spun at 14k RPM to remove dust particles. The samples were then dissolved in this mixture and centrifuged again. For kinetic and thermodynamic supercluster formation testing, 80% Ethanol/20% Toluene solvent mixture was used. Other testing was performed with solvent mixtures as noted.

DLS Measurements. All DLS measurements were performed on a Malvern Zetasizer Nano ZS with a quartz fluorimeter cell. Purity of the samples was checked by MALDI-TOF MS before and after all measurements.

For accessing kinetic supercluster formation regimes, an external water bath was used, held usually at 40-50 °C. The sample solution was heated thoroughly, quickly removed and wiped clean, then placed in the cooled DLS chamber for quenching. The sample was equilibrated for

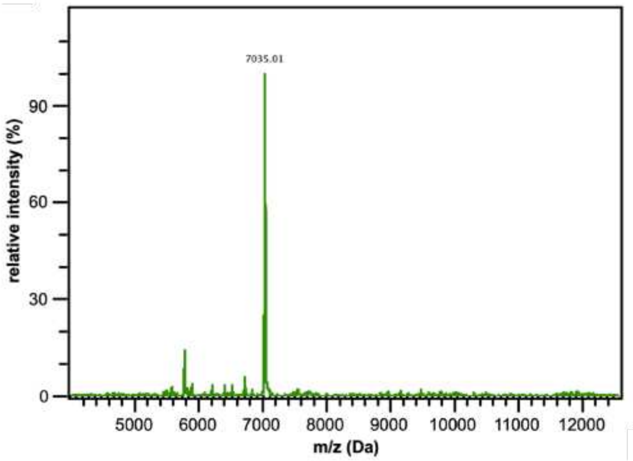

Figure 4.1. MALDI-TOF MS showing purity of $Au_{25}(S(CH_2)_5CH_3)_{18}^0$ with parent peak at 7035 Da and all other peaks assignable as fragments.

short amounts of time, 2-30 s, then measurements were taken with the high-resolution setting on the instrument. Data was analysed through size by volume interpretation. The sample was then recycled back in the water bath and tested at high temperature in the DLS for monomer-only size.

For accessing thermodynamic supercluster formation regimes, the temperature control of the DLS instrument alone was used. The sample solution was heated throroughly to 40-50 °C then checked for monomer only size signal. The samples were then cooled to the quench temperature and equilibrated for 5 minutes before DLS measurement were taken with the high-resolution setting on the instrument. Data was analysed through size by volume interpretation. The sample was then recycled to high temperature in the DLS for monomer-only size check.

4.4 Results and Discussion

Kinetic supercluster formation. Superclusters were formed from purified $Au_{25}(S(CH_2)_5CH_3)_{18}^0$ using multiple methods depending on the growth regime desired, wherein time scale and the depth of the temperature quench were controlled carefully. A kinetic trend following classic nucleation theory could be accessed through small time-scale temperature quenching. The sample solution was heated to 40 °C then quenched to low temperature rapidly. After data collection, the sample would be heated back up and checked for monomeric unit formation before quenching again at a different temperature. Purity of the samples was checked by MALDI-TOF MS before and after all measurements.

Figure 4.2a shows the results of formation of superclusters with a kinetic growth regime. With a time-scale between quenching and data acquisition of about 1.5 minutes, this short-time-scale data reflects the initial nucleation and quick growth of superclusters within the solution.

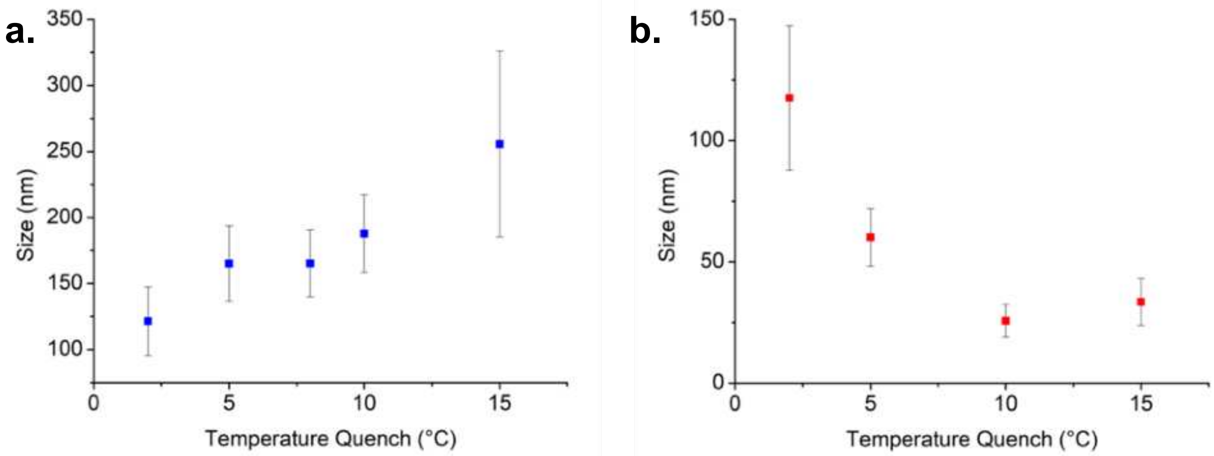

Figure 4.2. Graphs showing supercluster sizes as found by DLS. a. Kinetic growth regime graph of supercluster size from DLS. b. Thermodynamic growth regime of supercluster size from DLS experiments showing larger superclusters formed at lower temperatures, different from the kinetic growth regime.

The lower the quench temperature that was used, the smaller the superclusters formed. A cluster around 200 nm in solvodynamic radius equates to around 2.7x10^6 number of nanoclusters per supercluster. This is calculated with max efficiency packing of spheres, based on $Au_{25}(S(CH_2)_5CH_3)_{18}{}^0$ monomer size found by DLS measurements.

Concentration, as measured by absorbance, was important for accessing this kinetic trend if the sample was too concentrated only a thermodynamic trend could be accessed and if too dilute then supercluster formation is unpredictable. Reproducible and reliable supercluster formation through kinetic growth trends were best seen with an absorbance from 0.2-0.4 at 450 nm which is a known feature of the optical spectrum of $Au_{25}(S(CH_2)_5CH_3)_{18}{}^0$.

Thermodynamic supercluster formation. A thermodynamic trend for supercluster formation could be accessed through temperature control over a more extended time scale. Through longer equilibration times, the thermodynamically favorable size of the superclusters was observed through DLS measurements. These supercluster sizes seen can be attributed to the solubility of the monomer, $Au_{25}(S(CH_2)_5CH_3)_{18}^0$. Figure 4.2b shows the thermodynamic trends seen in the DLS data. At lower temperatures, larger superclusters are seen which is a result of lowered solubility of the monomeric $Au_{25}(S(CH_2)_5CH_3)_{18}^0$ units. Over time the superclusters reach an ideal size which is stable at a certain temperature for a certain concentration of nanoclusters in solution.

The thermodynamic data shows that over time the superclusters reach an ideal size for the conditions used. This indicates there is an exchange between the superclusters of the monomeric nanocluster unit. This changes over time from an initial nucleation size to a thermodynamically favorable supercluster size can be seen in Figure 4.3. In this experiment, an initial short time-scale measurement was made after a fast temperature quench then a longer time-scale measurement was made after equilibration of 5 minutes. At lower temperatures, a smaller supercluster initially formed indicating kinetic nucleation. Then over time at the quench temperature, superclusters grew to their thermodynamically favorable size. This behavior shows

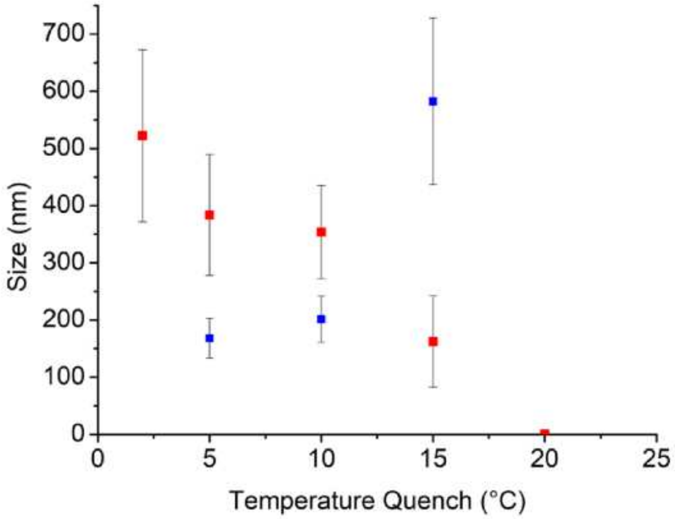

Figure 4.3. Graph showing DLS size trend of experiment containing both kinetic and thermodynamic growth of superclusters.

that in this two-phase system, the monomeric nanocluster unit acts like a molecular or atomic monomeric unit.

Concentration and solvent control of supercluster formation. The effects of concentration of the $Au_{25}(S(CH_2)_5CH_3)_{18}{}^0$ nanocluster in the solvent mixture was tested by DLS measurements to see what trend would arise from differing monomer amounts. For these experiments, optical density (OD) measurements were used at 450 nm from a UV-Vis measurement since measuring concentration from mass would be difficult from the extremely low concentrations used. A 10 °C temperature was picked and the samples equilibrated in the thermodynamic time-scale range before measurements were taken. Figure 4.4 shows the data collected at 2 °C from an optical density range of 0.16 - 1.05 AU. A clear trend can be seen with concentration and supercluster size. As the concentration of the monomeric nanocluster units increases, the size of the quasi-stable supercluster at that temperature increases as well. However, results at the highest OD are also erratic since the high concentration resulted in numerous supercluster sizes ranging from 6 -

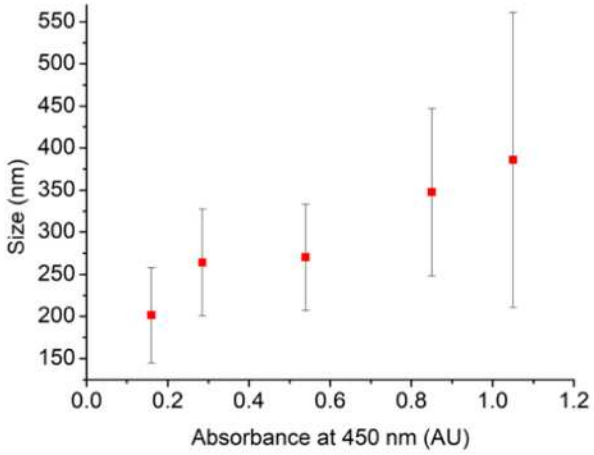

Figure 4.4. DLS data graph showing trend of supercluster size with change in concentration measured by absorbance at 450 nm.

645 nm. It seems there is an optimal range of concentrations where reliable sizes of superclusters can be formed and recycled from monomeric units to assemblies.

Predictable supercluster sizes were seen when changing solvent mixture percentages as well, which can be seen in Figure 4.5. As the ethanol percentage increases the size of a stable supercluster at a consistent temperature increases. This reflects the lowering solubility as the antisolvent is increased. Outside the range of 75-85% ethanol though, results were less clear. Below 75% ethanol, there is not enough anti-solvent in the solution to reliably form superclusters. At above 85% ethanol, the superclusters are irreversibly formed and do not significantly change size over varying temperature ranges. At this solvent ratio, the antisolvent percentage is too high to allow the monomeric units to exchange.

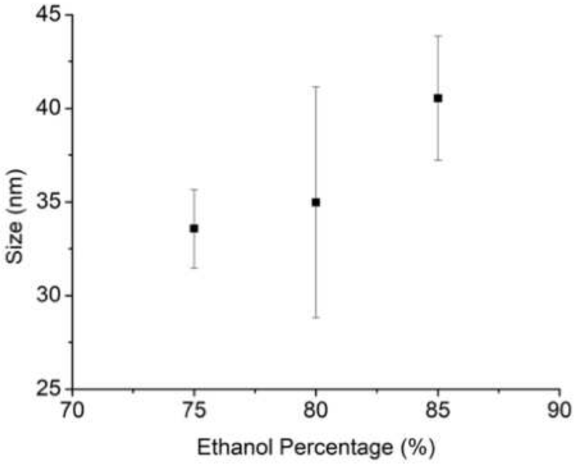

Figure 4.5. Graph showing DLS size data of superclusters with different antisolvent percentages.

Electron microscopy analysis of supercluster assemblies. To support DLS measurements and verify the creation of superclusters in solution electron microscopy studies were performed on a supercluster sample. Ethanol percentage was increased to 85% for this experiment to ensure supercluster formation. A solution with optical density of 0.215 AU was used. The sample was drop-cast at 4 °C with very small volumes (2μL) for transmission electron microscopy (TEM). Figure 4.6a shows a two spherical assemblies of nanoclusters with a diameter of ~300 nm. Figure 4.6b. shows the full field of the TEM grid. In this image, superclusters can be seen with relative monodispersity all around 400 nm in size. Comparing this to the DLS measurements of the solvodynamic radius we can see very close similarities between thermodynamically grown superclusters in Figure 4.2b. Measured around 2 -5 °C, the superclusters range from 370 - 520 nm in DLS measurement compared to the micrographs at ~ 400 nm. Additional micrographs from different grid loading can been seen in Figures S3 and S4.

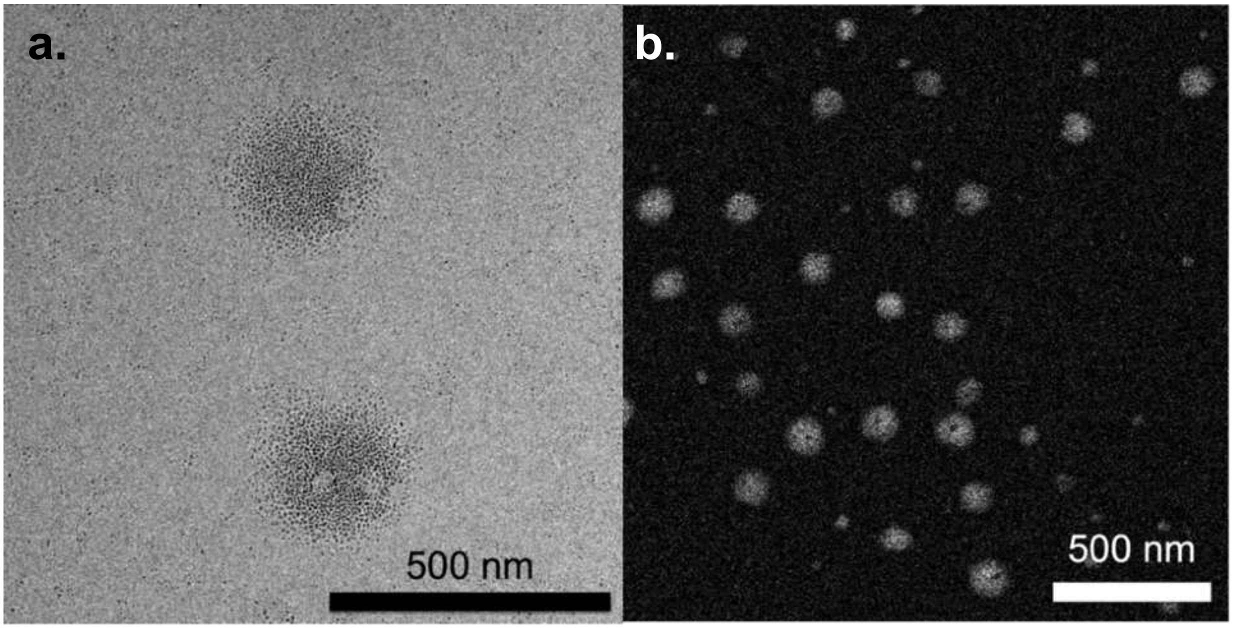

Figure 4.6. Transmission Electron Micrographs of drop-cast supercluster solution. a. Two supercluster assemblies showing spherical shape with particle size around 300 nm. b. Full field with mono-dispersed supercluster assemblies around 200-250 nm in size.

Oxidation state and ligand dependence. Supercluster formation was investigated with different oxidation states of the $Au_{25}(S(CH_2)_5CH_3)_{18}$ nanocluster as well as the $Au_{25}(PET)_{18}^{0/-1}$ nanoclusters (PET = phenylethanethiol). In the case of oxidation state differences of

$Au_{25}(S(CH_2)_5CH_3)_{18}$, supercluster formation was only observed in the 0 oxidation state. The -1 oxidation state of the superatom resulted in no supercluster formation. When the protecting ligand was changed to PET, no supercluster formation was observed in either the 0 or -1 oxidation states.

We believe that the ability to form these superclusters results from the small size, 0 oxidation state of the $Au_{25}(SR)_{18}^0$ nanocluster and the ligand chosen. With the small nanocluster size and relatively low ligand coverage of the surface, there are significant areas of solvent accessible gold atoms seen previously in crystal structure analyses.[14] These gold atoms can interact in solution and might help the assemblies associate and remain stable once the solvent conditions allow for a two-phase system. Evidence for this interaction of surface gold atoms is found with the inability to form superclusters with the $[Au_{25}(S(CH_2)_5CH_3)_{18}]^{-1}[TOA]^{+1}$ solution in similar solvent systems. No superclusters were observed at any available temperature from 2 - 50 °C in DLS measurements. Both the electrostatic repulsion of the “-1” superatom cores and the steric hindrance of the TOA^+ could keep the aurophilic interactions of surface gold atoms and ligand intercalations from associating these nanoclusters into quasi-stable assemblies. Crystal structure analysis shows how much area the TOA^+ ion covers between associated nanoclusters in solid crystalline form.[15]

Further analysis of the supercluster system was attempted with variable temperature UV-Vis and NMR. Figure S1 shows the optical spectra of the nanocluster at varying temperatures with no significant changes other than those that temperature induce. Analysis of the ligand system was attempted through NMR investigations both ^1H NMR and through-space interactions. However, the concentrations at which the supercluster reliably formed (Abs of 0.1-0.5 at 450 nm) were too low for NMR analysis to see signal of the nanocluster ligands.

Comparison to other superatomic supramolecular materials. Clusters have long been considered possible building blocks for new classes of materials. [1],[16],[17] Superatomic clusters can act similarly to elements that already exist and within supramolecular materials could be substituted with significantly different structural impacts. Strong interactions and covalent attachments between clusters can lead to property changes as well such as optical and electronic differences.[18,19]

Recent studies in the nanocluster field have shown that in strong interaction supramolecular assemblies, significant changes can occur to the clusters properties and structure such as nanocluster fusion. In one study, this fusion involved the heating of $Au_{25}(SC_nH_m)_{18}^0$, where n=3-4 and m=7-9 until fusion of the Au_{13} cores led to the formation of $Au_{38}(SR)_{24}$.[20] With a similar ligand used in this study, $Au_{38}(SR)_{24}$ formation did occur but only after 7+ days sitting in solution. Other previous studies involving superatom nanoclusters have shown covalent attachments or other fusion cases unlike the materials studied here.

The evidence showing that these materials can be recycled repeatedly in solution without fusion or other permanent attachments between nanoclusters reveals that the difference between these superclusters and other supramolecular nanocluster materials. Figure S1 shows variable temperature UV-Vis of the material with no significant differences in the spectra.

4.5 Conclusion

The formation of superclusters from nanocluster solutions is a novel method for creating nanomaterial assemblies with precision and possible tailored properties. The DLS analysis of supercluster solution from $Au_{25}(S(CH_2)_5CH_3)_{18}^0$ shows the formation of superclusters in the range of 30-600 nm assemblies in solvodynamic radius. Temperature and time-scale control of the nanocluster solution results in the separation of the kinetic and thermodynamic formation and growth regimes of supercluster assemblies. These regimes and the size of the assemblies seem to be dependent on the concentration of the nanocluster solution and solvent system differences but control over these extra variables requires more investigation. Further evidence suggests that the ability to form supercluster assemblies depends on the small size, oxidation state, and the ligand chosen for the nanocluster solution.

Further investigation could be performed with different antisolvent/solvent mixtures to access more controllable sizes of superclusters formed. In the case of this report, ethanol/toluene was chosen for the temperature window available in a sealed cuvette.

Studies could be extended with larger nanoclusters as the monomer solutions with alkanethiol ligands to look at the effect of the size and curvature of the nanocluster surface. Even larger nanoclusters like $Au_{102}(SR)_{44}$ have surface accessible gold atoms shown in crystal structures previously.[21,14] While this $Au_{102}(SR)_{44}$ nanocluster has not been seen to support alkanethiol ligands, the larger $Au_{144}(SR)_{60}$ nanocluster is commonly synthesized with alkanethiol ligands such as dodecanethiol. Investigating supercluster formation with $Au_{102}(SR)_{44}$ allows for more investigation on the effect of size of the monomer unit, ligand length, and charge state. The larger nanocluster could support different charge states without reducing supercluster associations.

Chapter 4 References

(1) Claridge, S. A.; Castleman, A. W.; Khanna, S. N.; Murray, C. B.; Sen, A.; Weiss, P. S. Cluster-Assembled Materials. *ACS Nano* **2009**, *3* (2), 244–255.

(2) Agrachev, M.; Antonello, S.; Dainese, T.; Ruzzi, M.; Zoleo, A.; Apr, E.; Govind, N.; Fortunelli, A.; Sementa, L.; Maran, F. Magnetic Ordering in Gold Nanoclusters. *ACS Omega* **2017**, *2* (6), 2607–2617.

(3) Singh, R. Unexpected Magnetism in Nanomaterials. *J. Mag. Mag. Mat.* **2013**, *346*, 58–73.

(4) Shenhar, R.; Norsten, T. B.; Rotello, V. M. Polymer-Mediated Nanoparticle Assembly: Structural Control and Applications. *Adv. Mat.* **2005**, *17* (6), 657–669.

(5) Yuan, P.; Zhang, R.; Selenius, E.; Ruan, P.; Yao, Y.; Zhou, Y.; Malola, S.; Häkkinen, H.; Teo, B. K.; Cao, Y.; Zheng, N. Solvent-Mediated Assembly of Atom-Precise Gold–Silver Nanoclusters to Semiconducting One-Dimensional Materials. *Nat. Comm.* **2020**, *11* (1).

(6) Antonello, S.; Dainese, T.; Pan, F.; Rissanen, K.; Maran, F. Electrocrystallization of Monolayer-Protected Gold Clusters: Opening the Door to Quality, Quantity, and New Structures. *J. Am. Chem. Soc.* **2017**,

(7) Klajn, R.; Bishop, K. J. M.; Grzybowski, B. A. Light-Controlled Self-Assembly of Reversible and Irreversible Nanoparticle Suprastructures. *Proc. Natl. Acad. Sci.* **2007**, *104* (25), 10305–10309.

(8) Yan, H.; Cingarapu, S.; Klabunde, K. J.; Chakrabarti, A.; Sorensen, C. M. Nucleation of Gold Nanoparticle Superclusters from Solution. *Phys. Rev. Lett.* **2009**, *102* (9), 095501.

(9) Khan, S. J.; Pierce, F.; Sorensen, C. M.; Chakrabarti, A. Self-Assembly of Ligated Gold Nanoparticles: Phenomenological Modeling and Computer Simulations †. *Langmuir* **2009**, *25* (24), 13861–13868.

(10) Patel, N.; Egorov, S. A. Interactions between Nanocolloidal Particles in Polymer Solutions: Effect of Attractive Interactions. *J. Chem. Phys.* **2005**, *123* (14), 144916.

(11) Goubet, N.; Richardi, J.; Albouy, P.-A.; Pileni, M.-P. Which Forces Control Supracrystal Nucleation in Organic Media? *Adv. Funct. Mat.* **2011**, *21* (14), 2693–2704.

(12) McClurg, R. B. *Homogeneous Nucleation Theory*; Elsevier, 1974.

(13) Brust, M.; Fink, J.; Bethell, D.; Schiffrin, D. J.; Kiely, C. Synthesis and Reactions of Functionalised Gold Nanoparticles. *J. Chem. Soc.* **1995**, No. 16, 1655–1656.

(14) Ni, T. W.; Tofanelli, M. A.; Phillips, B. D.; Ackerson, C. J. Structural Basis for Ligand Exchange on $Au_{25}(SR)_{18}$. *Inorg. Chem.* **2014**, *53* (13), 6500–6502.

(15) Heaven, M. W.; Dass, A.; White, P. S.; Holt, K. M.; Murray, R. W. Crystal Structure of the Gold Nanoparticle $[N(C_8H_{17})_4][Au_{25}(SCH_2CH_2Ph)_{18}]$. *J. Am. Chem. Soc.* **2008**, *130* (12), 3754–3755.

(16) Castleman Jr, A. W.; Khanna, S. N. Clusters, Superatoms, and Building Blocks of New Materials. *J. Phys. Chem. C* **2009**, *113* (7), 2664–2675.

(17) A W Castleman, J. From Elements to Clusters: The Periodic Table Revisited. *J. Phys. Chem. Lett* **2011**, *2* (9), 1–55.

(18) Compel, W. S.; Wong, O. A.; Chen, X.; Yi, C.; Geiss, R.; Häkkinen, H.; Knappenberger, K. L.; Ackerson, C. J. Dynamic Diglyme-Mediated Self-Assembly of Gold Nanoclusters. *ACS Nano* **2015**, *9* (12), 11690–11698.
(19) Champsaur, A. M.; Velian, A.; Paley, D. W.; Choi, B.; Roy, X.; Steigerwald, M. L.; Nuckolls, C. Building Diatomic and Triatomic Superatom Molecules. *Nano Lett.* **2016**, *16* (8), 5273–5277.
(20) Dainese, T.; Antonello, S.; Bogialli, S.; Fei, W.; Venzo, A.; Maran, F. Gold Fusion: From $Au_{25}(SR)_{18}$ to $Au_{38}(SR)_{24}$, the Most Unexpected Transformation of a Very Stable Nanocluster. *ACS Nano* **2018**, *12* (7), 7057–7066.
(21) Heinecke, C. L.; Ni, T. W.; Malola, S.; Mäkinen, V.; Wong, O. A.; Häkkinen, H.; Ackerson, C. J. Structural and Theoretical Basis for Ligand Exchange on Thiolate Monolayer Protected Gold Nanoclusters. *J. Am. Chem. Soc.* **2012**, *134* (32), 13316–13322.

Chapter 5: Ligand Exchange Studies on $Au_{133}(tBBT)_{52}$ with 4BBT.[§]

5.1 Synopsis

Controlling the surface structure of gold nanoclusters is an important step for functionalization of the nanoclusters. The ligand layer is how these materials interact with the "outside world" and how they can be attached to surfaces or materials of interest. Extensive research has been performed on small nanoclusters with a variety of ligands exchanged and techniques used; however, larger gold nanoclusters tend to be more difficult to work with. Within, crystallographic studies are being performed on $Au_{133}(tBBT)_{52}$ (tBBT=tert-butylbenzenethiol) with varying ligand equivalents added for exchange. Crystals were grown after exchange with para-bromobenzenethiol (4BBT) ligands and diffracted. Diffraction patterns are currently being solved for crystal structure analysis.

5.2 Introduction

Gold nanomaterials are of great interest for numerous applications because of their unique, tunable properties.[1–3] Ligand exchange on gold nanomaterials is crucial for preparing them for most applications or stabilizing them for increased lifetime.[4–7] Studies into surface modifications have been widespread on the smaller nanoclusters such as $Au_{25}(SR)_{18}$[8–10] and water soluble materials like $Au_{102}(p\text{-}MBA)_{44}$.[11] However, studies on larger organosoluble nanoclusters above the ~100 gold nuclearity can result in cluster core rearrangement to different nanoclusters. (144-133, 133-99, etc)[12,13]

[§] *The work presented herein includes contributions from Phillip S. Window that include experimental design, synthesis, and characterization. Diffraction of single crystals was performed by Ian Anderson.*

As nanoclusters increase in size and their properties closer to bulk materials, the surfaces become flatter and ligand packing on the surface gets denser. Cone angle changes, (i.e. sterics) in protecting ligands have a bigger impact on the surface chemistry which can then significantly change the cluster core arrangement. Bulky or stiff ligands also have different effects on the arrangement of those ligands on the surface environment and small changes to these ligands can have drastic effects on the core geometry and stabilization. This is clear in the case of core-size conversion from $Au_{144}(SR)_{60}$ to $Au_{133}(SR)_{52}$ versus $Au_{144}(SR)_{60}$ to $Au_{99}(SR)_{42}$. For the conversion to $Au_{133}(SR)_{52}$ 4-tert-butylbenzenethiol (tBBT) is used and for the conversion to $Au_{99}(SR)_{42}$, thiophenol (SPh) is used.[13] The difference of the tert-butyl group results in a different core-size conversion and different geometric stabilization even though the cone angle of these ligands is very similar.

Additionally, as nanoclusters increase in size, the core arrangements are built from increasingly large geometric shells and seem to become more and more symmetrical.[14] This can result in polymorphism in the core, gold atom arrangements. In the case of $Au_{144}(SR)_{60}$, crystallization and X-ray crystallography are extremely difficult due to fractionation and polymorphism.[15–17] However, $Au_{133}(SR)_{52}$ has significantly less symmetry in the shell structure of its core which allows for easier crystallographic studies.

$Au_{133}(SR)_{52}$ has a 55 gold atom core with a 1 + 12 + 42 rhombicosododecahedron structure as seen in Figure 5.1. A 52 atom shell is then added to this, breaking the Ih symmetry down to D. The lack of symmetry in the core results in $Au_{133}(SR)_{52}$ being one of the few cases of spherical, chiral, gold nanoclusters without chiral protecting ligands. The ease of crystallographic

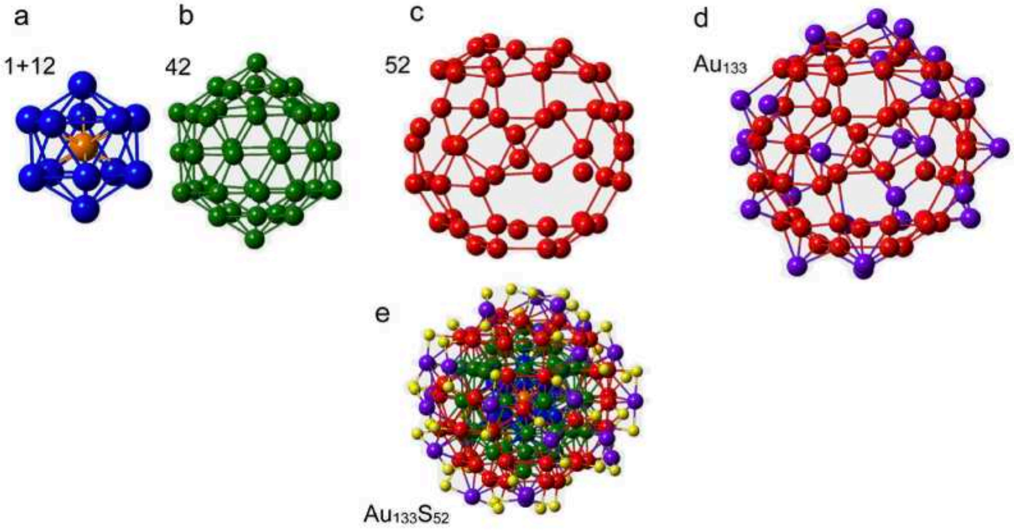

Figure 5.1. Structure of $Au_{133}(SR)_{52}$ shown from core to staple units. a. 12 atom icosahedral core surrounding center gold atom. b. icosahedral shell around core. c. 52 atom shell from rhombiicosidodecahedron missing 8 atoms. d. rhombiicosidodecahedron shell with gold atoms added from stable units. e. full structure of $Au_{133}(SR)_{52}$ with carbons omitted for clarity. *image copied and edited from publication.[20]

studies with spherical $Au_{133}(SR)_{52}$ means this material is ideal for analyzing ligand exchange on a larger nanocluster and comparing this to smaller nanoclusters.

X-ray Crystallography is an extremely powerful tool for the investigation of many types of materials.[18] In the case of gold nanocluster, it is essential for the examination of how these nanoclusters interact in solution and to predict how they will interact with other materials. X-ray crystallography resulted in immense progress to the field with the first gold nanocluster structure solved.[19] Since then, it is still a crucial analytical technique for understanding nanoclusters with their original ligands and those with exchanged ligands and their interactions with each other in the solid state.

Numerous studies have been performed on multiple gold nanoclusters smaller than 102 gold atoms, with varying amounts of incoming ligand to fully exchanged nanoclusters. The larger incoming ligand equivalent studies have been performed on small gold nanoclusters with thiol-for-thiol and thiol-for-selenol exchange. Large equivalent studies through X-ray crystallography have not been performed successfully to our knowledge on nanoclusters larger than $Au_{25}(SR)_{18}$ without core-size conversion. With more ligands exchanged, large nanocluster surfaces could have different behavior in the placement of mixed ligands on the surface such as different preferred exchange locations on the staple units.

Herein, ligand exchange studies have been performed on $Au_{133}(SR)_{52}$ protected by 4-tertbutylbenzenethiol (tBBT) with incoming ligands being 4-bromobenzenethiol (4-BBT). Single crystals were grown and diffracted at the Advanced Light Source Synchrotron X-Ray Diffractometer at Lawrence Berkley National Laboratory. However, X-ray Crystallography diffraction data has not been worked up on these diffraction pattern data-sets as of yet. Here is discussed the process for purification, crystallization, and controlled ligand exchange studies on a large gold nanocluster.

5.3 Methods

Previously discussed in Chapter 3 is the process for synthesis, purification, and crystallization of $Au_{133}(tBBT)_{52}$. Here the process will be repeated in short. Full details are in Appendix II.

In this work, the mono-ligated $Au_{133}(tBBT)_{52}$ was synthesized, purified, and crystallized based on a modified literature technique[12,20] then ligand exchange was performed on the nanocluster with 4-BBT as the incoming ligand. Full synthetic details are in the SI for Chapter 3. In short, $Au_{144}(PET)_{60}$ was first synthesized using a one-phase Brust-Schiffrin synthesis. The published time scale for the reaction was extended for better yield of $Au_{144}(PET)_{60}$ over $Au_{25}(PET)_{18}$ from 5 hours to 48 hours. The crude $Au_{144}(PET)_{60}$ was then purified through size exclusion chromatography (SEC). The $Au_{144}(PET)_{60}$ crude sample was then converted into $Au_{133}(tBBT)_{52}$ through ligand exchange thermo-etching or LEIST (ligand exchange induced size transformation). The $Au_{133}(tBBT)_{52}$ nanocluster was then crystallized from this sample through a dichloromethane/acetonitrile layering. Acetonitrile is carefully layered over dichloromethane in a 1:2 ratio at first and allowed to sit for greater than 48 hours. More acetonitrile was carefully layered until single crystals were formed. Moving forward with only crystallized sample was the best way to ensure the best purity of the sample possible since MALDI-TOF MS with large clusters has a very large envelope around the molar mass of the material that only indicates the rough size of the material.

Ligand Exchange Studies. Ligand exchange studies were performed with 4BBT ligand using multiple techniques. First, low equivalent ligand exchange (2-5 eq) was performed with short time-scale exchanges. The liquid ligand was diluted in toluene to a 0.1 or 1 mg/mL solution and was mixed with the nanocluster dissolved in DCM in the desired equivalents based on the mass of the purified sample. These solutions were stirred for 10 min at room temperature, 19-23 °C. Excess acetonitrile was then added to the solution and then rotovaped until minimal solvent remained in the vial. This ensured that the sample precipitated from solution and could not continue ligand exchange since the DCM mostly evaporates before the acetonitrile. Then excess methanol was added to the solution and centrifugation was used to collect the solid sample and remove excess ligand from the solution since free ligand is solution in alcohols but the nanocluster is not. Crystallization was done with the same technique as described above. Large single crystals required several recrystallizations and so were allowed significant time within solution after the exchange.

Higher equivalent ligand exchange was performed with short time scale as well as long time scale experiments to examine more ligands possibly exchanged onto the surface of the nanocluster. 10 equivalent exchange was attempted as well as 25 equivalent exchange. The 10 equivalent exchange was attempted the sample dissolved in DCM with the correct equivalents of 4BBT added and never washed. Crystallization was set up directly within this sample vial with acetonitrile layered above the DCM and toluene mixture. In this procedure it was set up for crystallization with the free ligands remaining in solution. The 25 equivalent exchange was performed with a 5 minute mixing time then the solution was cleaned of free ligand as described for the 2-5 equivalent exchange. Crystallization was done with the same acetonitrile and DCM layering technique described above.

Crystals were selected for diffraction in a stereoscope and loaded on a micromesh in Paratone-N oil based cryoprotectant. All crystals mounted with these studies had a hexagonal platelet morphology.

5.4 Results and Discussion

Successful crystallization was performed on the unexchanged $Au_{133}(tBBT)_{52}$, $Au_{133}(tBBT)_{52}$ with 2-5 ligands possibly exchanged, $Au_{133}(tBBT)_{52}$ with 10 ligands possibly exchanged, and $Au_{133}(tBBT)_{52}$ with 25 ligands possibly exchanged. The total possible exchanged number of ligands is based on the equivalents of ligand added per ligand on the surface of the nanocluster. Diffraction was then achieved on the unexchanged, 2-5 equivalent, and 25 equivalent exchanged nanocluster samples. Further studies have been performed with higher incoming ligand equivalents and different time-scales of mixing but no high quality crystals have been grown yet.

Previous Ligand Exchange Studies. Previous ligand exchange studies have suggested that the mechanism of ligand exchange for gold nanoclusters is associative. During short time-scale ligand exchange studies, the locations of exchanged ligands on the nanocluster occupy the most solvent accessible surface gold positions in the crystal structure. This result was seen with 2-4 ligands exchanged on $Au_{25}(SR)_{18}$ and 4 ligands exchanged on $Au_{102}(SR)_{44}$.[9,11] However, these studies were based on crystallographic data only. In the case of solid state investigations, contact points between molecules can influence the preferred location of the exchanged ligands.

More recently, studies have been performed on ligand exchange of materials with the introduction of intercluster reactions.[21,22,22] In these case, two nanoclusters within solution can exchange ligands and metal atoms from their surfaces and from their cores readily. A study revealed that silver clusters cannot exchange metal atoms or ligand when separated by dialysis membranes, further suggesting an associative mechanism required for ligand exchange.[23] With these studies, doubt in the results from crystallographic studies has decreased and the results from short time-scale ligand exchange still seem plausible.

Long time-scale ligand exchange studies mixed with intercluster interactions, however, reveal a different result for ligand positions on the surface of gold nanoclusters. When ligands are exchanged onto a nanocluster then long time-scales are used with the nanoclusters in solution for multiple days, further rearrangement of the ligands has been observed. Dr. Chris Hosier from the Ackerson lab observed that when exchanging thiol for selenol ligands on the $Au_{25}(SeR/SR)_{18}$ nanocluster, time has a large influence on the regiochemistry of ligands on the surface. Thiol ligands were exchanged onto a fully selenol protected nanocluster. Crystals were grown after differing times spent within solution. After initial exchange, crystallization was performed as fast as possible and partial exchange was seen across most of the nanocluster. If longer times were used before crystallization different positions emerged as those with higher percentages of partial exchange. This study seems to capture more of a thermodynamic equilibrium of exchanged ligands through crystallographic investigations.

Planned Studies and Outlook. Crystal structures of $Au_{133}(SR)_{52}$ have not yet been solved of the exchanged nanocluster and so there are no crystal structures to compare here. However, hypothesized and expected results can be discussed. From previous results of small time-scale and small ligand equivalent exchange performed with quick crystallization, we can expect only a few ligands to be exchanged on the surface of the nanocluster. $Au_{133}(tBBT)_{52}$ is stabilized by the bulky tert-butyl group on the ligand and the incoming ligand only has a bromine atom in the same position. This change in how stiff and bulky the ligand is could affect the positions these exchanged ligands occupy on the surface. However, if we assume that a small enough number of exchanged ligands will not upset the stability and structure of the nanocluster, we expect the exchanged ligands to occupy the most solvent accessible gold positions in the crystal structure. Crystals form in under 24 hours in most cases for $Au_{133}(tBBT)_{52}$, so intercluster interactions and surface rearrangements are unlikely.

For the higher ligand equivalent exchange, short time scales were used for the exchange reaction and crystals were also formed very quickly without extended time in solution. There is currently no hypothesis for how the ligands will be positioned on the surface of the nanocluster in this study. With 25 incoming ligands, almost half the ligands could be exchanged on the nanocluster, however, with such a short mixing time, this number is likely to be much smaller than 25. Currently, exchanges are still being performed with this number of ligand equivalents and longer mixing times to see the thermodynamically favorable ligand positions.

5.5 Conclusion

Within this study, $Au_{133}(tBBT)_{52}$ was synthesized, purified, crystallized, and ligand exchange experiments were performed with 4-BBT as the incoming ligand. Successful synthesis and crystallization of this material was done through modifying literature synthesis and careful crystallization techniques. Ligand exchange studies have been performed with 4-BBT following previously used methods from the Ackerson lab. Previous results for thiol-for-thiol ligand exchange on gold nanocluster have all been small-equivalent exchange. However, this material appears to support higher equivalent exchange which will provide important information for how large nanocluster surfaces arrange ligands with mixed ligand environments. Further experiments are currently being performed with larger equivalent ligand exchange and longer time-scale reactions. Diffraction pattern data will be solved for crystal structure analysis soon and further data analysis and comparison will be performed.

Chapter 5 References

(1) Daniel, M.-C.; Astruc, D. Gold Nanoparticles: Assembly, Supramolecular Chemistry, Quantum-Size-Related Properties, and Applications toward Biology, Catalysis, and Nanotechnology. *Chem. Rev.* **2004**, *104* (1), 293–346.

(2) Giljohann, D. A.; Seferos, D. S.; Daniel, W. L.; Massich, M. D.; Patel, P. C.; Mirkin, C. A. Gold Nanoparticles for Biology and Medicine. *Angew. Chem.* **2010**, *49* (19), 3280–3294.

(3) Louis, C. Gold Nanoparticles for Physics, Chemistry and Biology. **2012**.

(4) Jung, J.; Kang, S.; Han, Y.-K. Ligand Effects on the Stability of Thiol-Stabilized Gold Nanoclusters: $Au_{25}(SR)_{18}$, $Au_{38}(SR)_{24}$, and $Au_{102}(SR)_{44}$. *Nanoscale* **2012**, *4* (14), 4206–4210.

(5) Sharma, J.; Chaki, N. K.; Mandale, A. B.; Pasricha, R.; Vijayamohanan, K. Controlled Interlinking of Au and Ag Nanoclusters Using 4-Aminothiophenol as Molecular Interconnects. *J. Colloid Interface Sci.* **2004**, *272* (1), 145–152.

(6) Ertem, E.; Murillo-Cremaes, N.; Carney, R. P.; Laromaine, A.; Janeček, E.-R.; Roig, A.; Stellacci, F. A Silica-Based Magnetic Platform Decorated with Mixed Ligand Gold Nanoparticles: A Recyclable Catalyst for Esterification Reactions. *Chem. Comm.* **2016**, *52* (32), 5573–5576.

(7) Abtahi, S. M. H.; Burrows, N. D.; Idesis, F. A.; Murphy, C. J.; Saleh, N. B.; Vikesland, P. J. Sulfate-Mediated End-to-End Assembly of Gold Nanorods. *Langmuir* **2017**, *33* (6), 1486–1495.

(8) Meng, X.; Xu, Q.; Wang, S.; Zhu, M. Ligand-Exchange Synthesis of Selenophenolate-Capped Au25 Nanoclusters. *Nanoscale* **2012**, *4* (14), 4161–4165.

(9) Ni, T. W.; Tofanelli, M. A.; Phillips, B. D.; Ackerson, C. J. Structural Basis for Ligand Exchange on $Au_{25}(SR)_{18}$. *Inorg. Chem.* **2014**, *53* (13), 6500–6502.

(10) Fernando, A.; Aikens, C. M. Ligand Exchange Mechanism on Thiolate Monolayer Protected $Au_{25}(SR)_{18}$ Nanoclusters. *J. Phys. Chem. C* **2015**, *119* (34), 20179–20187.

(11) Heinecke, C. L.; Ni, T. W.; Malola, S.; Mäkinen, V.; Wong, O. A.; Häkkinen, H.; Ackerson, C. J. Structural and Theoretical Basis for Ligand Exchange on Thiolate Monolayer Protected Gold Nanoclusters. *J. Am. Chem. Soc.* **2012**, *134* (32), 13316–13322.

(12) Nimmala, P. R.; Theivendran, S.; Barcaro, G.; Sementa, L.; Kumara, C.; Jupally, V. R.; Apra, E.; Stener, M.; Fortunelli, A.; Dass, A. Transformation of $Au_{144}(SCH_2CH_2Ph)_{60}$ to Au_{133}(SPh-TBu)$_{52}$ Nanomolecules: Theoretical and Experimental Study. *J. Phys. Chem. Lett* **2015**, *6* (11), 2134–2139.

(13) Nimmala, P. R.; Dass, A. $Au_{99}(SPh)_{42}$ Nanomolecules: Aromatic Thiolate Ligand Induced Conversion of $Au_{144}(SCH_2CH_2Ph)_{60}$. *J. Am. Chem. Soc.* **2014**, *136* (49), 17016–17023.

(14) Bergmann, T.; Göhlich, H.; Lange, T.; 1991. Shell Structure of Clusters. *J. Phys. Chem.*

(15) Jensen, K. M. Ø.; Juhas, P.; Tofanelli, M. A.; Heinecke, C. L.; Vaughan, G.; Ackerson, C. J.; Billinge, S. J. L. Polymorphism in Magic-Sized $Au_{144}(SR)_{60}$ Clusters. *Nat Commun* **2016**, *7* (1), 11859.

(16) Lei, Z.; Li, J.-J.; Wan, X.-K.; Zhang, W.-H.; Wang, Q.-M. Isolation and Total Structure Determination of an All-Alkynyl-Protected Gold Nanocluster Au144. *Angew. Chem.* **2018**, *57* (28), 8639–8643.

(17) Lopez-Acevedo, O.; Akola, J.; Whetten, R. L.; Grönbeck, H.; Häkkinen, H. Structure and Bonding in the Ubiquitous Icosahedral Metallic Gold Cluster $Au_{144}(SR)_{60}$. *J. Phys. Chem. C* **2009**, *113* (13), 5035–5038.

(18) Ni, T. W.; Tofanelli, M. A.; Ackerson, C. J. Structure Determination by Single Crystal X-Ray Crystallography. *Front. Nano.* **2015**, 103–125.

(19) Jadzinsky, P. D.; Calero, G.; Ackerson, C. J.; Bushnell, D. A.; Kornberg, R. D. Structure of a Thiol Monolayer-Protected Gold Nanoparticle at 1.1 A Resolution. *Sci.* **2007**, *318* (5849), 430–433.

(20) Dass, A.; Theivendran, S.; Nimmala, P. R.; Kumara, C.; Jupally, V. R.; Fortunelli, A.; Sementa, L.; Barcaro, G.; Zuo, X.; Noll, B. C. $Au_{133}(SPh\text{-}TBu)_{52}$ Nanomolecules: X-Ray Crystallography, Optical, Electrochemical, and Theoretical Analysis. *J. Am. Chem. Soc.* **2015**, *137* (14), 4610–4613.

(21) Hosier, C. A.; Anderson, I. D.; Ackerson, C. J. Acetylide-for-Thiolate and Thiolate-for-Acetylide Exchange on Gold Nanoclusters. *Nanoscale* **2020**, *12* (11), 6239–6242.

(22) Krishnadas, K. R.; Baksi, A.; Ghosh, A.; Natarajan, G.; Som, A.; Pradeep, T. Interparticle Reactions: An Emerging Direction in Nanomaterials Chemistry. *Acc. Chem. Res.* **2017**, *50* (8), 1988–1996.

(23) Zhang, B.; Salassa, G.; Bürgi, T. Silver Migration between $Au_{38}(SC_2H_4Ph)_{24}$ and Doped $Ag_xAu_{38-x}(SC_2H_4Ph)_{24}$ Nanoclusters. *Chem. Commun.* **2016**, *52* (59), 9205–9207.

Chapter 6: Controlled Crystallization of $Au_{25}(SR)_{18}$ Leading to Polymorphic Structures**

6.1 Synopsis

Recent decades of research into gold nanoclusters have yielded conflicting results from the same gold nanoclusters from electrochemical studies to magnetism. Different crystal structures have also been solved for the same materials with no analysis this occurrence. Within this study, four different crystal morphologies were observed after synthesis and crystallization of $Au_{25}(PET)_{18}$. After diffraction of these crystals, four different structures were solved, two of which were previously unpublished. The needle morphology is also the first chiral structure of $Au_{25}(PET)_{18}$ observed without ligand exchange or external modifications. These different solid-state structures could be explanations for different observed properties. Understanding of the different crystallization techniques for access of these crystal morphologies is crucial for explaining different solid state properties in other nanocluster systems.

6.2 Introduction

X-ray crystallography is a powerful tool for studying molecular structures as well as nanocluster structures and the possible impact on the function and properties of a material. There are numerous techniques available to elucidate structure, however, the most powerful and most widely accepted for the solid state structure of a material is single crystal X-ray diffraction.[1] If the properties of a material can be examined through other analytical methods and then compared to the crystallographic structure of a material, trends can be inferred about how those

---

** *The work presented herein includes contributions from Phillip S. Window that include experimental design, synthesis, and characterization. Data analysis was performed by Dr. Chris Hosier, and Diffraction of crystals and crystal structure solving was performed by Rigaku Americas in Denver, CO.*

properties could be changed or affected in other materials. The atomic make-up of a material obviously influences the properties observed. The unique properties of gold nanoclusters, being size dependent, are a great example of this.[2–5] However, small structural changes through structural isomerization can also lead to significant property changes.

Structural isomers can be different in many ways from different organization of atoms with different bonds, to mirror images or very small changes. When a compound does not have different organization of atoms or any different bonds but packs differently in the solid state, these can be called polymorphs. Like isomers, property differences arise from these polymorphs that can be attributed to small changes in the structure of the material. These small changes are in the intramolecular interactions of the materials within the solid state and not within the material itself. Gold nanoclusters are no exception to this occurrence and it has been observed in recent years.[6,7]

Polymorphism in the core arrangement of atoms has been studied with larger nanoclusters and is the reason that in highly symmetric nanoclusters, crystal structures are difficult to solve with a high degree of certainty.[6] In smaller nanoclusters, isomerization and polymorphism is prevalent with ligand layers rather than the core gold arrangements. Multiple structures have been published of $Au_{25}(SR)_{18}$ and other nanoclusters that have different space groups and slightly different ligand arrangements but no significant work has been done to investigate these.[8–10]

Over the years with a range of materials including gold nanoclusters, differing results from optical, electronic, magnetic[11–13], bioavailability[14], e.g. have arisen through published research. These differences in properties from extremely similar materials have not been fully investigated in gold nanoclusters but recently theorized to be from polymorphic structural changes. A direct comparison of the properties and the differing structures of gold nanoclusters could result in a more definite answer as to the origin of different properties in seemingly identical materials.

During work with the $Au_{25}(PET)_{18}$ gold nanocluster for a different project in the Ackerson research group, it was observed that as the purified sample was crystallized, different morphologies of crystal were being collected. First, the most common morphology, or shape, for the material (cuboid) was the most prevalent when crystallizing $Au_{25}(PET)_{18}^{0}$. Then as more material was crystallized through different techniques to collect pure sample, different morphologies were beginning to arise, such as rectangular prisms, longer needles, and platelets with hexagonal shapes. Since these were all from similar crystallization techniques and from the same assumed pure samples, this was an interesting development.

Different macroscopic morphologies can be indicative of crystallographic conformational polymorphism so these crystals were diffracted and their structures solved and compared. The structures are discussed herein with a geometric analysis done previously by Dr. Christopher Hosier of the Ackerson Lab. Five different morphologies of crystals were collected and sent for diffraction and analysis with four different structures being observed. Two of these structures were previously unpublished structures of the $Au_{25}(PET)_{18}^{0}$ nanocluster and two others were previously published but with higher quality. The direct comparison of these structures and their possible property differences could lead to further understanding of the influence of the ligand layer of nanoclusters for later applications.

Within this work is discussed the methods of synthesis, purification, and most importantly the crystallization techniques used to access these different crystallographic morphologies. This chapter includes a much more in-depth explanation of the methods used for the crystallization of these materials than has previously been published. The results of slightly different crystallization techniques are discussed to further apply this to other gold nanocluster crystallizations for intentional property changes. Controlling crystallization through temperature, time, solvent and oxidation state changes led to these different morphologies and is important for solid phase applications of gold nanoclusters.

6.3 Methods

$Au_{25}(PET)_{18}$ was synthesized using a published synthetic procedure from the Ackerson lab.[15] In a typical synthesis 1.00 g (2.54 mmol) of $HAuCl_4$-$3H_2O$ and 1.56 g (2.85 mmol) of tetraoctylammonium bromide (TOAB) was added to 70 ml of THF in a round-bottom flask. This was then stirred for 15 minutes while the solution turns from a gold-salt yellow to an orange red. 1.8 ml (13.4 mmol) of 2-phenylethanethiol (PET) was added quickly and the reaction stirred over time until the color leaves the solution, generally ~3 hours. Once the solution turned clear, 965 mg (25.5 mmol) of $NaBH_4$ and 24 ml of water at 0 C ° was added rapidly to this flask with caution that the solution did not overflow due to the formation of bubbles. The solution was stirred for 48 hours loosely covered at 500 rpm as a black solid.

To clean the crude $Au_{25}(PET)_{18}$ sample, excess methanol was added to the flask to quench the remaining reductant in solution. A rotary evaporator was then used to remove all the solvent possible under vacuum. This leaves an oily black substance in the flask, to which

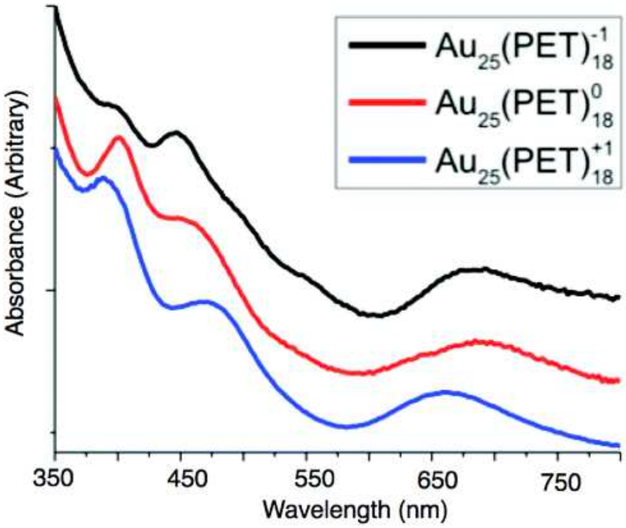

Figure 6.1. Optical spectra of $Au_{25}(PET)_{18}$ in three different oxidation states taken from Tofanelli's publication.[9] Showing clear distinction between oxidation state spectra.

methanol was added. After sonication, this suspension was centrifuged to precipitate the crude sample and wash away excess thiol.

Purification was performed on the nanocluster crude sample through size exclusion chromatography (SEC) with BioBeads SX1 matrix in tetrahydrofuran (THF). The nanocluster in its -1 oxidation state (the most stable form), is a strong reddish brown color and is an easy band to view on the SEC column. Multiple fractions of this reddish band were collected and run again on the SEC column. MALDI-TOF MS and UV-Vis spectroscopy was used to ensure purity of the $Au_{25}(PET)_{18}$ sample. Figure 6.1 shows a comparison of the $Au_{25}(PET)_{18}^{-1/0/+1}$ samples where clear differences are seen between the oxidation states.

Crystallization techniques were varied and discussed below but crystal preparation, sample handling, and diffraction were all done by Rigaku Americas in Denver, Colorado.

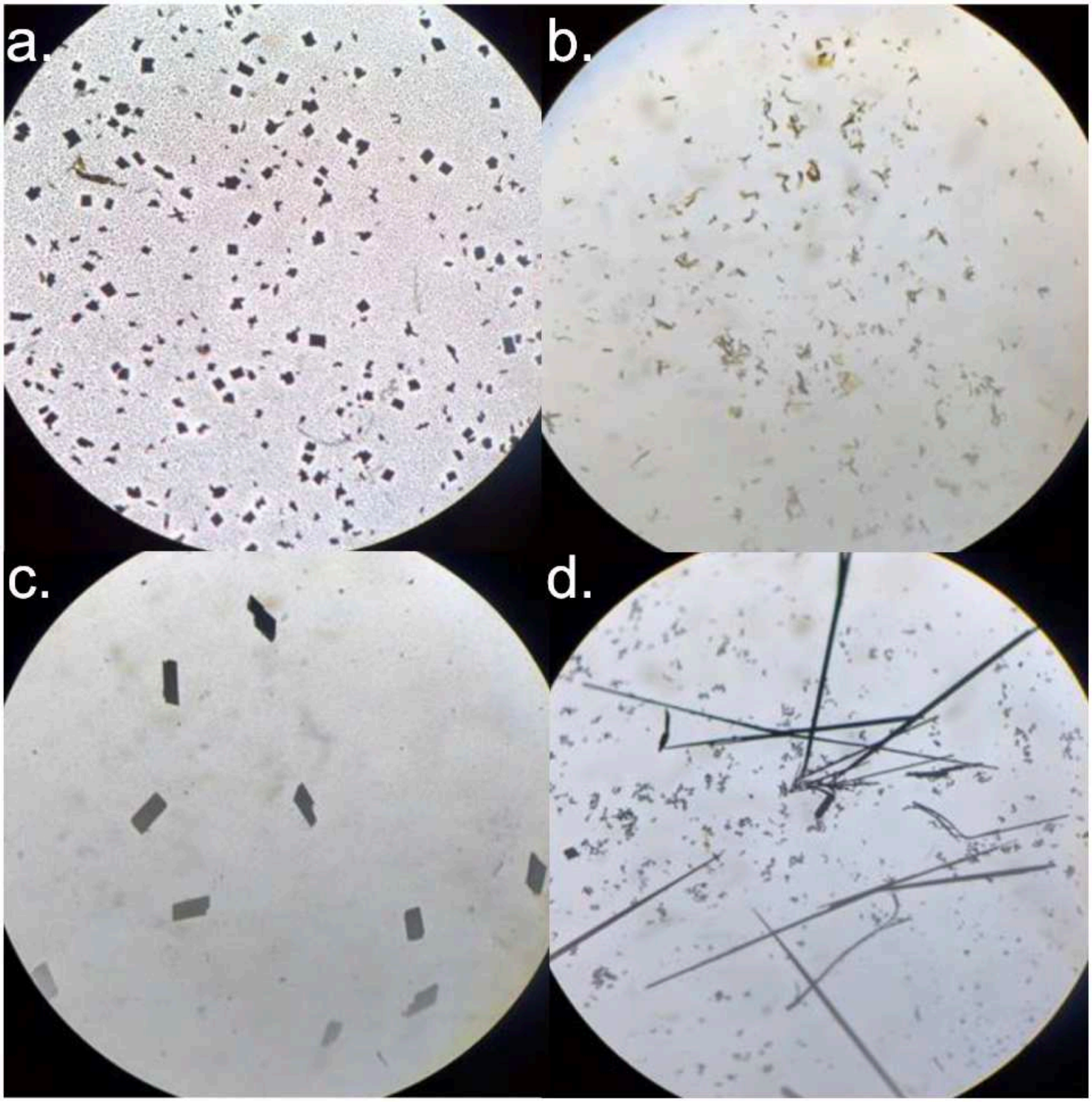

Figure 6.2. Photographs of 4 different crystal morphologies of $Au_{25}(PET)_{18}$ seen through a microscope. **a.** cuboid crystal morphology. **b.** platelet morphology. **c.** quadrilateral prism morphology. **d.** needle morphology.

6.4 Results and Discussion

Crystallizations. Four different crystal morphologies were observed through the crystallization of $Au_{25}(PET)_{18}$ with slightly different techniques and methods leading to the different crystalline shapes. Figure 6.2 shows the images of the four different crystals that resulted in different structures as seen through a microscope.

Figure 6.2a. shows a cuboid shaped cluster from a macroscopic view. This crystal morphology is the easiest to crystallize of the material and comes from the most used method for crystallization of $Au_{25}(PET)_{18}$. Purified sample was dissolved in minimal toluene. Ethanol was then added slowly while mixing until the sample becomes cloudy. This was then centrifuged and the precipitate was tested via UV-Vis spectroscopy in DCM for the $Au_{25}(PET)_{18}$ signature, which is easy to view within the optical spectrum. This was repeated until the $Au_{25}(PET)_{18}$ signature was seen. The supernatant was then carefully placed in a scintillation vial after filtration for dust and placed on a very low warmth hot-plate. As the sample was heated in the toluene and ethanol solution, $Au_{25}(PET)_{18}$ oxidizes from the -1 to the 0 oxidation state. It then crystallizes as the solubility decreases from this oxidation state change. Cuboid crystals are the result from this technique in most cases. The structure solved from this crystal habit has previously been published previously.[8] This crystal structure can be viewed in Figure 6.3a.

Figure 6.2b. shows the macroscopic view of the platelet morphology of the $Au_{25}(PET)_{18}^{0}$ crystals. This crystal morphology was accessed via a different solution composition and an unintentional in-situ oxidation of the nanocluster. The purified sample was collected from cuboid crystals of $Au_{25}(PET)_{18}^{-1}$. This was dissolved in deuterated acetonitrile with a 1:1000 ratio of tetramethylsilane added for 1H NMR investigations. In a very brief amount of time, the -1 oxidation state of the nanocluster oxidized in the acetonitrile to form the 0 oxidation state which is insoluble in acetonitrile. The sample precipitated within an NMR tube and quickly crystallized even while being handled. As seen in Figure 2b, very small, thin platelets that were slightly needle-shaped formed and were collected for diffraction. This technique was repeated and the same morphology of crystals were formed in multiple trials. The crystal structure that resulted from this morphology was a previously unpublished structure of $Au_{25}(PET)_{18}^{0}$. This crystal structure can be viewed in Figure 6.3b.

Figure 6.2c. shows the macroscopic view of the quadrilateral prism morphology of the $Au_{25}(PET)_{18}^{0}$ crystals. This crystal morphology was accessed through a different crystallization technique from the other morphologies. The purified sample was collected from cuboid crystals of $Au_{25}(PET)_{18}^{-1}$. This sample was oxidized by passing it through a silical gel column in DCM which is a known, easy technique for oxidation of the nanocluster. It was then dried and dissolved in minimal toluene. Ethanol was layered carefully on top of this solution and allowed to diffuse in over 2-3 days. Crystals were observed within the solution over several days of formation. The crystal structure that resulted from this morphology was the same as a previously published structure of $Au_{25}(PET)_{18}^{0}$ found within the Ackerson Lab.[9] This crystal structure from quadrilateral prism shaped crystals can be viewed in Figure 6.3c.

Figure 6.2d. shows the macroscopic view of the needle morphology of the $Au_{25}(PET)_{18}^{0}$ crystals. This crystal morphology resulted in the most interesting of the four different structures seen from this study. Its formation was also the most serendipitous of these morphologies and occurred over around a month of time of inactivity. Using the same technique as the cuboid crystal morphology with toluene and ethanol at the saturation point of the nanocluster, the sample precipitated an amorphous black powder with no crystalline material. It was left in the mother-liquor, untouched for a month on a non-vibrationally stabilized shelf. Over this time, the sample reorganized into extremely large needles that spanned the width of the scintillation vial.

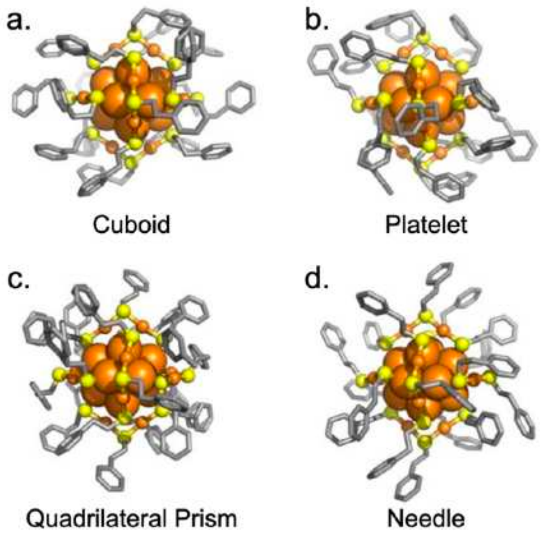

Figure 6.3. Crystal structure of $Au_{25}(PET)_{18}^{0}$ from the different crystal morphologies listed below each image. Shown are the different ligand arrangements around the nanocluster within the solid form.

These needles broke into smaller pieces when the vial was handled but diffracted well. The crystal structure that resulted from this morphology was a previously unpublished structure of $Au_{25}(PET)_{18}^{0}$ and was a chiral structure. This crystal structure is seen in Figure 6.3d.

Comparison of the Different Crystal Structures. Seen in Figure 6.3 are the four different structures of the same $Au_{25}(PET)_{18}^{0}$ material. These structures all have slightly different arrangements of the ligand layer which eventually result in the different morphologies. An analysis of the ligand conformations can be viewed with Dr. Christopher Hosier's dissertation.[17] The analysis includes a viewing of the ligands rotation through is S-C-C-Ph bonds and a viewing of the ligands overall direction within its RS-Au-SR-Au-SR staple unit arrangement. A comparison of gauche or anti rotation down the ligand bonds resulted in three different arrangements within the four different structures. The needle and quadrilateral prism morphologies have the same ligand bond rotations. A determination of the staple unit arrangement can be made between cis-cis, cis-trans, and trans-trans ligand conformations as well. However, all four morphologies have all trans-trans relationships of ligands along the staple units of the nanocluster.

The most interesting result of the comparison of the different structures is the needle morphologies lack of an inversion center. All other published structures of $Au_{25}(PET)_{18}^{0}$ and $Au_{25}(PET)_{18}^{-1}$ with achiral ligands have resulted in achiral structures. Chirality can be induced with mixed ligand layers and chiral ligands added to the surface; however, this structure induced chirality through polymorphic conformations of the achiral PET ligand layer. The solid state properties of this nanocluster therefore are assumed to be different to achiral $Au_{25}(PET)_{18}$. These properties could not be tested, however, as the entirety of the sample was sent off for diffraction and this morphology could not be replicated for testing. The introduction of chirality to a material without ligand exchange could result in new possible applications of gold nanoclusters in the solid state. Without needing further complicated, chemical modifications, new properties can be introduced through polymorphic crystallization.

Crystallographic Technique Extrapolations. The application of slight differences in crystallographic techniques in this case resulted in different crystallographic morphologies. Certain techniques resulted in certain morphologies consistently and so these techniques could possibly applied to other nanocluster materials. In situ oxidation at the saturation point, in situ oxidation in a selective solvent, anti-solvent layering, and solid-state reorganization, all resulted in different morphologies in the case of $Au_{25}(PET)_{18}$.

The in situ oxidation at the saturation point and the anti-solvent layering are done in the same solvent system but with different techniques for reducing the solubility of the material. Toluene and ethanol are used which should have the same molecular/solvent interactions of the crystallizing solid, however, they result in different morphologies, cuboid and quadrilaterial prism, respectively. The in situ oxidation at the saturation point relies on the decreased solubility of the 0 oxidation state over the -1. As the nanocluster oxidizes during gentle heating it precipitates and forms crystals. The anti-solvent layering system relies on the slowly increasing ratio of ethanol to toluene in the vial. As the ethanol increases beyond the saturation point the sample precipitates and forms crystals. In this case, the solvent mixture uses the same solvents but slightly different ratios in final mother-liquor. In the anti-solvent layering system, there is a higher ratio of ethanol to toluene once all the ethanol has diffused into the solution. The anti-solvent layering technique also works best at room temperature for slower diffusion, whereas the in situ oxidation at the saturation point uses gentle heating up to 40-50 °C. We do not currently have a hypothesis for the mechanism resulting in these two different morphologies.

The in-situ oxidation in a selective solvent technique used acetonitrile, which the -1 oxidation state is soluble in and the 0 oxidation state is insoluble. Since acetonitrile can dissolve a large amount of oxygen, the sample readily oxidized within solution and precipitated quickly. Thin platelet crystals were observed and this technique greatly resembles that of a published technique of electrocrystallization within acetonitrile.[16] In this publication, $Au_{25}(PET)_{18}^{-1}$ was slowly oxidized within acetonitrile through bulk electrolysis and resulted in thin hexagonal platelet crystals and long needles based on the current used. It seems that acetonitrile crystallization through oxidation can reliably result in hexagonal or needle-like platelet morphologies as these were observed in this lab as well.

The solid-state reorganization technique is the most inscrutable way to form a unique morphology of $Au_{25}(PET)_{18}^{0}$. Since this technique was a serendipitous formation of unique crystals and could not be replicated, we know very little of this method. The sample slowly went from amorphous powder to large needle crystals over the period of a month. Similar techniques are used for the crystallization of biomacromolecules in a much smaller format. The crystallization of $Au_{102}(pMBA)_{44}$ was also done through vapor diffusion where the sample is precipitated out initially then slowly as the composition of salts and pH change within the solution, it reorganizes to a crystalline product. This system is assumed to function in a similar way. Regardless, this crystallization technique resulted in the most interesting morphology and crystal structure and it the most interesting for further research.

Expanding to Other Materials. Recently within other lab work, two different morphologies have been observed for a different nanocluster, $Au_{133}(tBBT)_{52}$. The most common morphology seen is a hexagonal platelet from the crystallization of this nanocluster from acetonitrile layered over dichloromethane. However, during the same crystallization technique with no obvious changes to the process, needle shaped crystals have been observed as well. Figure 6.4 shows these two morphologies. It is possible that the samples are in different oxidation states from environmental factors. The samples come directly from synthesis and purification and are assumed to be in the 0 oxidation state. Those that form needles have taken longer to crystallize and have been exposed to atmosphere longer so this is a reasonable hypothesis.

6.5 Conclusion

Within this work, four different crystallization techniques were discussed which resulted in four different morphologies of crystals and four different crystal structures of $Au_{25}(PET)_{18}^{0}$. Interestingly, the structure that occurred from the needle morphology is the first $Au_{25}(PET)_{18}$ solid structure to be chiral without mixed ligand layers or chiral ligands added to the surface of

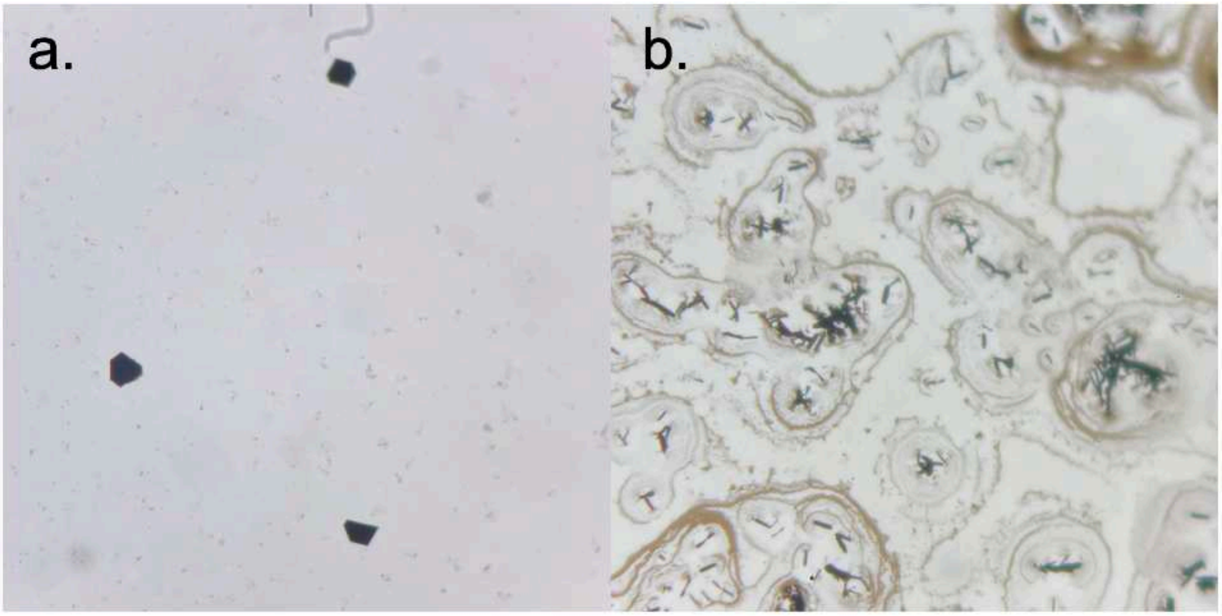

Figure 6.4. Photographs of $Au_{133}(tBBT)_{52}$ crystals taken through a microscope with similar scales. **a.** hexagonal platelet morphology and **b.** needle morphology.

the nanocluster. The needle and platelet morphologies were also previously unpublished structures of $Au_{25}(PET)_{18}^{0}$ that could result in different properties from the nanocluster in the solid state. Within this chapter hypotheses were given for the different morphologies formed from slightly different crystallization techniques that include different solvent conditions, temperatures, and techniques. The control of the oxidation state at the time of dissolution, control of the solvent to anti-solvent ratios, control of the temperature, control of the solvent used, and control of the handling of the solution all seem to have influences on the morphology of the crystals produced.

Further analysis is currently being performed on the geometric differences of these different morphologies as well as theoretical properties of the unique needle morphology. Collaborators have worked on taking the empirical structures solved from diffraction data and relaxed them through theoretical studies. Full analysis of the angles of each ligand as well as core distortions are being performed. Theoretical analysis of the needle morphology and its chiral nature has been done to look at the non-linear optical properties of this unique nanocluster structure. Hopefully in the future, this crystal morphology can be grown again and the empirical, solid-state properties can be investigated. Optical properties will be different due to the chiral nature, and other properties are assumed to have slight differences as well. The crystallographic techniques within can be applied to other gold nanoclusters for slightly different polymorphic conformations of solid state materials.

Chapter 6 References

(1) Ni, T. W.; Tofanelli, M. A.; Ackerson, C. J. Structure Determination by Single Crystal X-Ray Crystallography. *Front. Nano.* **2015**, 103–125.

(2) Bain, D.; Maity, S.; Paramanik, B.; Patra, A. Core-Size Dependent Fluorescent Gold Nanoclusters and Ultrasensitive Detection of Pb^{2+} Ion. *ACS Sustain. Chem. Eng.* **2017**, *6* (2), 2334–2343.

(3) Nimmala, P. R.; Yoon, B.; Whetten, R. L.; Landman, U.; Dass, A. Au(67)(SR)(35) Nanomolecules: Characteristic Size-Specific Optical, Electrochemical, Structural Properties and First-Principles Theoretical Analysis. *J. Phys. Chem. A* **2013**, *117* (2), 504–517.

(4) Plascencia Villa, G.; Demeler, B.; Whetten, R. L.; Griffith, W. P.; Alvarez, M.; Black, D. M.; José-Yacamán, M. Analytical Characterization of Size-Dependent Properties of Larger Aqueous Gold Nanoclusters. *J. Phys. Chem. C* **2016**, *120* (16), 8950–8958.

(5) Rambukwella, M.; Sementa, L.; Barcaro, G.; Fortunelli, A.; Dass, A. Organosoluble $Au_{102}(SPh)_{44}$ Nanomolecules: Synthesis, Isolation, Compositional Assignment, Core Conversion, Optical Spectroscopy, Electrochemistry, and Theoretical Analysis. *J. Phys. Chem. C* **2015**, *119* (44), 25077–25084.

(6) Jensen, K. M. Ø.; Juhas, P.; Tofanelli, M. A.; Heinecke, C. L.; Vaughan, G.; Ackerson, C. J.; Billinge, S. J. L. Polymorphism in Magic-Sized $Au_{144}(SR)_{60}$ Clusters. *Nat Commun* **2016**, *7* (1), 11859.

(7) Nag, A.; Chakraborty, P.; Bodiuzzaman, M.; Ahuja, T.; Antharjanam, S.; Pradeep, T. Polymorphism of $Ag_{29}(BDT)_{12}(TPP)_{4}{}_{3-}$ Cluster: Interactions of Secondary Ligands and Their Effect on Solid State Luminescence. *Nanoscale.* **2018**, *10* (21), 9851–9855.

(8) Zhu, M.; Eckenhoff, W. T.; Pintauer, T.; Jin, R. Conversion of Anionic $[Au_{25}(SCH_2CH_2Ph)_{18}]^-$ Cluster to Charge Neutral Cluster via Air Oxidation. *J. Phys. Chem. C* **2008**, *112* (37), 14221–14224.

(9) Tofanelli, M. A.; Salorinne, K.; Ni, T. W.; Malola, S.; Newell, B.; Phillips, B.; Häkkinen, H.; Ackerson, C. J. Jahn–Teller Effects in $Au_{25}(SR)_{18}$. *Chem. Sci.* **2016**, *7* (3), 1882–1890.

(10) Jaakko Akola; Michael Walter; Robert L Whetten; Hannu Häkkinen; Grönbeck, and H. On the Structure of Thiolate-Protected Au_{25}. *J. Am. Chem. Soc.* **2008**, *130*.

(11) Singh, R. Unexpected Magnetism in Nanomaterials. *J. Mag. Mag. Mat.* **2013**, *346*, 58–73.

(12) Trudel, S. Unexpected Magnetism in Gold Nanostructures: Making Gold Even More Attractive. *Gold Bull.* **2011**, *44* (1), 3–13.

(13) Nealon, G. L.; Donnio, B.; Greget, R.; Kappler, J.-P.; Terazzi, E.; Gallani, J.-L. Magnetism in Gold Nanoparticles. *Nanoscale* **2012**, *4* (17), 5244–5258.

(14) Vippagunta, S. R.; Brittain, H. G.; Grant, D. J. W. Crystalline Solids. *Advanced Drug Delivery Reviews* **2001**, *48* (1), 3–26.

(15) Ni, T. W.; Tofanelli, M. A.; Phillips, B. D.; Ackerson, C. J. Structural Basis for Ligand Exchange on $Au_{25}(SR)_{18}$. *Inorg. Chem.* **2014**, *53* (13), 6500–6502.

(16) Antonello, S.; Dainese, T.; Pan, F.; Rissanen, K.; Maran, F. Electrocrystallization of Monolayer-Protected Gold Clusters: Opening the Door to Quality, Quantity, and New Structures. *J. Am. Chem. Soc.* **2017.**

(17) Hosier, C. A. The Dynamic Nature of Ligand Layers on Gold Nanoclusters. Colorado State University, 2020.

Chapter 7: Summary of Studies

Gold nanoclusters are very stable and interesting materials for numerous applications, however, understanding where their properties come from through fundamental research is necessary to expand the possibilities for the materials. Applying the superatom theory to these materials allows for the study of their electronic structure through empirical experimentation. Careful control of their surface structure (ligand layer) allows for better understanding of how to functionalize these materials for applications in the future.

In order to understand gold nanoclusters electronic structure as their sizes change from very molecular materials to near bulk materials, magnetic studies have been performed on larger gold nanoclusters to compare to small nanocluster data. Applying superatom theory to these materials and comparing the proposed frontier orbitals, 1G and 1H orbitals of $Au_{102}(SR)_{44}$ and $Au_{133}(SR)_{52}$, respectively, to the magnetic data found gives plentiful information of how these orbital behave through different oxidation states. This data shows that as the gold nanoclusters increase in size, they can support higher and higher numbers of electron spins within solution. Since magnetism in gold only occurs in very small materials, this shows and interesting balance of the materials being small enough to have quantum confinement, but large enough for significant geometric stabilization to allow for larger oxidation states changes from the HOMO-LUMO gap. These studies presented within are some of the first empirical studies of the electronic structure of larger, near-bulk gold nanocluster materials. As the behavior of gold nanocluster electronics changes so much through core-size changes, certain sizes are more preferable for selective future applications.

In addition to these very core-centered properties of the electronic structure of gold nanoclusters, ligand layer studies and structural analyses are presented within that focus on the interactions of the gold nanocluster with its environment and other nanoclusters and the effect of this on their properties. Ligand interactions of the gold nanocluster and intercluster interactions are different within solution and solid phase but can be viewed similarly through experimental studies. Different ligands result in different behaviors of the nanocluster which are not fully understood enough even after decades of study to predict behavior. Ligand exchange and mixed ligand layers on a nanocluster further complicate the issue of selecting certain ligands for certain applications.

The research performed within displays how much new information is still available to discover through fundamental research of gold nanocluster materials. The investigation of nanocluster properties from core to ligand is still necessary to understand how we could choose nanocluster nuclearity, ligand layer, geometry, and oxidation state for future targeted applications.

Appendix I: Supporting Information for Chapter 2

Experimental

$Au_{102}(SPh)_{44}$ synthesis: $Au_{102}(SPh)_{44}$ was synthesized by dissolving 0.301 g (0.762 mmol) of $HAuCl_4•3H_2O$ in 20 mL of THF. To this solution, 0.613 mL (4.571 mmol) of 1-phenylethanethiol (PET) was added. This solution was stirred at 500 rpm for 30 min to go from orange to clear with white precipitate. An 5 mL aqueous solution containing 0.288 g (7.620 mmol) of $NaBH_4$ was prepared and cooled to 0 C°. This solution was then added rapidly to the THF solution and stirred for 5 min. Excess methanol (MeOH) was added to this flask then rotovaped slowly until bubbling ceased. All solvent was then removed under vacuum. The solution was then washed with MeOH until no thiol smell was observed then extracted with DCM.

The crude sample was dissolved in a minimal amount of toluene and heated to 60°C. To this, 2 µL of PET per mg of crude was added and stirred at 60°C for 3 hours. Solvent was then removed under vacuum and the solution was washed with MeOH until no thiol smell remained. The crude sample was dissolved again in a minimal amount of toluene and heated to 80°C. To this 10 µL of benzenethiol (SPh) per mg of crude was added and stirred at 80°C for 30 min. Solvent was then removed under vacuum and the solution was washed with MeOH until no thiol smell remained. The sample was then extracted with DCM.

$Au_{102}(SPh)_{44}$ purification: $Au_{102}(SPh)_{44}$ crude sample was dissolved in 2:1 DCM:Hexanes solvent mixture and run through a dry packed Flash silica gel column with 2:1 DCM:Hexanes until no colored product came out. This eluent contained a significant amount of

$Au_{67}(SR)_{22}$ sized product. The desired product, $Au_{102}(SPh)_{44}$, was then collected with THF through the silica gel column. The desired sample was then run through size exclusion chromatography columns with THF solvent with BioBeads SX1 column stationary phase to remove 33 and 35 kDa species until pure by MALDI-MS on a Bruker MicroFlex using DCTB matrix.

$Au_{102}(SPh)_{44}^{-1/+1/+2}$ electrolysis: $Au_{102}(SPh)_{44}^{-1/+1/+2}$ was synthesized though bulk electrolysis in a 50mM solution of tetrabutylammonium hexafluorophosphate ($TBAPF_6$) in HPLC-grade DCM. The sample was dissolved in the solution of $TBAPF_6$ and electrochemical processes were done in a three-compartment cell. First, a square wave voltammogram (SWV) was obtained to locate the charge state wells. A glassy carbon working electrode was used for the SWV with a Ag/AgCl reference and platinum counter electrode. Bulk electrolysis was then performed at the resulting potentials observed in the SWV. Charge state was then verified through open circuit potential measurements using a glassy carbon electrode and compared to a SWV taken after bulk electrolysis with a glassy carbon working electrode used. For bulk electrolysis, platinum working and counter electrodes were used with a Ag/AgCl reference electrode. Electrode use was changed from glassy carbon to platinum and back since the platinum working electrode used for bulk electrolysis is a mesh which can adversely affect voltammetry methods. However, electrochemical performance was checked on both electrodes and were identical except for some issues with signal intensity. For the -1 charge state, all solvents were degassed before electrolysis. Immediately after bulk electrolysis, solvent was removed under vacuum at room temperature, then washed with degassed and dry acetonitrile to remove $TBAPF_6$ salts. The sample was then washed with ethanol (EtOH) then dried under high vacuum to prepare for Evans Method ^{1}HNMR measurements.

Evans Method ^{1}H NMR: $Au_{102}(SPh)_{44}^{-1/0/+1/+2}$ in each charge state was separately dissolved in ~600 µL of chloroform-d with 0.1% tetramethylsilane (TMS) added and placed in an NMR tube. For the -1 charge state the solvent was degassed with argon gas. To this NMR tube, a capillary was added with the same chloroform-d and 0.1% TMS solution. ^{1}H NMR experiments were performed with a 400MHz NMR.

Evans Method Discussion

Evan's method measures the magnetic response of materials in solution by examining the pseudocontact shift of NMR signals and relating this shift to a magnetic response. The material of interest in solution with shift the NMR signal of your analyte (solvent or standard) based on its different diamagnetic or paramagnetic properties. Evan's Method measurements were done in deuterated chloroform with the tetramethylsilane (TMS) as the analyte NMR signal being tracked for pseudocontact shifts due to magnetic behavior of the nanocluster. Equation 1 below was then used to calculate the magnetic susceptibility.

Equation 1.

$$X_M^p = \frac{1}{v_0 S_f}\left[\frac{\delta v^p M^p}{m^p} - \frac{\delta v^{dia} M^{dia}}{m^{dia}}\right]$$

This equation calculated the paramagnetic molar susceptibility of a sample based on subtracting the molar pseudocontact shift of the diamagnetic analogue of the nanocluster (the "0" charge state) from the molar pseudocontact shift of the +1, +2, or -1 charge state nanoclusters to obtain the molar paramagnetic response of the pseudocontact shift peak.

Data

Table SI.1.1. Total Evan's Method data used for calculating magnetic susceptibilities.

Charge State	δv (Hz)	mass of sample (mg)
0	-8.4	19
0	-10.4	18.62
0	-8.4	20.33
1	-7.6	13.8
1	-6	15.13
1	-3.6	9.69
1	-3.2	10.15
1	-3.84	13.5
2	-4	13.06
2	-4.4	18.09
2	-3.876	12.41
2	-4.224	13.1
-1	-2.8	17.29
-1	-3.2	11.92

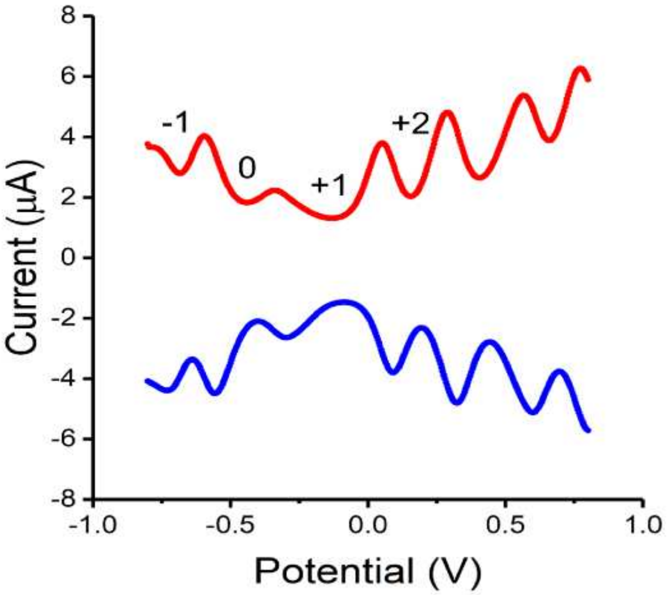

Figure SI.1.1. Square wave voltammogram with charge state designations shown in charge state wells

Charge State Designation: Traditionally, the larger well between the electrochemical gap would be considered the 0 charge state well. However, when looking at the molar pseudocontact shift values, the largest negative value indicates the diamagnetic analogue and corresponds to the 0 charge state. This happens to be the smaller well to the left that sits around -0.5V vs Ag/AgCl.

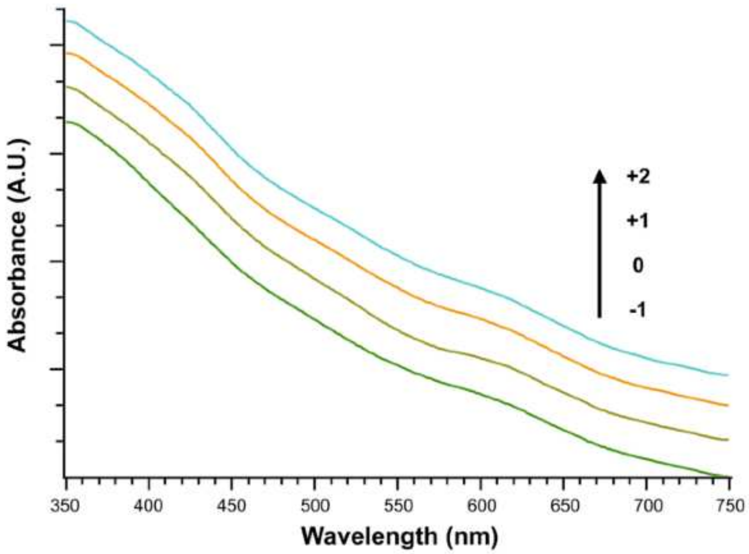

Figure SI.1.2. UV-Vis Spectra of $Au_{102}(SPh)_{44}^{-1/0/+1/+2}$ in distinct charge states showing no significant differences across oxidation states.

UV-Vis Spectra: UV-Vis spectra were collected in DCM with 100mM $TBAPF_6$ in different oxidation states after bulk electrolysis. No significant differences were seen with oxidation state changes as seen in Figure S2.

Full 1H NMR Data: Below are included the full NMR spectra (SI.1.3) where the "δv" data in Table S1 can be found. Each figure shows the 1H NMR spectrum from 10 ppm to -1 ppm on the left. A second figure is on the right of each image with the 0.05 ppm to -0.05 ppm region of the spectrum shown for the TMS peak shift regions. Each image is labeled with the charge state and data point number in the top left. (eg 0.1 is charge state 0 data point 1 in Table SI.1.1).

Figure SI.1.3. Full NMR spectra for Chapter 2.

1.1

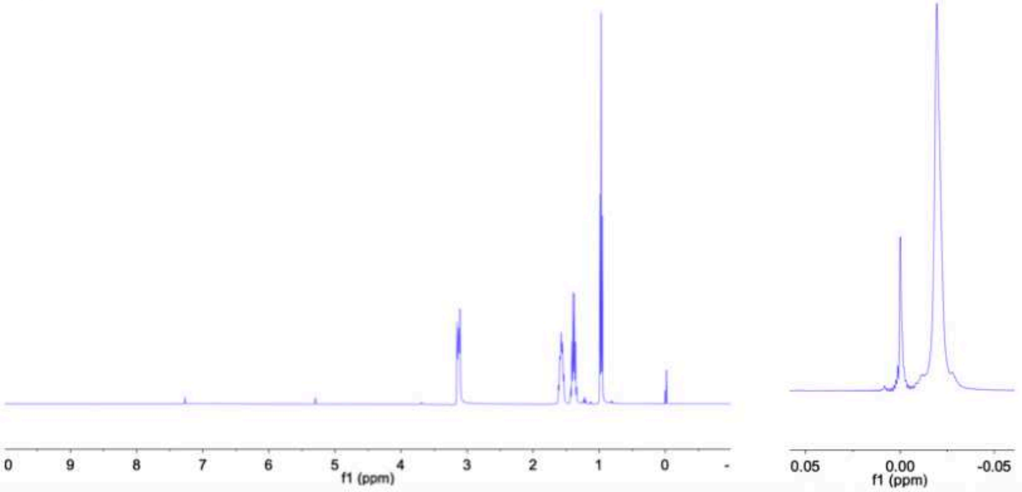

1.2

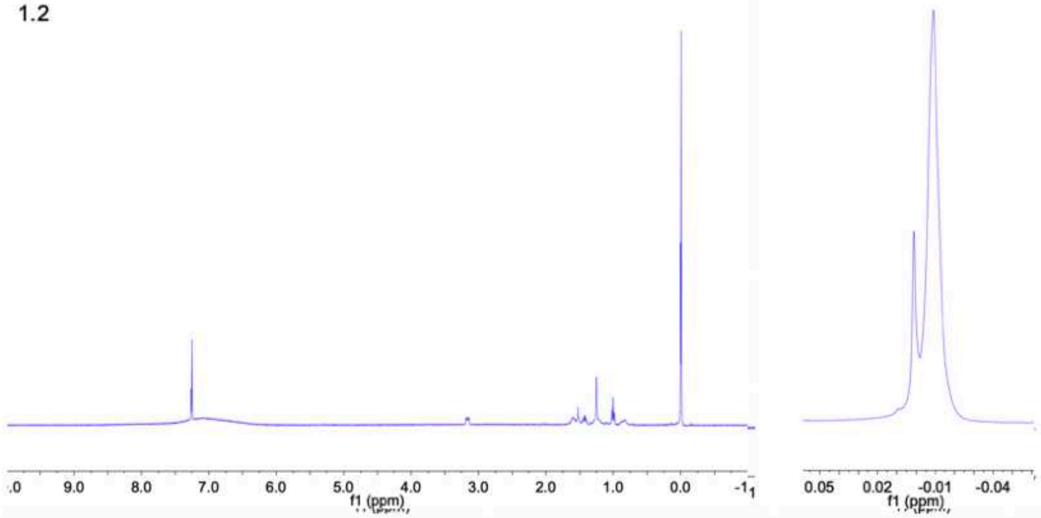

1.3

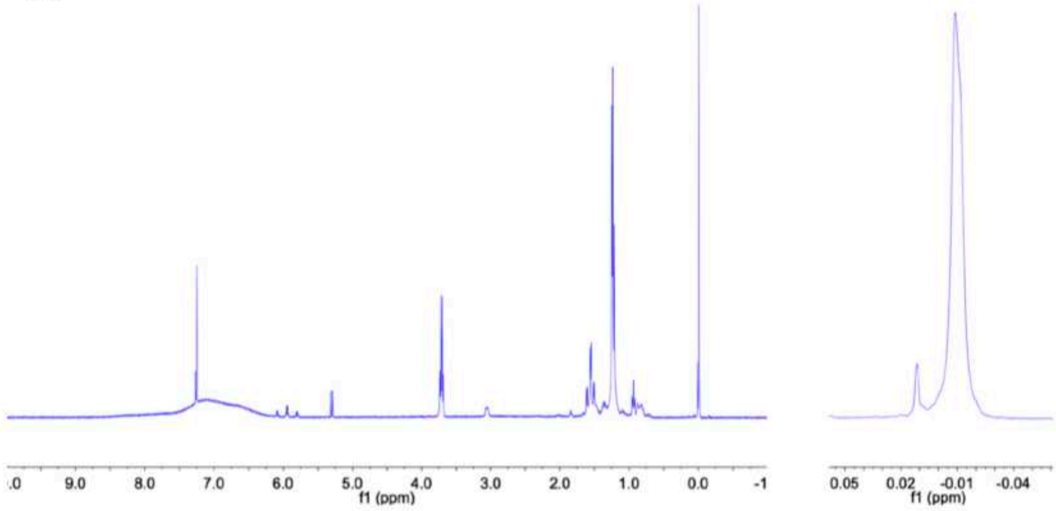
.0
9.0
8.0
7.0
6.0
5.0
4.0
3.0
2.0
1.0
0.0
-1
f1 (ppm)
0.05
0.02
-0.01
-0.04
f1 (ppm)

1.4

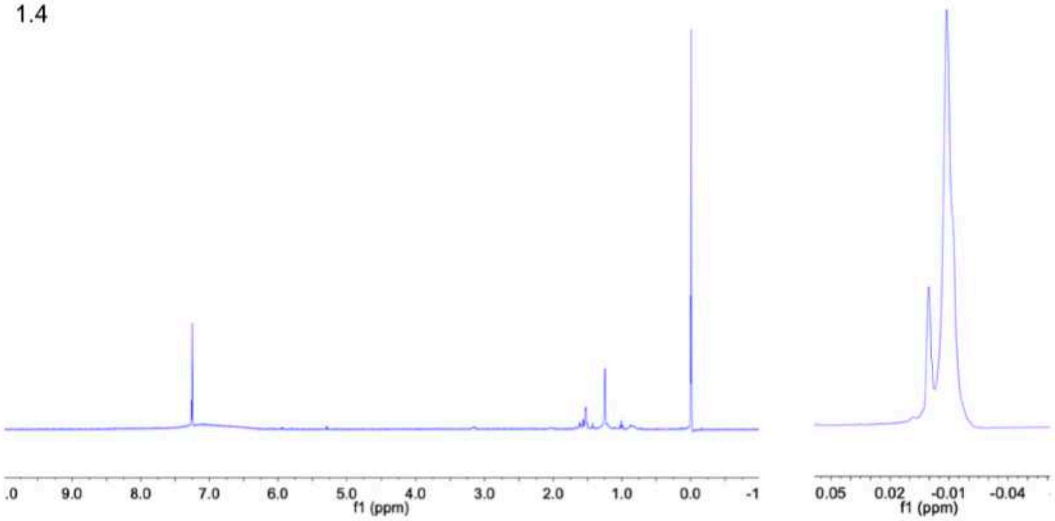
.0
9.0
8.0
7.0
6.0
5.0
4.0
3.0
2.0
1.0
0.0
-1
f1 (ppm)
0.05
0.02
-0.01
-0.04
f1 (ppm)

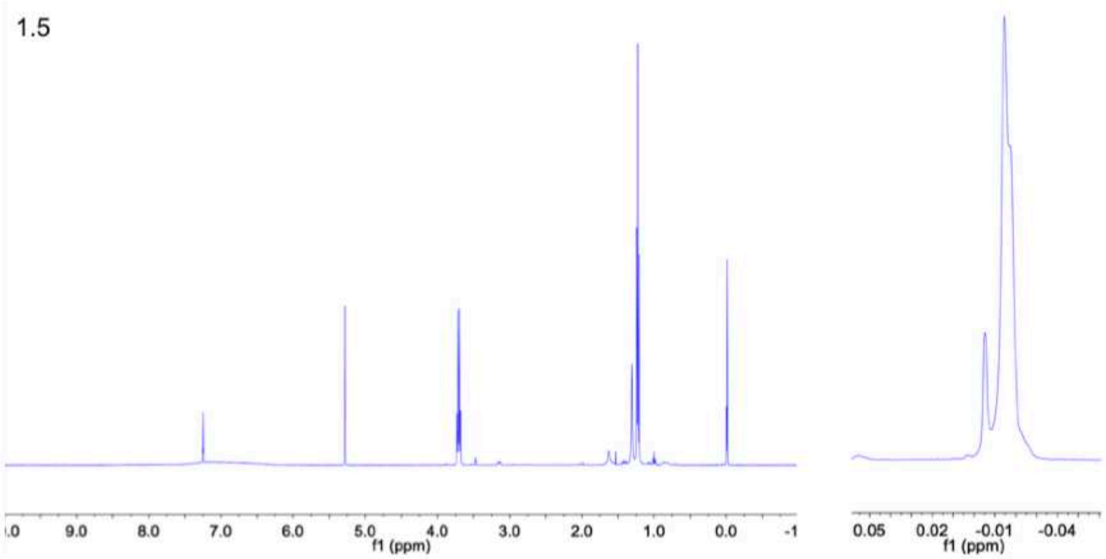
1.5
9.0
8.0
7.0
6.0
5.0
4.0
3.0
2.0
1.0
0.0
-1
f1 (ppm)
0.05
0.02
-0.01
-0.04
f1 (ppm)

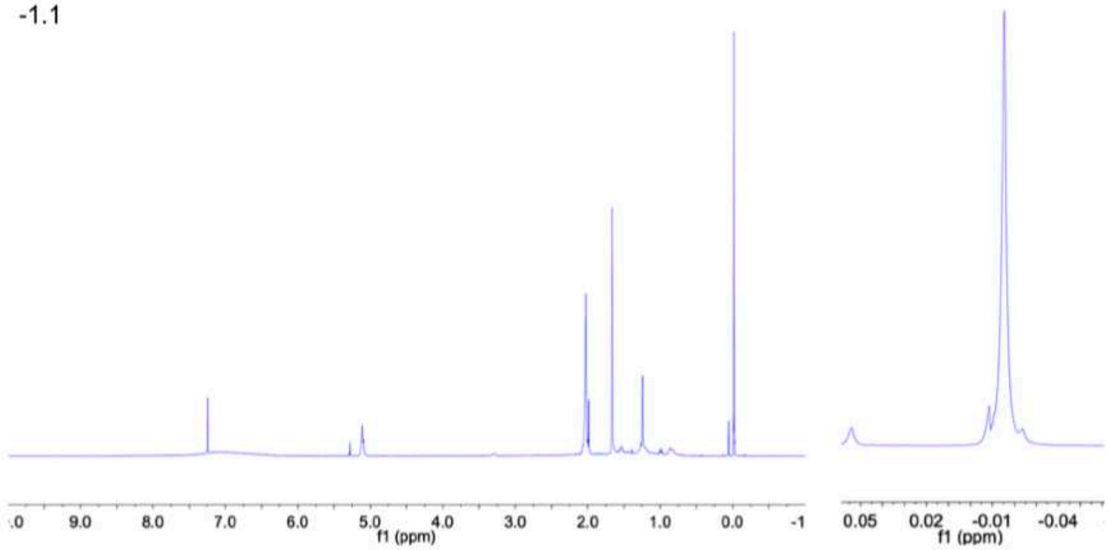
-1.1
9.0
8.0
7.0
6.0
5.0
4.0
3.0
2.0
1.0
0.0
-1
f1 (ppm)
0.05
0.02
-0.01
-0.04
f1 (ppm)

-1.2

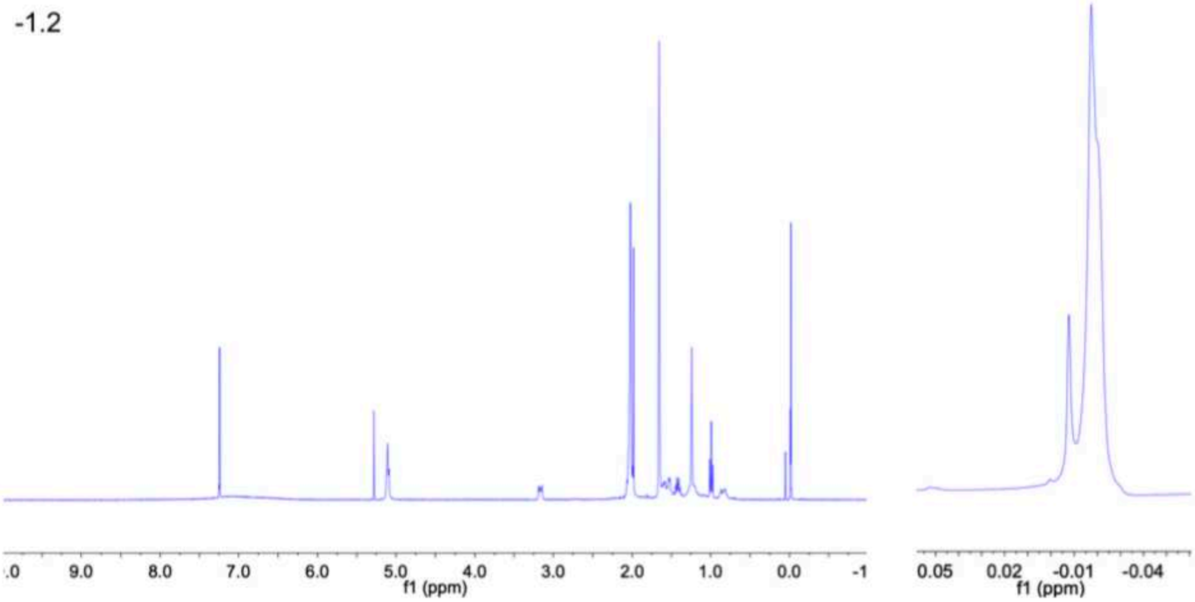

.0
9.0
8.0
7.0
6.0
5.0
4.0
3.0
2.0
1.0
0.0
-1
f1 (ppm)
0.05
0.02
-0.01
-0.04
f1 (ppm)

0.1

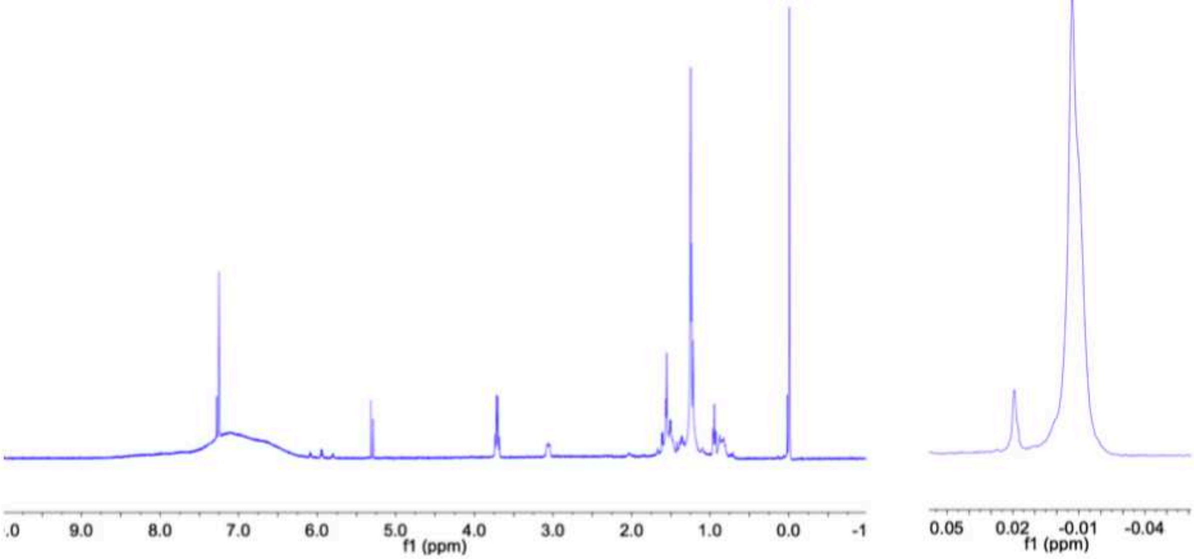

.0
9.0
8.0
7.0
6.0
5.0
4.0
3.0
2.0
1.0
0.0
-1
f1 (ppm)
0.05
0.02
-0.01
-0.04
f1 (ppm)

0.2

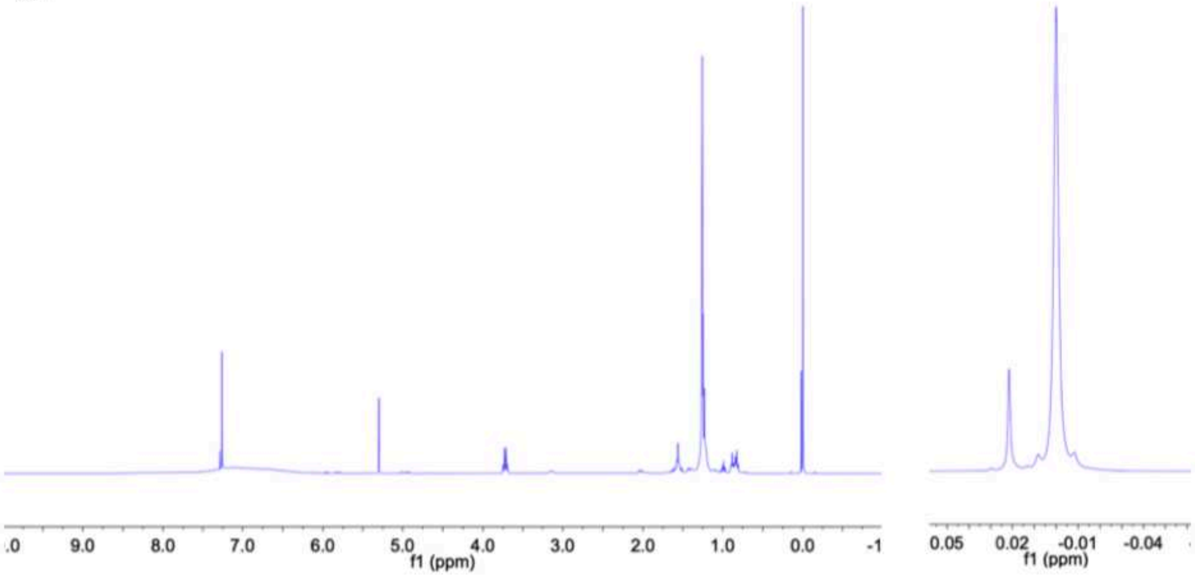
.0
9.0
8.0
7.0
6.0
5.0
4.0
3.0
2.0
1.0
0.0
-1
f1 (ppm)
0.05
0.02
-0.01
-0.04
f1 (ppm)

0.3

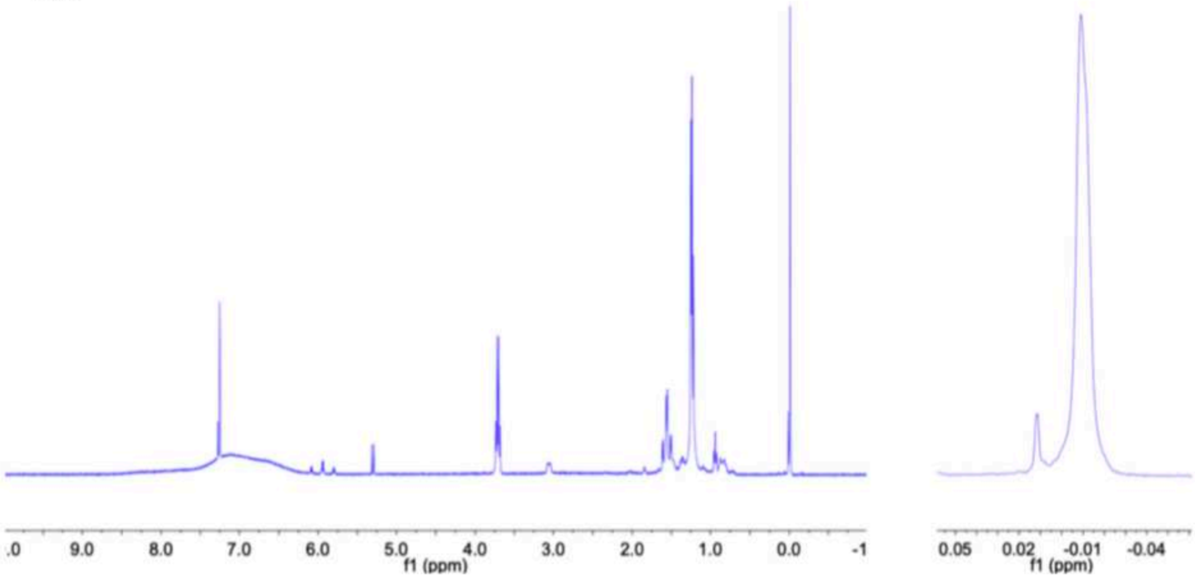
.0
9.0
8.0
7.0
6.0
5.0
4.0
3.0
2.0
1.0
0.0
-1
f1 (ppm)
0.05
0.02
-0.01
-0.04
f1 (ppm)

2.1

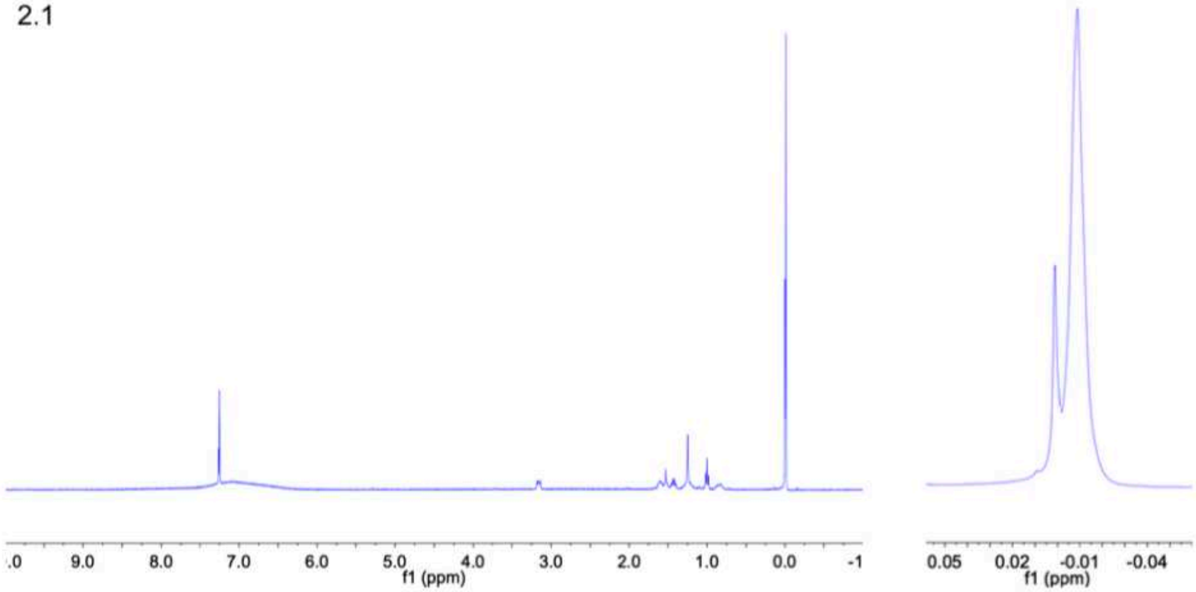
.0
9.0
8.0
7.0
6.0
5.0
4.0
3.0
2.0
1.0
0.0
-1
f1 (ppm)
0.05
0.02
-0.01
-0.04
f1 (ppm)

2.2

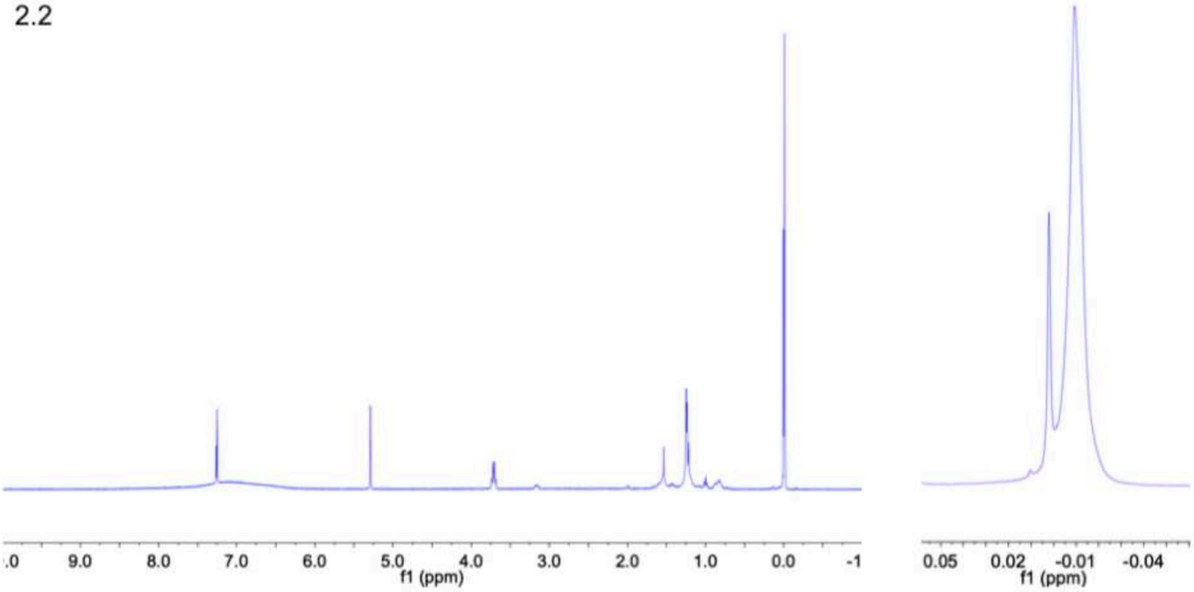
.0
9.0
8.0
7.0
6.0
5.0
4.0
3.0
2.0
1.0
0.0
-1
f1 (ppm)
0.05
0.02
-0.01
-0.04
f1 (ppm)

Appendix II: Supplementary Information for Chapter 3

Experimental

Synthesis of $Au_{144}(tBBT)_{60}$: $Au_{144}(PET)_{60}$ was synthesized by dissolving 0.472 g (1.2 mmol, 1.0 eq.) of $HAuCl_4$•$3H_2O$ and 760 mg (1.39 mmol, 1.16 eq.) of TOABr in 60 mL of methanol. To this solution, 0.840 mL (5.89 mmol, 4.9 eq.) of 1-phenylethanethiol (PET) was added. This solution was stirred at 500 rpm for 15-30 min to go from red-orange to clear with white precipitate. A 24 mL aqueous solution containing 0.456 g (12.0 mmol, 10 eq.) of $NaBH_4$ was prepared and cooled to 0 C°. This solution was then added rapidly to the methanol solution and stirred for 48 hours. After this time, DCM and nano-pure water were added to this solution and the DCM layer was extracted through a separatory funnel. The DCM was then removed under vacuum and the crude sample suspended in methanol The solution was then washed with methanol by centrifugation until no thiol smell was observed then extracted with DCM.

The crude $Au_{144}(PET)_{60}$ sample was then purified by size exclusion chromatography (SEC) to remove the small fraction of $Au_{25}(PET)_{18}$ that is produced from this synthesis. The $Au_{144}(PET)_{60}$ sample elutes from the column as a black solution in THF. After collection and removal of solvent, the sample was weighed.

Synthesis of $Au_{133}(tBBT)_{52}$: 10 mg (2.73E-4 mmol, 1eq.) of $Au_{144}(PET)_{60}$ sample was dissolved in 1 mL of toluene in a small scintillation vial. 1 mL (5.797 mmol, 2.12E4 eq.) of 4-tert-butylbenzenethiol was added to this solution. Two methods are possible for the thermoetching of the solution to $Au_{133}(tBBT)_{52}$, sand bath heating and oil bath heating. When heating in an oil bath, the sample was submerged in 80°C oil and stirred gently for 48 hours. When heating in the sand bath, the temperature probe was inserted into a matching volume solution of toluene for temperature control. The sample solution was heated at 80°C for 24 hours only, as more than this would result in decomposition of the material into insoluble powder. The solvent was then removed under vacuum (as much as possible). The solution was then washed with methanol by centrifugation with at least 200 mL of methanol added.

Crystallization of $Au_{133}(tBBT)_{52}$: The sample of $Au_{133}(tBBT)_{52}$ was extracted with DCM and centrifuged for the removal of dust and precipitate to prepare for crystallization. With around 2-5 mg of sample within a scintillation vial and less than two mL of DCM, the solution can be layered with acetonitrile and crystallizes readily. To start acetonitrile can be layered over DCM carefully with a ratio of 1:2 by volume. If this solution does not produce crystals, the supernatant is filtered off then more acetonitrile is carefully added with much smaller amounts over the mother-liquor. This process works for unexchanged, tBBT protected nanocluster and the exchanged nanoclusters with mixed 4BBT and tBBT ligand layers.

Electrolysis of $Au_{133}(tBBT)_{52}$: $Au_{133}(tBBT)_{44}^{-1/0/+1/+2}$ was formed though bulk electrolysis in a 50mM solution of tetrabutylammonium hexafluorophosphate ($TBAPF_6$) in HPLC-grade DCM. The sample was dissolved in the solution of $TBAPF_6$ and electrochemical processes were done in a three-compartment cell. First, a square wave voltammogram (SWV) was obtained to locate the charge state wells. A glassy carbon working electrode was used for the SWV with a Ag/AgCl reference and platinum counter electrode. Bulk electrolysis was then performed at the resulting potentials observed in the SWV. Charge state was then verified through open circuit potential measurements using a glassy carbon electrode and compared to a SWV taken after bulk electrolysis with a glassy carbon working electrode used. For bulk electrolysis, platinum working and counter electrodes were used with a Ag/AgCl reference electrode. Electrode use was changed from glassy carbon to platinum and back since the platinum working electrode used for bulk electrolysis is a mesh which can adversely affect voltammetry methods. However, electrochemical performance was checked on both electrodes and were identical except for some issues with signal intensity. For the -1 and -2 oxidation states, all solvents were degassed before electrolysis and the electrolysis cells' head-space was covered with argon gas flow. Immediately after bulk electrolysis, solvent was removed under vacuum at room temperature, then washed with degassed and dry acetonitrile to remove $TBAPF_6$ salts. The sample was then washed with ethanol (EtOH) then dried under high vacuum to prepare for Evans Method ^1H NMR measurements.

Evans Method ^1H NMR: $Au_{133}(tBBT)_{52}^{-1/0/+1/+2}$ in each oxidation state was separately dissolved in ~600 µL of chloroform-d with 0.1% tetramethylsilane (TMS) added and placed in an NMR tube. For the -1 oxidation state the solvent was degassed with argon gas. To this NMR tube, a capillary was added with the same chloroform-d and 0.1% TMS solution. ^1H NMR experiments were performed with a 400MHz NMR.

Voltammograms of $Au_{133}(tBBT)_{52}$: Figure SI.2.1 shows the square wave voltammograms of $Au_{133}(tBBT)_{52}$ after electrolysis into the 5 different oxidation states of the nanocluster, -2,-1,0,+1,+2. Bulk electrolysis was performed as described above then voltammograms were recorded with the open circuit potential of the sample solution shown on the graph for that oxidation state. There are small changes between the different oxidation states with different signal strengths and small movements of the oxidation state wells, however, not enough changes for a lengthy analysis of the different effects of the oxidation states.

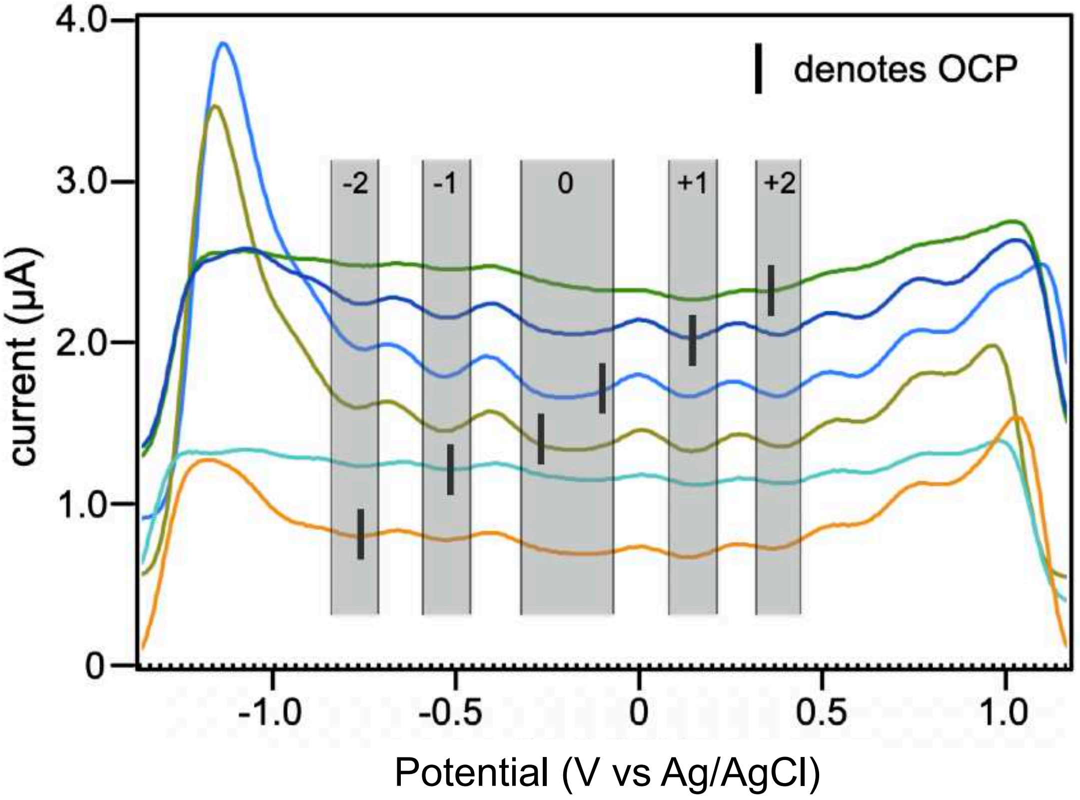

Figure SI.2.1. Voltammograms of $Au_{133}(tBBT)_{52}$ taken after bulk electrolysis and open circuit potential (OCP) measurements into each oxidation state well. Highlighted are the oxidation state wells with labels and black lines mark the measured OCP of the material ensuring the correct oxidation state from -2 to +2.

Appendix III: Supplementary Information for Chapter 4

Experimental

$Au_{25}(SC_6H_{13})_{18}$ synthesis: $Au_{25}(SC_6H_{13})_{18}$ was synthesized by dissolving 1.00 g (2.54 mmol) of $HAuCl_4•3H_2O$ with 1.56 g (2.85 mmol) of TOABr in 70 mL of THF. This was stirred at 500 rpm for 30 min until it was a clear orange-red solution. To this solution, 1.8 mL (13.4 mmol) of 1-hexanethiol was added. This solution was stirred at 500 rpm for 1-12 hours to go from orange-red to clear with white precipitate. A 24 mL aqueous solution containing 956 mg (25.6 mmol) of $NaBH_4$ was prepared and cooled to 0 C°. This solution was then added rapidly to the THF solution and stirred for 48 hours. Excess methanol (MeOH) was added to this flask then rotovaped. All solvent was removed under vacuum. The solution was then washed with MeOH until no thiol smell was observed then extracted with DCM.

$Au_{25}(SC_6H_{13})_{18}$ purification: $Au_{25}(SC_6H_{13})_{18}$ crude sample was dissolved in THF and then run through size exclusion chromatography columns with THF solvent with BioBeads SX1 column stationary phase to remove $Au_{144}(SC_6H_{13})_{60}$ byproduct species until pure by MALDI-MS on a Bruker MicroFlex using DCTB matrix.

$Au_{25}(SC_6H_{13})_{18}$ oxidation: Pure $Au_{25}(SC_6H_{13})_{18}^{-1}$ was dissolved in DCM then run through a silica gel column to oxidize to $Au_{25}(SC_6H_{13})_{18}^{0}$.

DLS Methodology: A Malvern Zetasizer instrument was used for all DLS investigations. For preparation of samples, the $Au_{25}(S(CH_2)_5CH_3)_{18}^{0}$ sample was first dissolved in a small amount of toluene. 0.20 mL of this solution was added to a 1.5 mL eppendorf tube. Then, 0.80

mL of ethanol was added to this tube and mixed thoroughly. This sample was diluted with more 80% ethanol 20% toluene solution and UV-Vis spectroscopy was used to test the optical density at 450 nm for a concentration comparison. After optical density was taken, the eppendorf tube solution was spun down at 14000 rpm for 15 minutes. It was then carefully decanted into a second clean eppendorf tube and centrifuged again to ensure no dust particulates. This was decanted into another clean eppendorf tube and ready for DLS studies.

Samples were transferred to fluorometry cuvettes using pasteur pipettes cleaned by compressed air. The cuvettes were then capped and the caps were not removed during DLS studies.

Other percentages of anti-solvent to solvent were prepared using the same method discussed above.

Ligand Choice

Ligand choice also plays a large role in the formation of superclusters as evidenced from the lack of supercluster formation observed for $Au_{25}(PET)_{18}^{0/-1}$ (PET being phenylethanethiol) in either stable oxidation state tested. This could be from the stronger interactions with the solvent system because of the aromatic carbon ring. Much higher antisolvent concentrations were required before saturation of the system occurred and then at > 95% ethanol amounts precipitation occurs before a stable two phase system at the tested temperatures. From this it can be inferred that the decreased strength intramolecular interactions and reduced solubility of the hexanethiol protected nanocluster aided the formation of superclusters. An increased solvent/ antisolvent mixture window seems available before precipitation from solution for the hexanethiol protected nanoclusters. Intercalation of the alkyl chains from ligands is proposed to stabilize the assemblies as well as the surface gold interactions.

Variable Temperature UV-Vis

UV-Vis Spectrometry was performed on an 80/20% Ethanol/Toluene sample of $Au_{25}(PET)_{18}^0$ nanoclusters at different temperatures. Temperature control was achieved by using water and ice baths for the 0 – 39 °C. -5 °C was achieved through an acetone/ice bath. Temperature was measured in a blank solution of the same volume and container. 39°C was found to be warm enough for the superclusters to disassociate within DLS measurements for an 80/20% Ethanol/Toluene sample. VT-UV-Vis was performed on a 0.217 absorbance sample at 450 nm using an Ocean Optics dip-probe UV-Vis. As seen within Figure SI.3.1 there are no significant changes to the spectra as the sample is cooled. Figure SI.3.2 is an optical spectrum of the same sample within a normal, closed-chamber, cuvette UV-Vis without the artifact present from the dip-probe instrument.

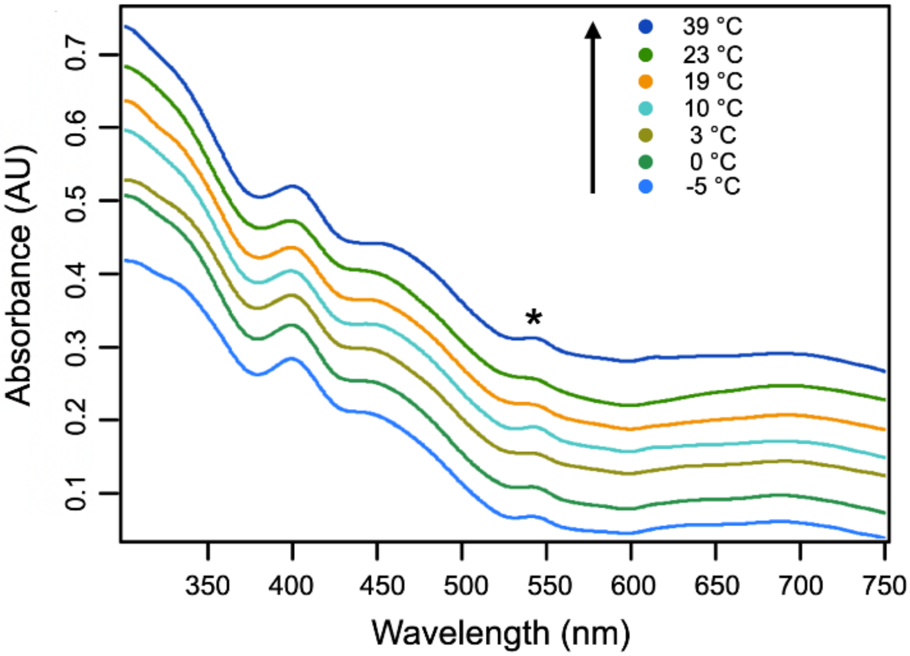

Figure SI.3.1. Variable Temperature UV-Vis spectra from -5 °C to 39 °C, taken with dip-probe spectrometer. No changes are seen within the 3 features usually seen within $Au_{25}(SR)_{18}^0$ (400, 450, and 680 nm peaks). Asterisk denotes artifact

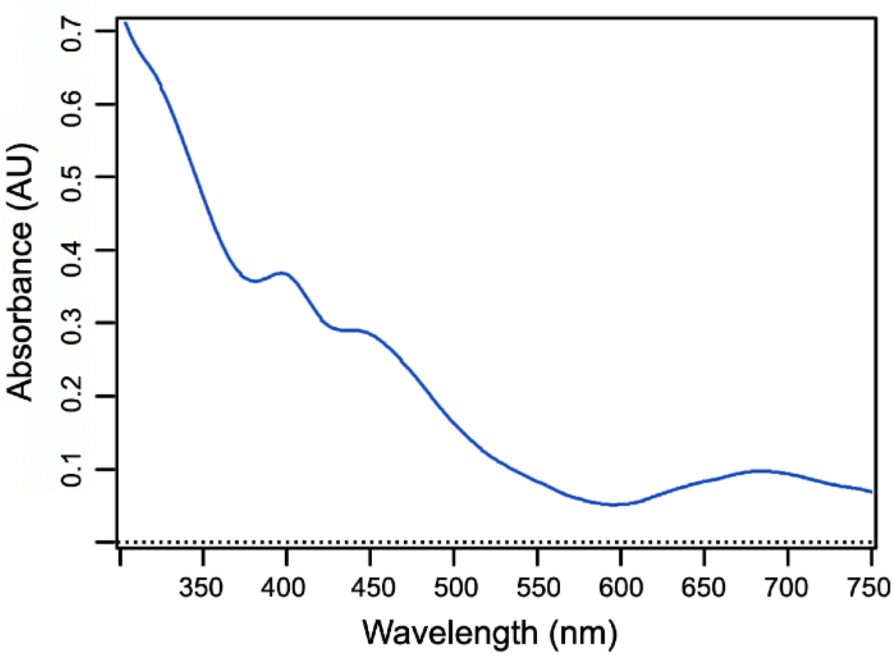

Figure SI.3.2. UV-Vis spectra at RT of the sample seen in Figure S1 taken with regular spectrometer.

Further Electron Microscopy Analysis

Electron micrographs were collected with TEM at CSU and CU Boulder, and SEM at CSU. The preparation for TEM at Boulder was done at 0.200 AU at 450 nm in 85% Ethanol. The preparation for TEM at CSU was done at 0.200 AU at 450 nm in 85% Ethanol (S2) and SEM preparation at 0.360 at 450 nm in 85% Ethanol (SI.3.3). Figures SI.3.3 and SI.3.4 below are included for comparison.

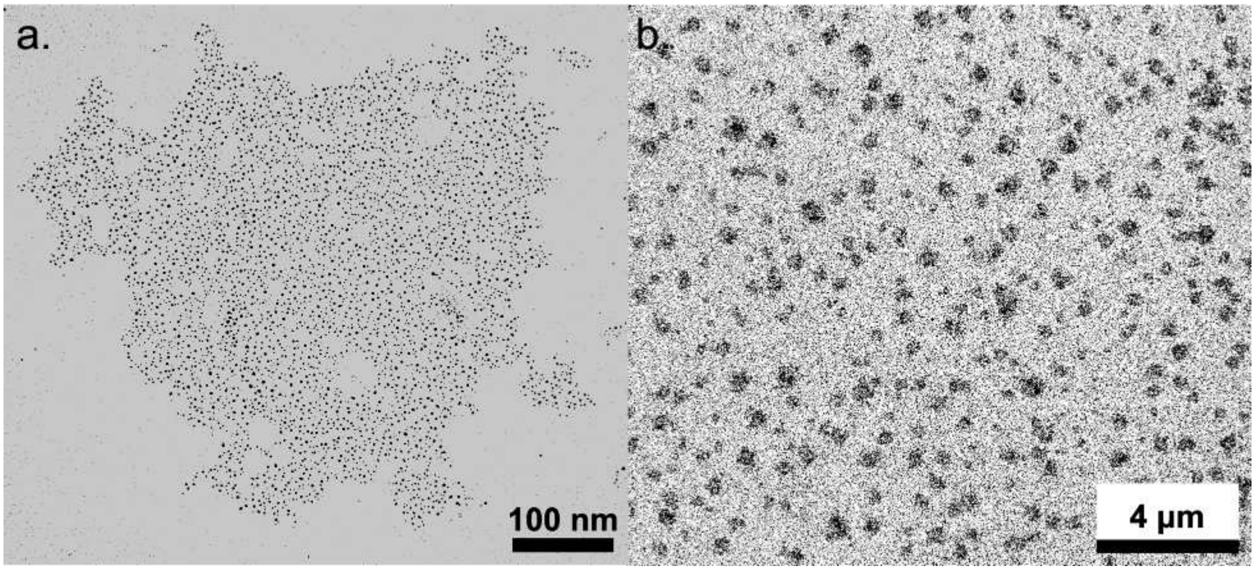

Figure SI.3.3. TEM micrographs of superclusters taken at University of Colorado - Boulder showing **a.** one supercluster on a grid with amorphous shape, and **b.** a full view of the monodispersity of the superclusters around 400 nm.

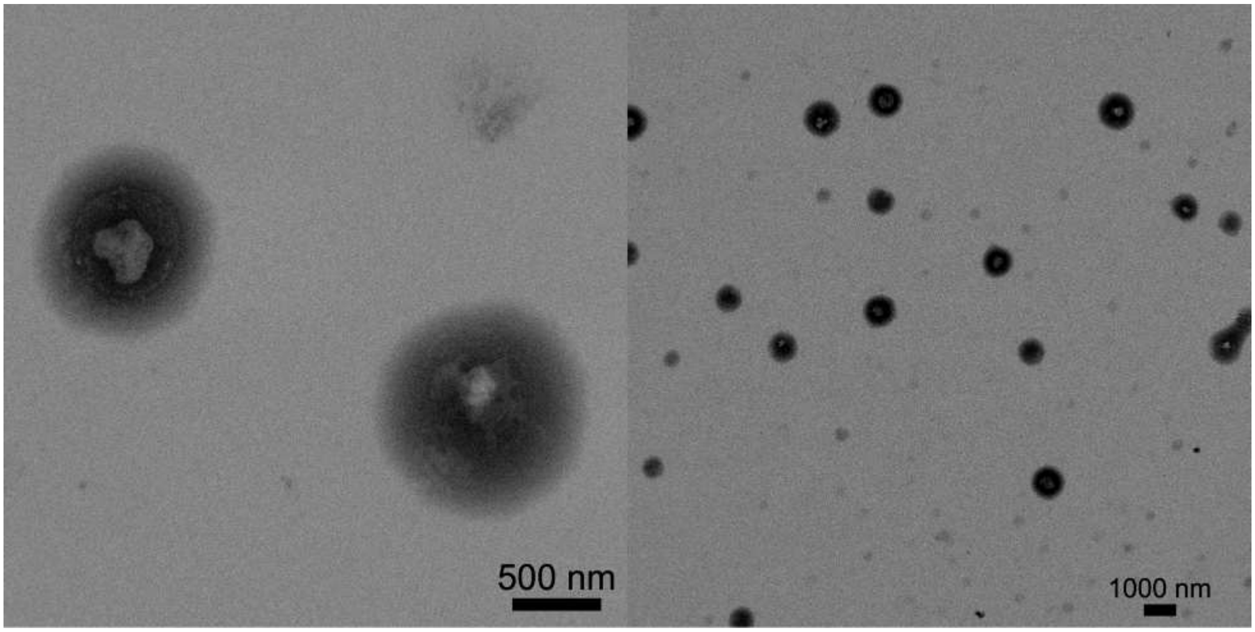

Figure SI.3.4. SEM Micrographs showing superclusters with **a.** being two superclusters around 500-600 nm in diameter and **b.** showing a larger field of superclusters on the grid with sizes from 600-800 nm.